Spring 2022

Rational Synthesis of Ultra-small and Durable Platinum-based Catalysts for Renewable Energy Applications

Fahim Bin Abdur Rahman

Rational Synthesis of Ultra-small and Durable Platinum-based Catalysts for Renewable Energy Applications

by

Fahim Bin Abdur Rahman

Bachelor of Science
Bangladesh University of Engineering and Technology, 2012

Master of Science
Independent University-Bangladesh, 2015

Master of Science
Texas A&M University at Qatar, 2017

Submitted in Partial Fulfillment of the Requirements

for the Degree of Doctor of Philosophy in

Chemical Engineering

College of Engineering and Computing

University of South Carolina

2022

Accepted by:

John R. Regalbuto, Major Professor

John R. Monnier, Major Professor

Christopher T. Williams, Committee Member

Jacob S. Spendelow, Committee Member

Melissa Ann Moss, Committee Member

Tracey L. Weldon, Vice Provost and Dean of the Graduate School

Dedication

I dedicate this dissertation first and foremost to Almighty Allah for giving me the confidence to believe in myself right from the beginning to this very point. I also dedicate this work to my lovely wife, Maimuna Akter, for her endless support, inspiration, and unconditional love throughout my endeavors. This work is also dedicated to my son, Fayzan Muhtadi, and daughter Mariyam Farzeen, who made this journey pleasant and less stressful. Lastly, I dedicate this work to my parents, who are why I am here today.

Acknowledgments

First and foremost, I would like to express my sincere gratitude to my advisor, Dr. John R. Regalbuto, for his expert guidance, support, and constant encouragement, which have made this scientific work more impactful and exciting. I have felt incredibly fortunate to have him as a mentor, who has provided me the liberty to explore research independently and aided me with brilliant thoughts when my steps faltered. Furthermore, his kindest heart has taught me many lessons that impacted my personal life to a great extent.

I would also like to thank my co-supervisor, Dr. John R. Monnier, and my committee member, Dr. Christopher T. Williams, for the valuable time and constructive inputs during different phases of my research. Their guidance and assistance have significantly extended my research perspective, enriched my capabilities, and improved my judgment and ability to solve research problems.

I am also incredibly thankful to Dr. Jacob S. Spendelow for allowing me to work in a promising technology field at Los Alamos National Laboratory (LANL). Working with him at LANL has given me a complete experience of the industrial working culture and made me a more confident and efficient problem solver. Furthermore, he included me in collaboration with different parties, including renowned US universities and National Laboratories, which enriched my communication skills and taught me professionalism.

I want to make a special mention to Dr. John M. Tengco and Dr. Stavros G. Karakalos for sharing their insightful expertise and helping me to understand different technical tools throughout my research. Also, I am grateful to the people, especially

in CReF, without whom my time at USC would not be that meaningful. For their constructive scientific discussions, passions for research, and vigilance and teamwork, the research group has become very organized, interactive, and productive, making me one of the best I have ever worked.

My profound appreciation goes to my parents for having faith in me and my wife, Maimuna Akter, for her continuous encouragement and love throughout my endeavors. Furthermore, I acknowledge my son and daughter, who have made my journey enjoyable and less stressful. Last but not least, I would like to thank the Almighty Allah for keeping all circumstances in favor of me and letting me accomplish this dissertation.

Abstract

Ultrasmall supported platinum nanoparticles (Pt NPs) are often used in two promising renewable energy production technologies – hybrid-sulfur water splitting for actively catalyzing H_2SO_4 decomposition and in fuel cells for the oxygen reduction reaction (ORR). However, the stability of Pt NPs under reaction conditions is the ultimate challenge for these processes. Two prevalent ways to overcome this challenge are improving stability by anchoring Pt onto a secondary metal or doping heteroatoms into the support. This dissertation covers the rational design, synthesis, and stabilization of Pt-based catalysts in these two ways to achieve durable catalytic performance with desired activity and selectivity.

The first vein of this research explores the stabilization of core-shell structured Ir-Pt bimetallic NPs on pre-stabilized titania (TiO_2) or boron nitride (BN) support for high-temperature H_2SO_4 decomposition, particularly SO_3 to SO_2 decomposition. A series of Ir-Pt catalysts have been synthesized with different Ir loading and evaluated for the selective decomposition of SO_3 to SO_2 in an extreme (high temperature, highly corrosive) reaction environments. Investigations have revealed that the deactivation of Ir-Pt catalyst on pre-stabilized TiO_2 is more dominant than BN, confirmed by X-ray diffraction and catalyst evaluation results. Furthermore, a negligible catalyst deactivation has been obtained for 1%Pt-7.5%Ir/BN. Various characterization techniques have been employed to explain this consistent stability.

In the second vein of research, the stabilization of Pt NPs by nitrogen-doped carbon has been explored with a combination of high sensitivity X-ray diffraction (XRD) and X-ray photoelectron spectroscopy (XPS) with in-situ pretreatment. The high

sensitivity XRD instrument has allowed the incredibly observationed the behavior of ultrasmall Pt NPs (about 1 nm), which was previously impossible to observedetect. Furthermore, the XRD results have been clarified the unappreciated trend in the literature of why XRD peaks of ultrasmall Pt NPs often appear shifted to the left. Additionally, using XPS, this work has been corrected a prevalent literature delusion that higher valences of Pt in N-doped carbon result from the formation of Pt-N bond.

In the final part of this work, the strong electrostatic interaction (SEA) technique has been explored to synthesize small, uniformly distributed, and highly dispersed Pt NPs on Vulcan XC72R carbon (Pt/C). The SEA method has significantly improved catalyst durability for ORR in proton-exchange membrane fuel cells (PEMFCs) by tuning metal-support interactions, confirmed by a comparative durability study in PEMFCs on various Pt/C catalysts prepared by dry and wet impregnation, polyol, and SEA methods. In addition, a thermal stability test has been performed based on these Pt/C catalysts that have validated the superiority SEA catalyst by demonstrating the metal-support interactions.

Table of Contents

List of Tables

List of Figures

Chapter 1

Introduction

1.1 Background and motivation

A catalyst is a material that transforms reactants into products via an uninterrupted and repetitive cycle of elementary steps without undergoing any permanent chemical change at the end of each cycle through its lifespan. Usually, a catalyst increases the chemical reaction rate by lowering the activation energy without impacting equilibrium or reaction thermodynamics [1, 2]. Catalytic processes account for almost 80% of overall chemical conversions, equivalent to about 20% of the total value of commercial products produced in the US [3]. Also, nearly 90% of these catalytic processes use heterogeneous catalysts; the catalyst is in a different phase than reactants [4]. In standard heterogeneous catalysts, metals are dispersed as small particles (submicron to nanometer) on high surface area supports (mainly oxides – titania, silica, alumina, ceria, zirconia, and carbons) that upsurge the utilization of metals, yielding a higher production rate. The support physically separates these particles and holds them on the surface by chemical interactions [5]. The most common heterogeneous catalysis applications encompass food, pharmaceutical, petrochemical, agricultural, automobile, and other commodity and specialty chemical industries [6–10]. Recently, heterogeneous catalysts are being used in emerging chemical processes such as fuel cells [11–13], green chemistry [14, 15], nanotechnology [16], and biorefining [17–19]. Therefore, a substantial amount of attention has been received to understand the role of these catalysts and make them efficient with systematic tuning to address issues facing our existing catalytic processes.

The instability of supported catalysts, especially at excessively high temperatures and vastly oxidative environments, is one of the foremost challenges in heterogeneous catalysis. Exposure of metal NPs at such extreme conditions leads to NPs sintering (the growth of Pt NPs from the more minor constituents), causing substantial loss of active catalyst sites that result in significant long-term catalyst deactivation [20–22]. The loss of active sites is critical when precious group metals (i.e., Pt, Pd, Rh,

Ir, and Ru) are active materials. Particle agglomeration, phase transformation due to metal particle oxidation, and destruction of support pores during reactions have been identified as the primary causes for metal sintering [23]. Therefore, stabilizing metal NPs under reaction conditions has become a priority in recent catalysis works. Numerous techniques have already been revealed for stabilizing supported metal NPs. For example, the preparation of stable bimetallic NPs by incorporating secondary metal with primary metal NPs [24–26], the increase of nucleation sites by doping heteroatoms onto the support [27–30], the improvement of metal-support interactions by tuning catalyst synthesis methods [31–36], and support modification either by developing a stable composite [37, 38] using multiple supports or applying additional treatments [39–43] are reported as the most common stabilization techniques.

The catalyst deactivation due to metal sintering is frequently reported for Pt-based catalysts [20–22], although supported Pt NPs are the most used heterogeneous materials with tremendous scientific and technological significance because of their extensive applications in various industrial catalytic processes, including steam reforming [44–46], hydrogenation [47–52], oxygen reduction in fuel cells [53–57], methanol oxidation [58–60], water gas shift [61–63], and SO_3 decomposition in hybrid water splitting [64–66]. A complete discussion of Pt sintering is difficult because the degree of Pt sintering depends on the catalyst composition, physical and chemical properties of the materials, reaction environments, metal-support interactions, morphology, pallet shapes, and many unknown variables [67]. However, the effect of catalyst stabilization can be observed based on the improvement of catalytic performance. Therefore, this work emphasizes synthesis, and stabilization of supported Pt-based catalysts, especially for ORR in fuel cell and SO_3 decomposition in hybrid water splitting processes.

1.2 Supported metal nanoparticle synthesis

1.2.1 Overview

In most catalytic reactions, the synthesis of highly dispersed, ultrasmall, and stable metal NPs is desirable. Ultrasmall NPs with high dispersion (the number of metal atoms on the surface divided by the total number of metal atoms in the catalyst) increase the active metal surface area to the volume ratio by mounting the number of accessible active metal sites on the support surface that improves overall catalytic performance. Conversely, the overall contacts between reactants and catalyst NPs are reduced when the dispersed metal particles are oversized. Consequently, metal consumption intensifies, and normalized catalyst activity decreases [68]. Various methods have already been explored to attain small metal NPs with the maximum amount of metal atoms exposed on the surface. However, the favorability of these methods for industrial-scale uses depends on materials availability, production complexity, and scalability [69]. Also, the ability to synthesize such metal NPs depends on the chemistry between metal precursors and the support. Some of the most used catalyst synthesis techniques are discussed below.

1.2.2 Impregnations

Impregnations are the most common and straightforward techniques to synthesize supported catalysts. In impregnation, a metal precursor is dissolved in a solvent, usually water, and filled the precursor solution into the support pores. Based on the volume of precursor solution used, the impregnation methods are named incipient wet impregnation (IWI)/dry impregnation – the volume of precursor solution is equal to the pore volume of the support and wet impregnation (WI) – the volume of precursor solution is above the pore volume of the support. In impregnation methods, no metal is wasted. However, non-uniform metal distribution is developed as the metal

complex remains in the solution, conveying to the support surface by drying only. Additionally, the pH of the solution is rarely controlled before impregnation, while controlling pH is critical to obtain strong metal-support interactions [70]. After drying, the impregnated sample goes through a calcination (in the air) or reduction (in H_2) treatment to transform precursor ligands into metallic NPs. Counterions inside the precursor complex react with H_2 or air and emit as gaseous products. However, alkaline metals and their salts are less reactive to H_2/air, remaining in the final catalyst. Impregnation is typically the best choice when the reaction is less sensitive to the catalyst NP size or when other synthesis methods fail to produce well-dispersed ultrasmall catalyst NPs under reaction conditions.

1.2.3 Deposition-precipitation

The precipitation method alters a solution of the soluble precursor salt into a solid material by transforming the metal complex in the precursor solution into metal NPs. The pH and concentration of the precursor solution, natures of precipitation/reduction and complexing agent, and operating temperature are the most critical factors to control the kinetics of metal NP nucleation and growth [71–73]. Monodispersed NPs are formed when nucleation time is short, and 'bust nucleation' is achieved. In contrast, bimetallic NPs are formed due to co-precipitation. Vigorous mixing is necessary for the homogeneous distribution of the precipitating agent [74–77]. The precipitated metal NPs are deposited on the support either by impregnation or colloidal methods. However, the metal complex can also be directly precipitated onto the support, known as the deposition-precipitation (DP) method [78]. In the DP method, metal NPs nucleate and grow on the suspended support using an adsorption mechanism in basic conditions; no deposition occurs in the solution. Sodium hydroxide and urea are commonly used as precipitating agents to control the solution pH, and precipitate metal NPs on the support [79–81]. The DP method is sensitive to

concentration or temperature gradient, uniform mixing, and local fluctuation in nucleation and growth. In addition, an inadequate understanding of this method leads to poorly dispersed supported NPs. Therefore, the DP method is highly favorable when very high metal loading (i.e., 50 wt%) is desirable [82].

1.2.4 Colloidal/Polyol

The colloidal method produces metallic NPs beforehand that are deposited later on the support with controlled size, uniformity, and dispersion in alkaline ethylene glycol (EG) solution; EG functions as a reducing agent [83]. However, the deposition of colloidal metal NPs on the support in EG solution is still a concern because the change of colloid NPs to supported NPs is less controllable. Like WI, the colloidal NPs deposition onto the support surface occurs through an uninterrupted mixing of support and the solution containing metal NPs. The solvent is removed either by evaporation or filtration; the weight loading of colloidal catalysts needs to be confirmed after the WI. Typically, colloidal catalysts need additional heat treatment to remove the residual reducing agent, leading to particle sintering, especially in bimetallic systems. Besides, like impregnation approaches, the polyol method does not control the solution pH, which may cause insufficient interactions between colloidal metal NPs and the support [84].

1.2.5 Strong electrostatic adsorption (SEA)

SEA is a particular form of the WI method, where ionic precursors are adsorbed on a charged support surface through coulombic interactions between the support surface and the precursor. Typically, the support surface is charged by carefully adjusting the pH of the precursor solution [85]. Pioneering work by Brunelle first revealed the interactions between nobel metal complex and mixed-oxide surfaces [86]. Regalbuto's group extensively implemented this concept to prepare supported metal NPs on

various mixed-oxide, and carbon supports [87–90]. In the typical SEA method, it is necessary to determine the optimum pH of the precursor solution where the maximum amount of precursor adsorbed and metal-support interactions are the strongest.

The point of zero charge (PZC – the pH where the net charge on the support surface is zero) of the support plays the most crucial role in determining the type of precursor and the optimum solution pH. When the solution pH is adjusted away from the PZC, the functional groups on the support surface are protonated or deprotonated at pH below or above PZC, respectively (Figure 1.1a). A simple pH shift experiment determines the PZC of the support using high surface loading (Figure 1.1b). Surface loading (SL) refers to the surface area of the support exposed in the solution volume (m^2/L). Typically, the anionic precursor is adsorbed on the protonated surface (pH $<$ PZC) and vice versa (Figure 1.1c). The optimum SEA pH is estimated based on the uptakes of the preselected precursor on the support for a range of the solution pH. This pH is used later to adsorb metal precursor onto the support, followed by subsequent drying and reduction to attain metallic NPs. The metal precursor is adsorbed as a monolayer retaining many hydration sheaths. These hydration sheaths separate the precursor due to steric hindrance, providing high precursor dispersion on the support. Moreover, the coulombic forces provide strong precursor-support interactions, inhibiting agglomeration and migration of the precursor during drying. Consequently, highly dispersed and uniformly distributed supported metal NPs are formed through drying and calcination/reduction treatments.

However, finding an apposite precursor with the correct charge is still challenging for the SEA method. Also, achieving more than a monolayer coverage of the precursor is impossible since the metal precursor is adsorbed on the support as a monolayer. In the case of high metal loading requirements, multiple SEA cycles can achieve the desired weight percentage. Moving to a higher surface area support also can solve this issue because the adsorption density is constant for a particular precursor, and

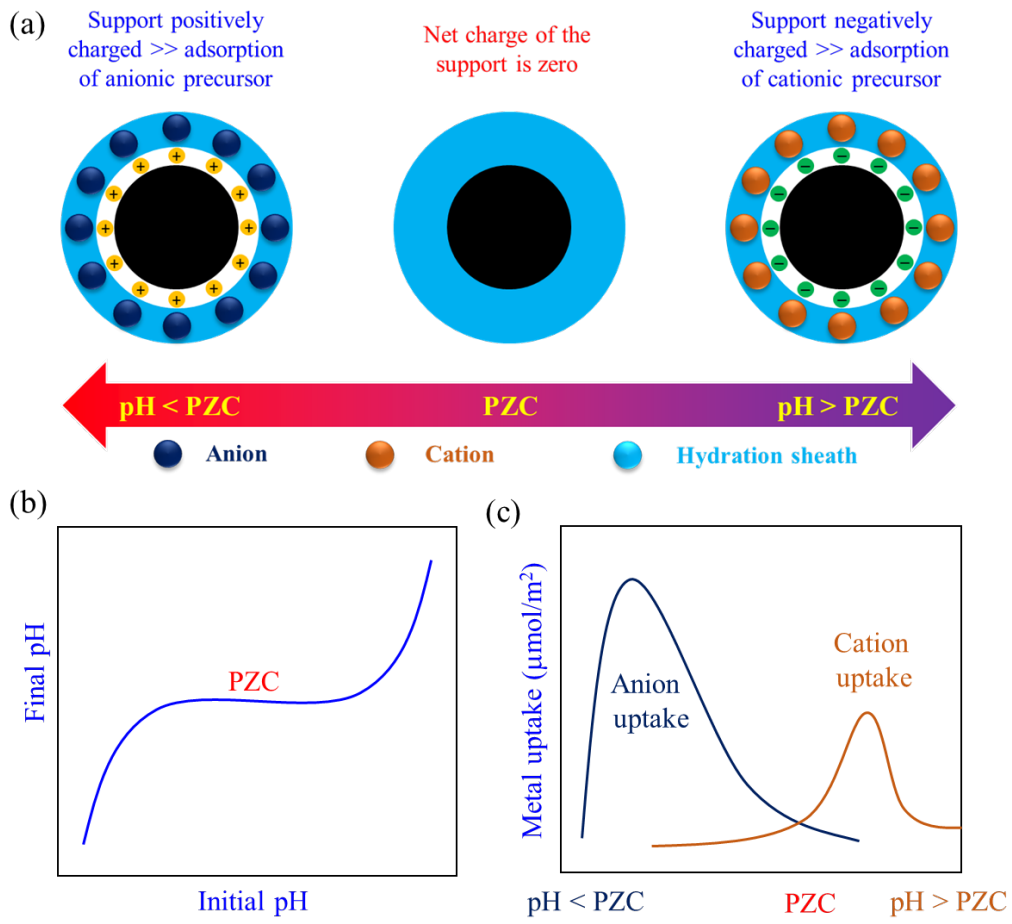

Figure 1.1 Strong electrostatic adsorption mechanism

the accessible surface area of the support is enormously increased. In multiple cycles SEA, the metal precursor needs to be reduced after each cycle so that the available surface will be freed for the next cycle of precursor adsorption.

1.2.6 Charged enhanced dry impregnation (CEDI)

CEDI combines SEA and IWI methods where a precursor solution with controlled pH fills pores of the support, minimizing the metal loss (a common problem in SEA due to filtration) with improved metal NPs dispersion. Like SEA, the precursor solution is acidified or basified in the CEDI method to form coulombic force between

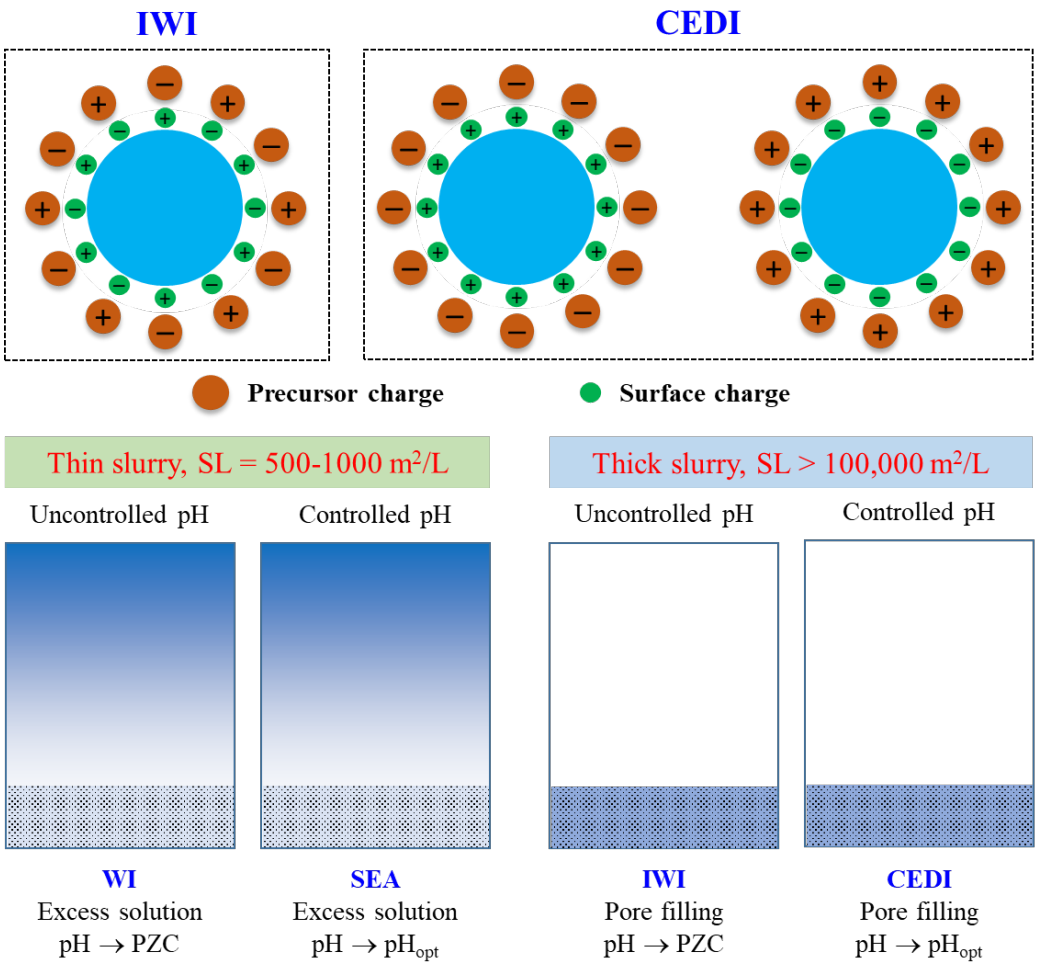

Figure 1.2 Graphical illustration of WI, IWI, CEDI, and SEA methods

the charged surface and oppositely charged precursor solution; however, the precursor solution is filled onto the support pores by the IWI method [91]. Figure 1.2 illustrates the difference between IWI, WI, SEA, and CEDI. Although catalysts synthesized using CEDI demonstrate excellent metal-support interactions because of electrostatic adsorption, metal particles sintering during synthesis due to residual counter ions such as chloride and nitrate are still a critical concern. Removing these counter ions by repetitive washing can effectively stabilize NPs from sintering and keep particles small with narrow distribution [92].

1.2.7 Electroless deposition (ED)

ED is a reactive adsorption process, producing the core-shell structured bimetallic catalyst where a secondary metal is reduced and deposited onto the surface of pre-existing supported metal NPs. ED uses an analogous concept as electroplating, but a reducing agent (RA) is applied instead of electricity; hence, the ED is also called 'Electroless plating' [93]. Besides catalysis, ED is employed in metal plating and thin-film fabrication. The synthesis of core-shell structured bimetallic catalyst using ED method prerequisites an aqueous bath of predetermined pH, a secondary metal precursor, and a reducing agent (i.e., hydrazine – N_2H_4, dimethylamine borane – DMAB, formaldehyde – HCHO, and hypophosphite – $H_2PO_2^-$). Before aiming for ED trials, a primary metal (M_1) is deposited onto the support using one of the techniques cited above. The dispersed NPs act as the active sites for secondary metal (M_2) deposition by ED.

When RA is added to the ED bath containing the supported M_1 NPs, the RA first interacts with active sites of M_1, later decomposes, and departs adsorbates, enabling the reduction of the M_2 precursor onto the M_1 surface that creates a core-shell bimetallic structure. The formation of the core-shell structure by ED promotes excellent interactions between metals. ED can occur either catalytically or autocatalytically depending on the bath temperature, reducing agent, the extent of reaction, and the solution pH. In catalytic ED, M_2 deposits on M_1 with monolayer coverage where M_1 has all active sites; no deposition of M_2 occurs on M_2. After catalytic ED, in some cases, M_2 acts as an active site for ED, promoting the deposition of M_2 on M_2. This catalytic and autocatalytic combination leads to a thicker shell with lower coverage [94–96]. Either bubbling H_2 attains reduction of M_2 through an aqueous slurry containing M_1 catalyst to saturate the metal site with chemisorbed H atoms and then adding a soluble RA [97] or combining M_1 catalyst and organic RA in a

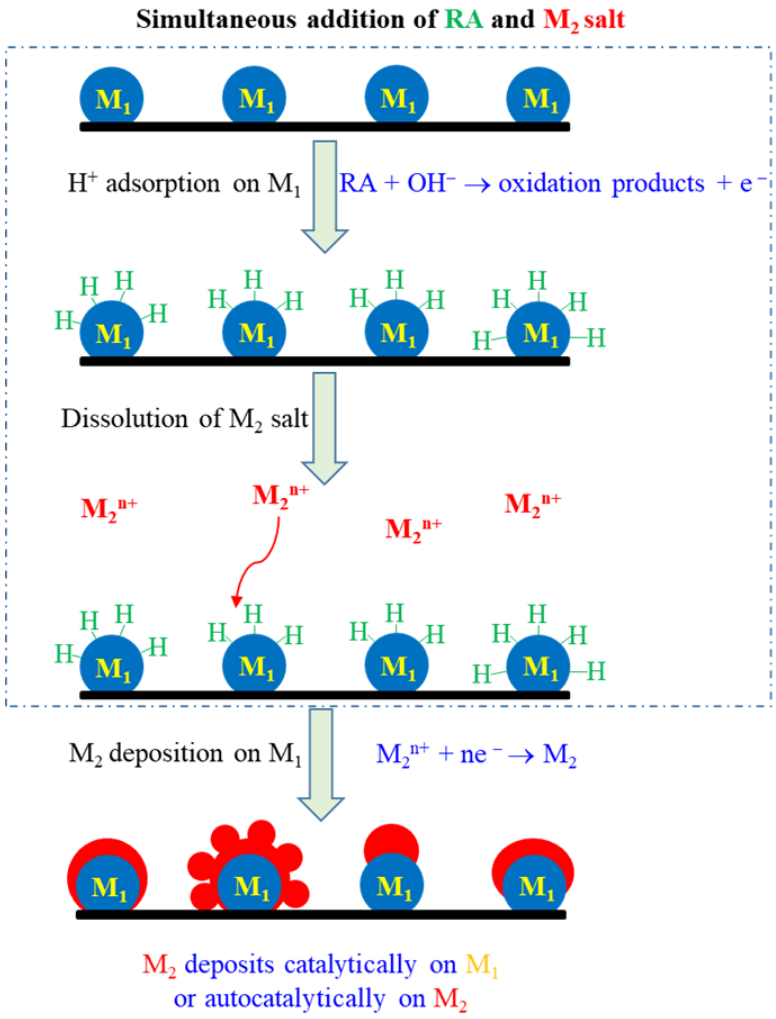

Figure 1.3 Schematic of bimetallic core-shell structured catalyst synthesis by electroless deposition

liquid phase with appropriate concentration [98].

The efficacy of ED is highly dependent on the bath conditions. Such as, adjusting pH in the ED bath is crucial to evade SEA and increase the electrochemical potential of the RA. Usually, a higher pH value is preserved for anionic metal precursor deposition in the ED bath. Moreover, the metal precursor must be thermally and chemically stable for a wide range of solution pH. The selection of RA is another vibrant factor for ED because the catalytic activity of RA controls the deposition

pathway (catalytic or autocatalytic). The catalytic decomposition is favorable when RA is more active for M_1; if RA is more active towards M_2 autocatalytic decomposition occurs. Typically, a stability test is made during the preparation of an effective electroless developer bath, where the deposition of M_2 is examined in the absence of M_1. Ideally, the M_2 only deposits on M_1; no precipitation or spontaneous reduction occurs in the solution without M_1 [96, 99]

1.3 Metal-support interactions

Metal-support interaction (MSI) has gained tremendous interest in recent scientific investigations, as it has a profound influence on the improvement of catalytic performance in reaction environments [35]. However, there are no exact mechanisms to elucidate MSI. As a result, immense efforts have been devoted to better understanding the nature of MSI in catalysis. Charge (electron) transfer between metal and support, the interfacial perimeter, the morphology of metal NPs, chemical composition, and strong metal-support interactions (SMSI) are the most common phenomena often combined to explain MSI. The influence of these phenomena in MSI depends on the catalyst materials and the type and conditions of the reaction. The leading phenomena of MSI and their tuning strategies are graphically illustrated in Figure 1.4 [32].

Electron transfer between metal and support occurs at the metal-support interface to reposition the electrons within the materials. However, the impact of this re-arrangement in catalytic performance is limited up to a few atomic layers at the interface. The charge transfer across the interface is determined in some cases by measuring the alteration of the oxidation state of the metal atoms using XPS [100]. The extent and direction of electron transfer are governed by discrepancies in the Fermi Level of the metal NP and support, eventually aiming to equalize electron chemical potential at the interface. However, the electron can still transfer with a

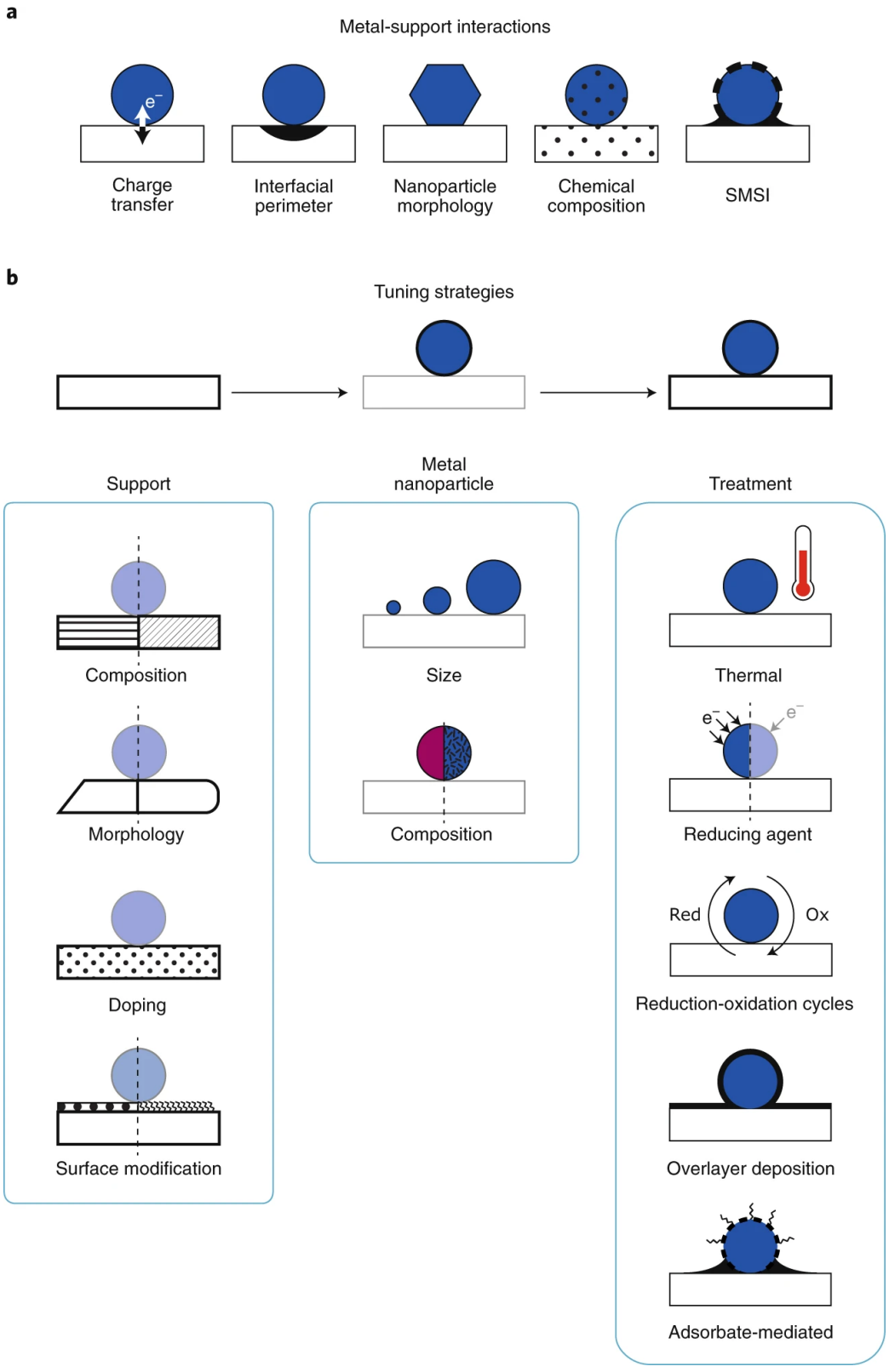

Figure 1.4 Graphical exhibition of metal-support interactions and tuning approaches [32]

minimal number (maximum of 0.003 electrons per atom) after attaining equilibrium [101]. The size and shape of metal NPs are critical for electron transfer as more localized electronic states are obtained for smaller NPs. In addition, the conductivity, reducibility, morphology, defects occurrence, and exposed crystal planes of the support also considerably impact charge transfer [35]. Typically, the synchronization of a reaction is enabled by direct interaction between the metal NPs, support, and reactants at the interface of support and the perimeter of the NPs. Due to electron transfer, the interfacial metal atoms accumulate more charge, accelerating the adsorption of reactants and reaction rate at the perimeter of the metal NPs [102]. Also, the proximity of metal NPs to various functional groups and defects at the support surface benefit successive local reactions or stabilize transition phases of reactants, and products [103].

As mentioned, the size, shape, and crystallographic structure of the supported metal NPs incredibly tune MSI, which enormously influence the catalytic performance. Usually, the reaction is favorable on particular facets, which are detected by the shape of the NPs. Depending on the facet, the bonding structures are altered, providing a distinct catalytic behavior in identical reaction conditions. For instance, the metal particles are tighter in (111) than (100) facets, resulting in a different coordination number and geometry of the atoms [104]. In addition, the adhesion energy (Ed – release at the metal-support interface) controls the shape of the NPs; a raft-like shape with more NPs facets is formed when the support consists of higher adhesion to the metal NPs. In general, the value of Ed is increased by reducing the size of the metal NPs. Besides, the mobility and sintering of supported NPs under reaction conditions are stabilized when the Ed value is high [36]. A stable shape of metal NPs with higher MSI is obtained when the surface free energy (SFE) is minimized due to specific contacts between the support and metal. However, the reaction conditions sometimes change the SFE of the metal NPs upon the adsorption of reactants on the

catalyst sites. Also, the formation of strain and defects due to misfitting between the support lattice and the NPs modify the overall morphology of the metal NPs and mismatching is profound for smaller NPs.

The chemical composition of support materials and catalytic metal NPs inherently influences MSI. For example, adding a transition metal (M – Co, Ni, Fe, Mn, Cu, Zn) in Pt/C catalyst significantly improves the catalyst durability for ORR in PEMFCs; the transition metal hinders the mobility of Pt NPs on the support surface, indicating the formation of improved MSI [105]. In addition, the compositional ratio between metals in supported bimetallic catalysts significantly impacts catalytic performance. For example, Yarlagadda et al. have found the lower specific activity of PtCo/C catalyst for ORR due to the reduction of Co content [106]. Besides adding M into Pt/C catalyst, doping carbon support with heteroatoms (N, B, S, O, P) boosts Pt-C interactions. Heteroatoms inside the carbon matrix form irregular and disrupt edge plane defects which provide higher densities of nucleation genesis from the deposited metal precursor, resulting in ultra-small and uniformly distributed metal NPs with improved MSI. Moreover, heteroatoms have higher electronegativity than conventional support, driving to form strong interactions between metal and support [27–30].

In heterogeneous catalysis, the metal NPs are encapsulated by partially reduced support oxides through a high-temperature H_2 treatment, known as strong metal-support interaction (SMSI). The concept of SMSI was first introduced in heterogeneous catalysis by Tauster et al. for tuning the catalytic performance of group (VIII) metals by modifying the electronic and geometric structures of metal sites [107]. Typically, the SMSI is formed for a combination of high SFE metal with the capability of activating H_2 and reducible transition metal oxides (support) with low SFE that generate suboxide species. During the formation of SMSI, the metal SFE is minimized due to the encapsulation of metal NPs by the support suboxides. However,

extensive coverage is undesirable as it blockages the active sites of metal NPs, hurting the catalytic performance. Furthermore, the partial coverage of suboxides alters the local electronic configuration of the active metal sites, promoting rapid activation of reactants that increase catalytic performance [108].

1.4 Nitrogen-doped carbon (NC)

The catalytic properties and the stability of metal-support binding are enhanced by inducing defects on carbon; controlling the defect formation mechanism is imperative to improve the catalytic potential [109]. Usually, defects allow the active metal catalyst more direct access to carbon's electronic "highway," which can be tuned to modify the electron donor/acceptor property, attributing to the bond formed between the metal particle at the defect site [110–112]. The modifications of carbon are the inherent defects that change how electrons move through the -network. The defective carbon has an increased affinity to metal ions than pure carbon, increasing metal uptake and potential particle nucleation sites [113, 114]. One of the most prevalent techniques of producing defective carbon is doping heteroatoms to the carbon lattice. Dopants are advantageous due to the potential for precision site engineering of bandgap structure and particle nucleation site dispersion. For catalysis, having a small bandgap is ideal since theoretically, this means the resistance to electron excitation, or flow, is at a minimum. In addition, dopants are typically added into carbon's defect sites, often substituting a carbon atom or filing a vacancy site, which improves electron transport across the structure, providing the most robust binding between the doped site and defective carbon lattice [112]. Doping carbon with nitrogen atoms has provided promising results, especially for fuel cell applications, as N atoms have excellent oxidation resistance and electron-accepting ability toward ORR. Also, N atoms within the carbon matrix have higher electronegativity than C atoms, significantly improving MSI [29]. Therefore, it is necessary to acquire a brief understating

of different approaches to N doping in the carbon structure.

1.4.1 Direct thermal treatment

Direct thermal treatment is one of the most accessible routes to synthesize NCs where carbon support is directly heated in the presence of a nitrogen-containing precursor. The doped N content and chemical and physical properties of NCs are critically reliant on the exposure time and thermal temperature. The highest nitrogen doping has been observed for a temperature range of 500-600 °C, and this amount is decreased with increasing treatment temperature. For example, Song et al. [115] have found the highest N content at 500 °C and lowest at 800 °C. In addition to that, the different N-containing precursors have shown different chemical bonding formations and N content. For instance, the annealing of graphene oxide with NH3 favorably forms graphitic and pyridinic N centers, while annealing with polyaniline and polypyrrole preferentially generates pyridinic and pyrrolic N, respectively [116].

1.4.2 Functionalization of carbons by N-containing compounds

Carbon modification by functionalization or doping often is performed to achieve improved results for specific applications. Typically, carbon is functionalized using an N-containing precursor through a wet chemical route (a process generating products by chemical reactions in the solution) followed by high-temperature calcination [117]. Functionality refers to when multiple atoms of a non-carbon element (i.e., nitrogen) are randomly added in a non-specific manner to the carbon. This method is easy to scale up since the production of NCs occurs in the solution [116]. Like the direct thermal method, calcination temperature and annealing time control the configuration, type, and amount of doped N inside the carbon structure. For example, Yu et al. have observed the formation of pyridinic and quaternary N during the carbonization of pentagonal polypyrrole at 900 °C, and the specific surface area and

pore size distribution can be precisely controlled by tuning calcination temperature [118]. In recent years, N-doped graphene oxide (GO) has been found as one of the most promising materials in catalysis due to its high dispersion in a wide range of solvents, including water, acetone, and alcohol. In addition, the oxygen functional groups on the GO surface have a high affinity to chemically react with N-containing precursors, resulting in the insertion of N atoms on the GO surface [116]. Sun et al. showed how NH_3 compound from hydrothermal urea decomposition reacts with oxygen-containing GO to produce an N-doped graphene skeleton [119]. Typically, a mixture of a nitrogen source with dispersed carbon is sonicated prior to hydrothermal treatment at optimum temperatures for control synthesis of NC with uniform N dispersion and high N content. The mass ratio between the carbon and N-containing source tunes N content [120]. The typical sources of N are hydrazine, NH_4HCO_3, urea, $(NH_4)_2CO_3$, hydroquinones, and glucosamine [116].

1.4.3 Chemical vapor deposition

The chemical vapor deposition (CVD) method extensively synthesizes N-doped carbons. In the typical CVD, a gaseous carbon source (mostly CH_4) is adsorbed, dissociated, and catalytically precipitated on a Ni or Cu film in a quartz tube furnace under the combination of H2 and Ar environment; typically, Si substrate is used as the catalyst [121]. When the furnace temperature reaches 800-1000 ^oC, an N-containing precursor is introduced in the gas flow, aiding the growth of N-doped carbon (NC) [122, 123]. Rapid heating is necessary to avoid aggregation of the catalyst film. After the growth is done, the sample is cooled to room temperature in an H_2 or inert atmosphere. However, carbon and nitrogen can be sourced from the same precursor (i.e., CH_3CN) [122]. Doping N atoms onto carbon by CVD is not limited to the gas mixture; liquid-based organic precursors like acetonitrile and pyridine are also used. However, the formation of NC using liquid precursors critically needs special skeletal

bonds. For example, C-C, C=C, and C≡N in acrylonitrile cannot produce NC, while C=C bonds in pyridine participate in the formation of NC [124]. Apart from skeletal bonds, the gas flow rate, growth temperature, and catalyst also influence the synthesis of NC using CVD [125].

1.4.4 Pyrolysis of nitrogen-containing complex

Pyrolysis is a chemical process in which a sizeable complex material is thermally decomposed into more analytically accessible fragments at elevated temperatures and anaerobic environments [126]. In a typical preparation of NC using pyrolysis technique, N-comprising compounds, mostly NH_3, have been flown across the support placed in a furnace at elevated temperatures for a specific period. Therefore, N-containing compounds break down into N atoms which are adsorbed on the carbon surface. For example, Luo et al. doped approximately 10.3 at% of N into carbon using direct pyrolysis of commercial cellulose under NH_3 environment at 550-1000 °C for 2-6 h [127]. In the case of N doping into commercial carbons, carbon support is oxidized by soaking into concentrated acid at 70-80 °C for 6-8 h prior to the carbonization process. Finally, the soaked sample is washed, dried, and annealed under NH_3 or N_2 environment at approximately 500-1000 °C [128]. Besides using NH_3, Ashourirad et al. used benzimidazole (BI) as N-source to prepare NC where BI was mixed with KOH. Then, the mixture was heated under Ar gas in a temperature-programmed tube furnace at 600-800 °C for an hour to transfer N atoms from BI to carbon [129]. Furthermore, the porosity and capacitance of NC prepared by this method can be balanced by tuning the pyrolysis temperature [129].

Chapter 2

Stabilization of Ir-Pt bimetallic catalysts for high-temperature SO_3 to SO_2 decomposition to produce H_2 and O_2 using hybrid-sulfur water-splitting process

2.1 Abstract

Catalyst deactivation is a primary concern during the decomposition of SO_3 to SO_2 at temperature 800 °C, a critical step commonly featured in the hybrid sulfur (HyS) water-splitting process for H_2 generation. Enhancing the long-term performance of catalysts for this reaction was explored through support pretreatment and nanoparticle (NP) stabilization by surface free energy (SFE) difference. A series of Pt-based catalysts supported on both titania (TiO_2) and boron nitride (BN) was synthesized and evaluated at the high-temperature oxidative environment of the actual reaction. Exposure of the TiO_2 and BN supports at conditions similar to reaction, specifically static air calcination at 800 °C for 8 h, prior to use in catalyst preparation, resulted in improved stability of catalysts. This was attributed to diminished changes in the support structure and pore collapse. By using electroless deposition (ED) to anchor low-SFE Pt on higher SFE Ir, supported on either TiO_2 or BN, the sintering of Pt was effectively limited. Evaluation of the catalysts showed consistently improved performance of the Ir-Pt catalysts with increased resistance to sintering. BN was also determined to be superior to TiO_2 due to the retention of high surface area after pretreatment and at reaction conditions.

2.2 Introduction

Hydrogen is considered an efficient energy carrier [130–132]. When used as a vehicular fuel, it provides 2.6 times more energy than gasoline while eliminating greenhouse gases (GHG) from gasoline combustion [133, 134]. The global demand for hydrogen is predicted to massively increase over the next few decades from 71 million tons used in 2019 to 519 million tons by 2070 [135]. Over 95% of commercial hydrogen is produced through GHG emitting processes that consume fossil fuels, such as steam reforming, partial methane oxidation, and coal gasification [136]. The abundance of non-fossil

fuel renewable energy resources can provide an environment-friendly, and sustainable means of hydrogen production [130]. Thermolysis is considered a viable alternative when using a renewable heat source, such as solar energy to split water molecules into hydrogen and oxygen. However, the high temperatures (approximately 2500 K) needed for water-splitting create issues with material selection, and construction regulations [137, 138].

Thermochemical cycles for water-splitting have been proposed for large-scale and low-cost generation of H_2 and O_2 [139]. In particular, the HyS process, which is a sulfur-based thermochemical cycle that utilizes non-fossil fuel input as the primary heat source, has generated significant interest. In the HyS process, H_2SO_4 decomposes into SO_2 and O_2 (by-product), yielding H_2 (product) after an electrochemical reaction between SO_2 and H_2O at 80-120 ^oC. H_2SO_4 is completely recycled from the process for further production of SO_2. The decomposition of H_2SO_4 to SO_2 occurs in two steps: a non-catalytic thermal decomposition of H_2SO_4 to SO_3 and H_2O at about 350-400 ^oC, followed by catalytic decomposition of SO_3 to SO_2 at $\geq$ 800 ^oC [140]. A schematic of an integrated thermochemical water-splitting facility is shown in Figure 2.1, where heat for the catalytic decomposition is proposed to be supplied by an array of mirrors focusing sunlight on an elevated reactor. In studies evaluating catalysts for the SO_3 to SO_2+$\frac{1}{2}O_2$ decomposition step, most showed lower activity as a result of sulfate formation [141–143] while others did not meet catalyst performance benchmarks due to the formation of volatile acid salts [141], support poisoning [141], and catalyst attrition [144]. TiO_2 supported Pt NPs have been shown to catalyze the decomposition reaction effectively.However, the cost and long-term stability of these catalysts present notable drawbacks for commercialization. The excessive reaction temperature causes catalyst deactivation via sintering of the Pt NPs due to both high temperature sintering and structural degradation of the catalyst support [145–148] that highlights the need to improve catalysts by minimizing NP sintering and

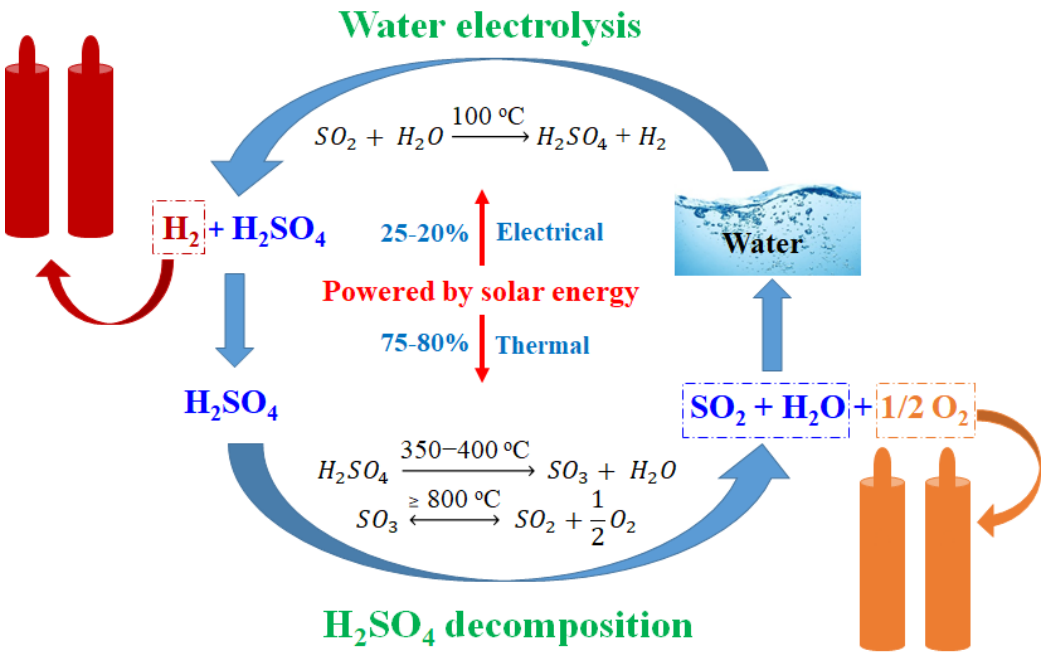

Figure 2.1 A schematic diagram of the hybrid-sulfur water-splitting cycle

enhancing support stability. This work focuses on the development and stabilization of a Pt-based catalyst for SO_3 to SO_2 conversion with acceptable activity.

Under heat treatment, the stability of catalyst support is related to the resistance of the structure to change. As the metal nanoparticles are anchored by interaction with the support surface, rearrangement of the surface atoms can weaken the support-particle interaction, resulting in particle mobility and sintering [149]. Selecting a support material that will be resilient to transformation at reaction conditions is critical to catalyst design and synthesis. The anatase phase of TiO_2 is known to undergo a transition between 400 °C to 1000 °C to form the rutile phase [150]. Pretreatment of the support by inducing phase change to stabilize the surface before adding Pt NPs can be a route for catalyst development. Substitution of the support with a more robust material is also an alternative. Boron Nitride (BN), a non-oxide ceramic type of support that exhibits higher thermal stability and oxidation resistance with greater mechanical strength [151–153], has been used as a support for numerous

high-temperature catalytic reactions [153–156]. Zhu et al. [157] demonstrated that Pt-NPs strongly interact with vacancy-abundant BN, significantly improving catalyst performance. Improving catalyst durability can also be done by hindering the sintering caused by particle migration or Ostwald ripening. A bimetallic nanoparticle system can be taken advantage of where the SFE difference between two metals will influence metal mobility [24–26, 158]. Catalysts with a core-shell structure have been claimed to offer better resistance to metal sintering for high-temperature reactions [159–162]. The higher SFE metal serves as the core anchoring the lower SFE shell metal. Such NP morphologies have been successfully prepared using the ED synthesis technique [24–26] . In ED, illustrated in Figure 1.3, targeted deposition of a secondary metal onto a pre-existing primary metal is achieved through a reduction-oxidation mechanism. Pt can be deposited by ED on a higher SFE core metal NP like Ir, which can then stabilize the Pt metal.

In this study, the stabilization of Pt-based catalysts for SO_3 decomposition was explored by techniques mentioned for support and nanoparticle stabilization. Pretreated TiO_2 and BN were used as support materials while a Ir-Pt NP system was developed by ED. The catalysts were synthesized and subsequently exposed to a high-temperature oxidative environment and evaluated at actual reactions.

2.3 Experimental

2.3.1 Materials and methods

Aeroxide TiO_2 P25 (Evonik, BET SA=65 m^2/g) and BN (Alfa Asear, BET SA=61 m^2/g) was used as catalyst supports, which were calcined at 800 °C in static air in a muffle furnace for 8 h. The calcination was done to minimize support collapse during operation at high temperatures. Incipient wetness impregnation (IWI) method was used to synthesize monometallic Pt and Ir catalysts, where an aqueous solution of

corresponding precursor tetraamineplatinum (II) hydroxide hydrate (99.99%) and hydrogen hexachloroiridate (IV) hydrate (99.98%) from Sigma-Aldrich was added into the support to achieve incipient wetness. The impregnated materials were subsequently dried overnight in ambient air, followed by oven drying at 120 °C for 8 h. The dried powders were then reduced under 10%H_2 (balance He) flow at 300 °C for 2 h to transform precursor salt to metallic NPs.

The ED technique was employed to synthesize Pt-based bimetallic catalysts, where the lower SFE Pt was anchored on higher SFE Ir base-catalysts. For ED experiments, hydrogen hexachloroplatinate hydrate (99.9%), dimethylamine borane (DMAB, 97%), and ethylenediamine (EN, ≥99.5%) from Sigma-Aldrich were used as Pt salt, reducing agent, and stabilizing agent. ED experiments were conducted at 50 °C temperature with pH 10.0, and the solution pH in the ED bath was adjusted by NaOH (JT Baker). The kinetics of Pt deposition on Group VIII base metal catalysts using DMAB was demonstrated in previous work by Beard et al. [163–165]. Prior to the ED experiments, the desired concentration of Pt^{4+} salt solution and the solutions of DMAB and EN were simultaneously added into the ED bath at a molar ratio of Pt:EN:DMAB=1:4:5. The solution was kept for 30 min to ensure there was no thermal deposition of $PtCl_6^{2-}$ due to the rection between Pt salt and DMAB (known as 'thermal stability test'). The Ir and Ru (different preparation) base catalysts were placed in the ED bath and continuously agitated to maintain a uniform temperature of 50 °C throughout the ED experiment. To determine whether strong electrostatic adsorption of $PtCl_6^{2-}$ on the catalyst support occurred in the ED bath, a controlled experiment was done where the support was placed in the bath instead of the base catalyst keeping all other parameters the same. The purpose of the control experiment was to ensure that Pt was deposited on the pre-exisiting metal, not on the support. Aliquots of about 0.5 mL were taken from the bath at predetermined time intervals to analyze water-soluble Pt^{4+} concentration using atomic absorption spec-

troscopy (Perkin-Elmer AA-400). After ED, all catalysts were filtered and washed with sufficient deionized water (typically 2L for 1g of catalyst). The recovered catalyst powders were dried overnight in a vacuum at room temperature and stored in a sealed vial at ambient conditions.

2.3.2 Catalyst characterization

A Micromeritics ASAP-2020 equipment was used to measure BET specific surface area and pore size distribution by nitrogen physisorption technique. The phase and size of the catalyst NPs were estimated by X-ray diffraction (XRD) analysis. To obtain XRD patterns, a Rigaku MiniFlex-II benchtop diffractometer equipped with a high sensitivity D/tex Ultra Silicon silt detector was used. The XRD patterns were obtained using a Cu-Kα radiation source (λ=1.5406 Å), operated at 30 mA and 15 kV. The XRD measurements were done in the range of 20^o-80^o at a scan rate of 2^o/min and a sampling width of 0.02^o. The XRD patterns were deconvoluted by fitting in Fityk (version 1.3.1) using Gaussian peak shape. The Scherrer equation with an input of half-width at half maximum (HWHM) and a shape factor of 0.94 was applied to calculate the particle sizes. The number of active catalytic sites of the base metal was measured by pulse chemisorption using H_2-titration of oxygen pre-covered metal on a Mincrometitics Autochem II 2920 Analyzer, which has a high-sensitivity thermal conductivity detector for chemisorption measurements. The technique has been described in detail in prior work by Monnier et al. [24]. In brief, the base catalysts were reduced in-situ under flowing H2 at 300 ^{o}C for 3 h and subsequently purged under flowing Ar for 30 minutes to remove all unused H_2 from the analysis tube. Prior to exposing the catalysts in O_2, the catalysts were cooled to 40 ^{o}C in Ar. A gas stream of 10%O_2 balance He was flowed at 40 ^{o}C for 30 min, allowing the formation of Ir (or Ru) O-bonds on the catalyst surface. Afterward, the residual gases and weakly adsorbed O_2 were purged with Ar for 30 min at 40 ^{o}C. Pulses of

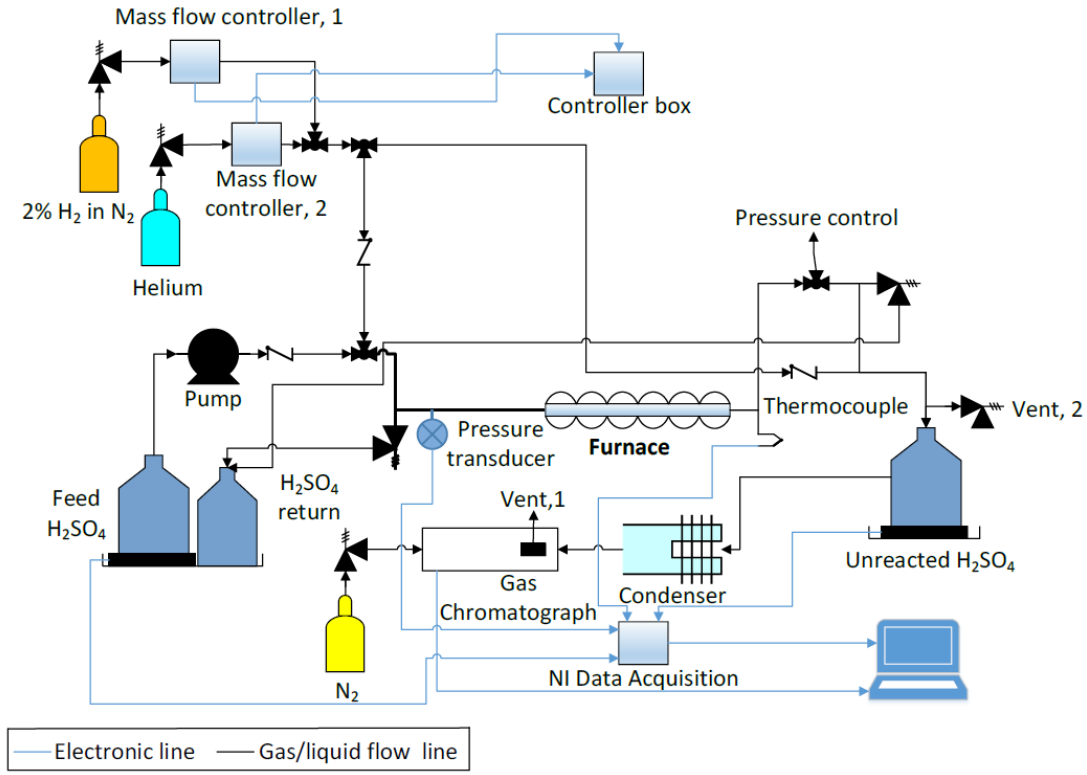

Figure 2.2 A schematic of reactor system used for H_2SO_4 decomposition

10%H_2 balance Ar were dosed every 5 minutes at 40 °C for Pt and Ir until there were no changes in H_2 peak intensities. The H_2 titration stoichiometry (H_2/M) was the same (1.5) for Pt, Ir, and Pt-Ru.

2.3.3 Catalyst evaluations

Catalyst stability at high temperature oxidative conditions was evaluated by calcination at 800°C in static air for 8 hours in a muffle furnace and characterized after each calcination treatment using XRD. The stability of the catalysts was then demonstrated in terms of metal sintering and oxide formation caused by catalyst exposure at these conditions.

To confirm the stability results obtained from XRD analysis, a set of both monometallic and bimetallic catalysts were tested for actual SO_3 decomposition. Evaluation of

catalysts activity and stability for SO_3 decomposition was done at Idaho National Laboratory (INL). The schematic reactor system at INL is shown in Figure 2.2, and the details of the procedure are reported in references [145–147]. In brief, a stream of 96-98 wt% H_2SO_4 was pumped through a high-temperature, tube furnace where H_2SO_4 was simultaneously vaporized and cracked to gaseous SO_3, which was then catalytically reduced to produce SO_2 and O_2 at a temperatures of approximately 800 ^oC. The gaseous SO_2 was adsorbed by a solution of 1N NaOH, and O_2 was vented to atmosphere. The unreacted SO_3 was combined with steam to reform H2SO4, separated by condensation. The condensed H_2SO_4 was periodically collected and examined by typical acid-base titration to estimate the acid conversion. The yield of SO_2 production was estimated by quantifying the amount of SO_2 adsorbed in NaOH solution using standard iodometric titration. Alternatively, the NaOH scrubber could be bypassed and gas phase SO_2 and O_2 analyzed by gas chromatography to provide more real-time data analysis.

2.4 Results and Discussion

2.4.1 Stabilization of Catalyst Support

The as-received TiO_2 and BN supports were subjected to calcination treatments at different hold temperatures. Powder XRD profiles of the supports before and after calcination are shown in Figure 2.3. Corresponding values of BET surface area measurements of both supports, using nitrogen physisorption, are reported in Figure 2.4. The XRD analysis of TiO_2 showed that the as-received sample is composed mostly of anatase TiO_2 [ICSD card no. 01-075-2552]. Calcination treatment induced structural changes for samples exposed at or above 700 ^oC, as indicated by the formation of peaks corresponding to rutile phase TiO_2 [ICSD card no. 01-072-1148], accompanied by diminished intensities of the anatase pattern. Complete transition to rutile

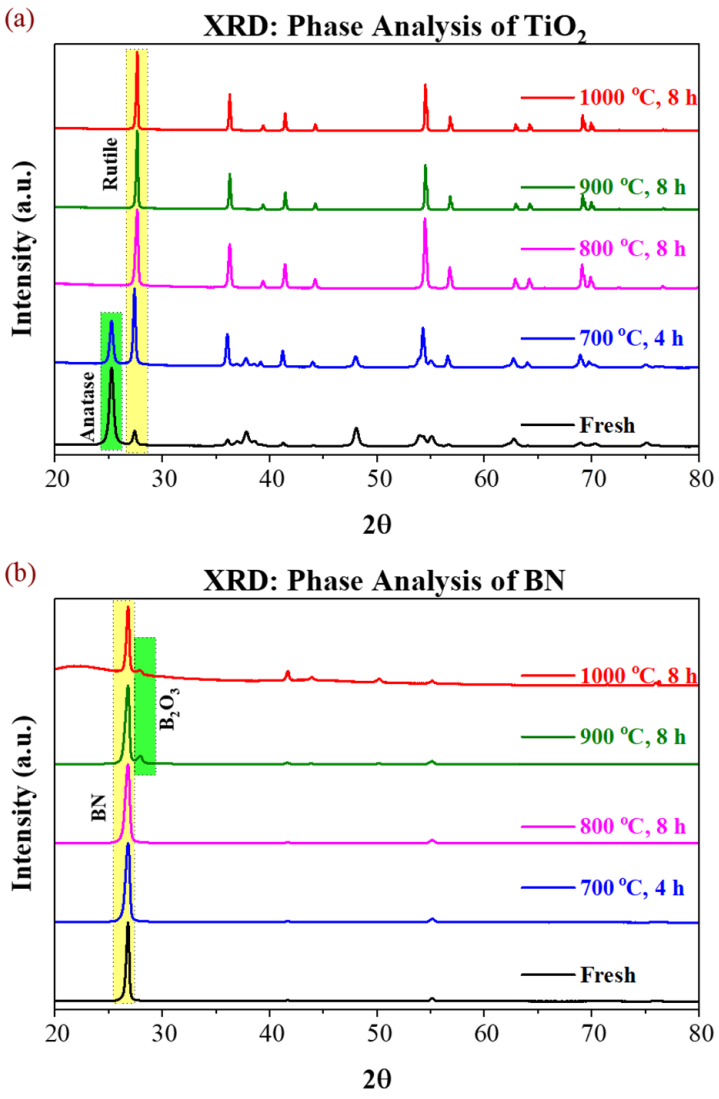

Figure 2.3 Powder XRD profiles of fresh and calcined supports: TiO_2 (left) and BN (right).

was observed for the 800 °C calcined sample, which agrees with reported transition conditions of TiO_2 [150]. For the BN support, there was no significant difference in the diffraction patterns of samples treated with calcination up to 800 °C. However, increasing the temperature to 900 °C resulted in the appearance of the oxide phase, B_2O_3, which became more evident after 1000 °C calcination. This result is consistent

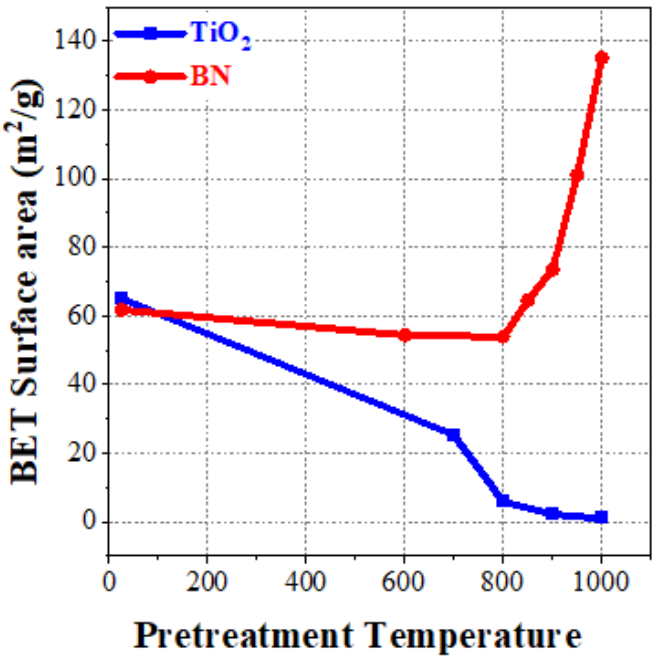

Figure 2.4 BET surface area measurements of support powders.

with the findings on BN oxidation reported in the literature [166].

The physical changes of the supports under high-temperature calcination were also manifested in the results of the nitrogen physisorption analysis. The BET specific surface area of TiO_2 drastically dropped from 65.1 to 25.3 m^2/g after calcining at 700 °C. While the surface area continued to decline with increasing temperature, the decrease was less prominent after 800 °C. This loss of surface can be attributed to the irreversible transition of the crystalline structure of the TiO_2 from metastable anatase to stable rutile [150, 167–170]. Conversely, BN had much better stability than TiO2 and surface area decreased only from 61.8 to 53.9 m^2/g at 800 °C calcination. However, increasing the calcination temperature to 1000°C increased the surface area to 135.2 m^2/g. This may be explained by the oxidation of BN to B_2O_3 [166, 171], the formation of the oxide being detected in XRD. This results in defects at higher oxidation temperatures that could form pores on the stacked, planar structure of BN

to increase surface area. A pore analysis of the calcined BN samples, shown in Table 2.1 confirms the formation of micropores, giving a smaller average pore diameter or greater fraction of micropores at higher calcination temperatures.

Table 2.1 Nitrogen porosimetry measurements of BN samples.

Sample	BET surface area $[m^2/g]$	V_{pore} $[cm^3/g]$	D_{mean} [nm]
BN-fresh	61	0.21	13.7
BN-600 °C	54	0.18	13.8
BN-800 °C	53	0.17	13.1
BN-900 °C	73	0.13	7.4
BN-950 °C	100	0.11	4.6
BN-1000 °C	135	0..11	3.5

The structural changes of the support materials, i.e., the transition of TiO_2 from anatase to rutile and the oxidation of BN, when exposed to high-temperature oxidative conditions such as those in SO_3 decomposition, indicate possible and extrinsic sources of catalyst deactivation [172], and that activity losses for TiO_2-supported catalysts may be due to collapse of the support and not just sintering of Pt. Prior studies have shown evidence of sintering of Pt supported on TiO_2 after SO_3 decomposition at temperatures above 750 °C [145–147]. However, surface and pore changes can result in particle migration or Pt occlusion if catalyst synthesis is done on untreated supports. Inducing changes through calcination treatment prior to adding metal nanoparticles can be beneficial, such that additional exposures to similar oxidative conditions will have decreased effect on the support surface. Thus, all supports were pretreated by static air calcination at 800 °C for 8 h prior to catalyst synthesis. This calcination treatment is referred to as standard calcination treatment.

2.4.2 Monometallic Platinum catalyst stability

TiO_2 and BN support after standard calcination were used to prepare supported

Pt catalysts at 1 wt% metal loading, that were synthesized by IWI and reduced at 300 °C in a flow of 20%H_2/ balance He for 2 h. After synthesis, catalysts were subjected to a second standard calcination to determine the stability of the Pt NPs on these materials. The XRD patterns of the 300°C reduced (fresh) and after second 800°C calcination samples are shown in Figure 2.5 for both TiO_2 and BN supported samples. A relatively small but detectable peak corresponding to Pt(111) reflection (2θ = 39.8°) could be discerned from the diffraction pattern of the fresh 1% Pt/TiO_2 sample. After support pattern subtraction and peak fitting, size estimation using the Scherrer formula gave 11.6 nm Pt particle sizes. The formation of Pt particles this large may be due to the lower surface area of the pretreated TiO_2 support that provided less surface for Pt dispersion. Conversely, fresh 1% Pt/BN show no diffraction peaks corresponding to any Pt phases, indicating particle sizes below the detection limit of the instrument (<1.5 nm) [173].

After the second standard calcination, the patterns for the monometallic catalysts on either support showed sharp peaks corresponding to the face-centered cubic (fcc) Pt phase [NBS Card no. 00-004-0802], confirming that the pt loading metal is sufficient enough to be detected by the instrument. Estimation of Pt particle sizes by XRD revealed that the (second) calcination 1% Pt/TiO_2 catalyst had sintered to 33.5 nm. In comparison, the (second) calcination 1% Pt/BN catalyst, the Pt particles were estimated to be 13.2 nm. The smaller Pt NPs on BN after calcination signify better stability than TiO_2 support. However, the particle growth after calcination at 800 °C still indicated that Pt sintering at reaction conditions could be expected.

2.4.3 Bimetallic Catalyst Synthesis

The concept of Pt stability by SFE difference between two metals for supported catalyst stabilization has been demonstrated in a previous study [158]. This study hypothesized that depositing Pt (SFE = 2.691 J/m^2 at 298.2 K) on the higher SFE

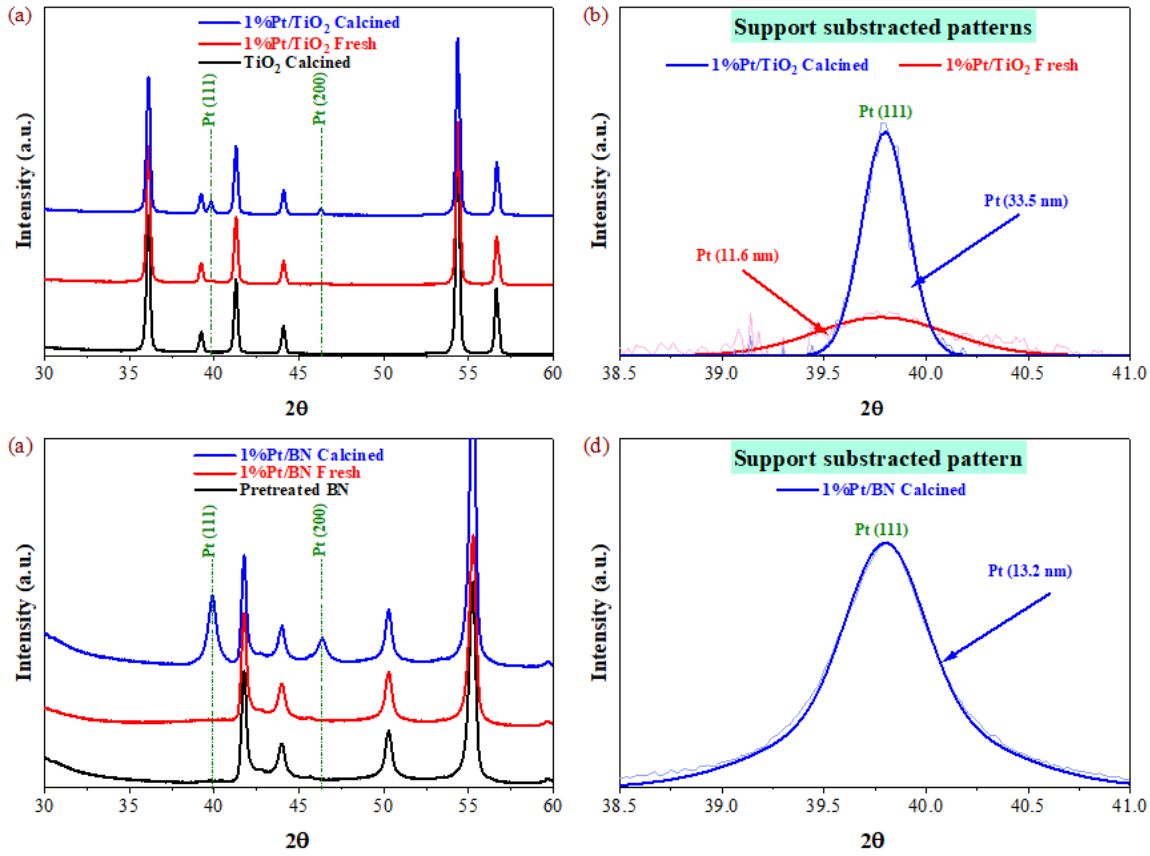

Figure 2.5 XRD patterns with Pt (111) peak fitting of monometallic catalysts: (a, b) 1% Pt/TiO_2 and (c, d) 1% Pt/BN. Peaks was fitted after corrosponding support substraction.

metal such as Ir (SFE = 3.231 J/m^2 at 298.2 K) [174] on a support could reduce Pt sintering, thereby maintaining the lowest system free energy to give a more stable catalyst. Migration of Pt from the Ir surface would increase the overall free energy of the Pt-Ir-cupport system. The ED technique was applied for synthesis of all bimetallic catalysts in this work. In a typical ED process, a secondary metal is deposited on a primary metal when the seed catalyst (primary metal dispersed on the support) is immersed in an ED bath, containing an aqueous solution of the secondary metal precursor salt, a stabilizing or chelating agent, and am organic reducing agent [24–26]. The current work used Pt as the secondary metal and Ir as the primary metal. The composition of the ED bath for deposition of Pt on Ir was the same as used for the

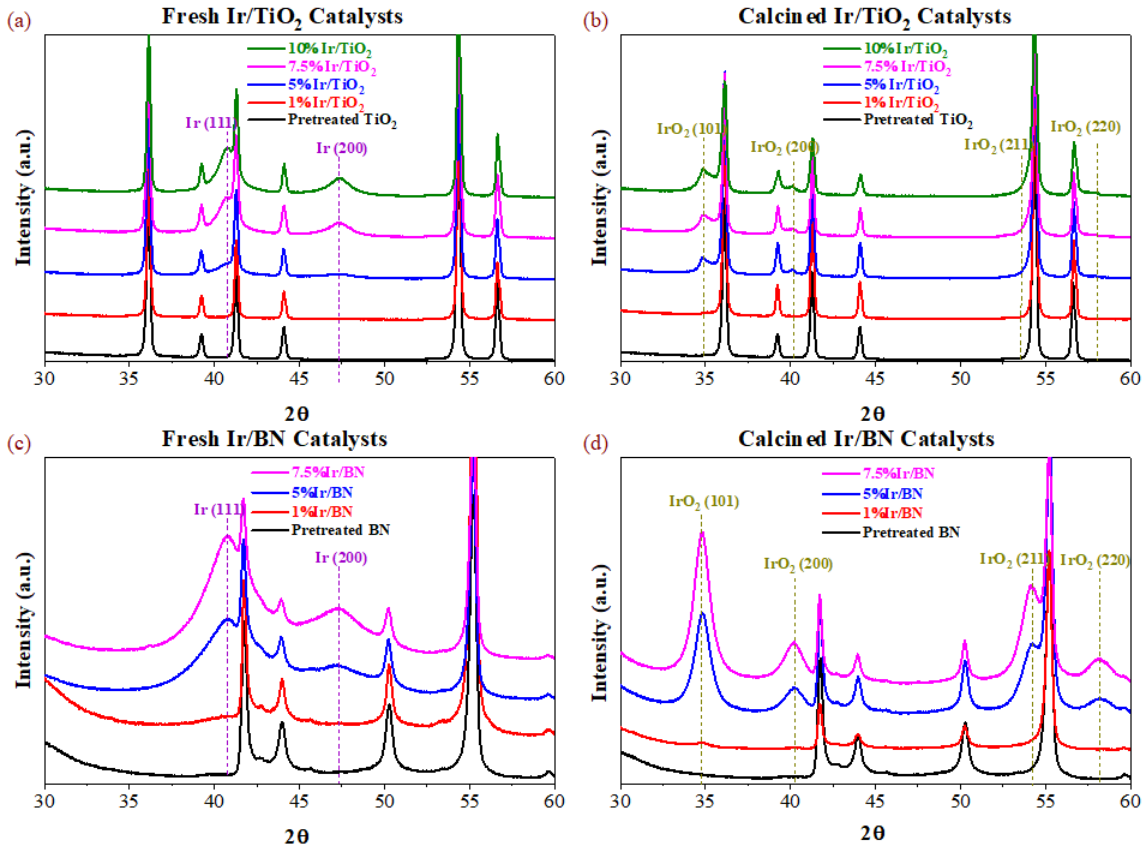

Figure 2.6 XRD profiles of Ir seed catalysts after reduction at 300°C (left) and a second calcination at 800°C (right).

ED of Pt on Ru by Diao et al. [24]. Finally, Ir weight loadings were varied between 1 and 10% on both TiO_2 and BN to increase the amount of Pt that could be deposited and maintained on the Ir surface.

The stability of the Ir catalysts was evaluated by pre-treatment at standard calcination conditions. XRD of the fresh and calcined samples are shown in Figure 2.6. For all fresh catalysts (after reduction at 300°C), increasing the Ir loading increased the intensity of peaks corresponding to fcc Ir metal [NBS Card no. 00-006-0598]. In addition, oxidation of the Ir on these catalysts occurred after standard calcination to form IrO_2. The metallic surface areas of the fresh Ir catalysts were determined using H_2 chemisorption; the results are shown in Figure 2.7. As expected, higher Ir

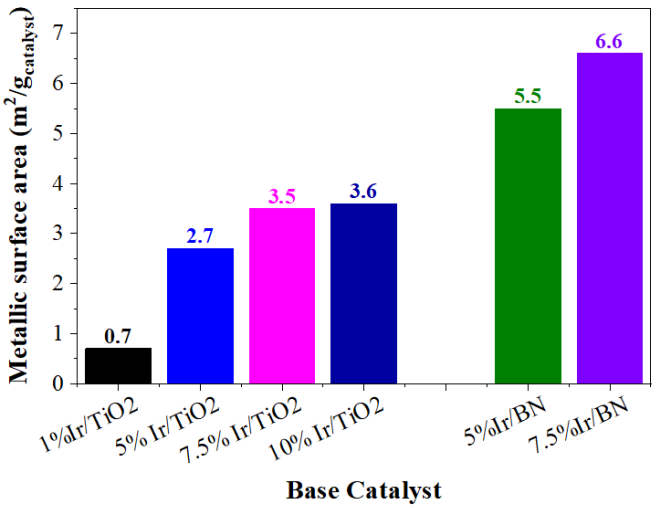

Figure 2.7 Ir surface areas for the different Ir seed catalysts determined by chemisorption.

loadings gave larger metallic surface areas due to the formation of more Ir NPs since the XRD patterns revealed insignificant growth of Ir particles for higher Ir loadings on both supports (details in Table A.1). However, the accessible metallic Ir on the treated TiO_2 support reaches a maximum of 3.6 m^2/g-catalyst for the 10% Ir/TiO_2, which is lower than the 6.6 m^2/g-catalyst Ir surface obtained from the 7.5% Ir/BN catalyst. This may be due to the lower surface area of the TiO_2 support, giving less surface for the Ir to disperse.

Bimetallic Ir-Pt catalysts were prepared with ED, and a plot of the deposition kinetics for selected samples is shown in Figure 2.8. The stability of the electroless developer bath was determined in the first 30 min of the experiment, where no reduction and precipitation of Pt^0 from at solution containing $PtCl_6^{2-}$, DMAB reducing agent, and ethylenediamine (EN) was observed. After addition of the Ir catalysts at 30 min, the concentration of $PtCl_6^{2-}$ dropped due to activation of DMAB by Ir and reduction of the Pt precurosr on the Ir surface. The slopes of the Pt concentration-time profiles during ED indicate the deposition rate. For example, the 7.5% Ir/TiO_2

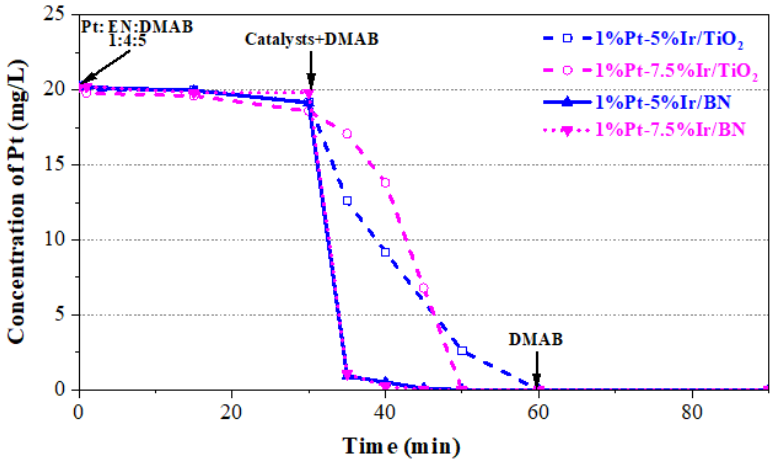

Figure 2.8 Deposition kinetics of Pt on supported Ir seed catalysts.

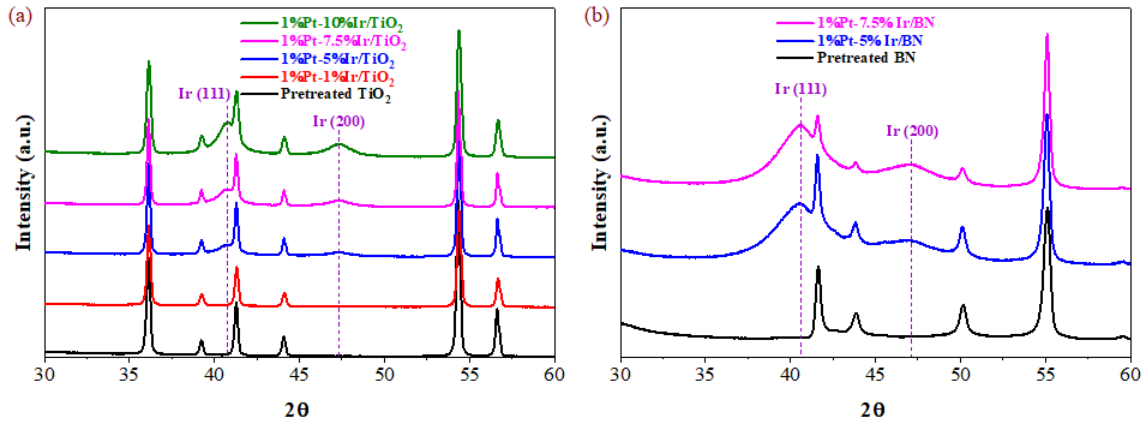

Figure 2.9 XRD patterns of fresh (reduction at 300°C) bimetallic Ir-Pt catalysts, Ir-Pt/TiO_2 (left) and Ir-Pt/BN (right). Normal position of Pt(111) and Pt(200) at 2θ=39.8 and 46.2, respectively

seed catalyst had a faster deposition rate than 5% Ir/TiO_2 due to the higher Ir surface for activating the reducing agent and subsequent reduction of Pt. This was also the reason for the much steeper slopes of the deposition profiles on BN-supported catalysts.

XRD analyses were carried out on the fresh bimetallic catalysts, and the diffraction patterns are shown in Figure 2.9. The profiles of the Ir-Pt samples match those

of the corresponding seed catalysts containing only Ir. The absence of any Pt peaks peaks suggests the deposited Pt metal was below the size detection limit of the instrument or dispersed as thin rafts on the Ir surface as predicted by the ED process.

2.4.4 Bimetallic Catalyst Stability

A second standard calcination treatment was done to determine the sintering characteristics of the bimetallic catalysts. The size growth of the nanoparticles and other structural changes were analyzed from ex-situ XRD and are shown in Figure 2.10. Similar to the calciination of the Ir catalysts (before ED of Pt), some oxidation of Ir to IrO_2 was also observed. The emergence of Pt fcc peaks indicates Pt metal sintering did occur after the second calcination treatment. Visual inspection of the Ir-Pt/TiO_2 profiles reveals an inverse relationship between the sharpness and intensity of the peaks for Pt with respect to the Ir loading. Higher Ir amounts resulted in less intense or broader Pt peaks. By careful deconvolution of the Ir, Pt, and IrO_2 peaks from the diffraction patterns for the fresh and calcined bimetallic catalysts, particle size estimates were calculated using the Scherrer formula listed in Table 2.2.

For the TiO_2 support, the growth of Pt particles after calcination was less pronounced at higher loadings of Ir. This was likely due to the higher amount of Ir that gave more metallic surface for the anchoring of Pt. While the Ir did oxidize to form IrO_2, the growth of the oxide particles was not drastic, thereby minimizing the destabilization of the deposited Pt.

Additionally, the occlusion of Ir by Pt on the surface may have aided in inhibiting the oxidation and sintering of the Ir phase [158]. For the calcined Ir-Pt/BN catalysts, the Pt NP size was larger for the higher loading, 7.5 wt% Ir sample, which also had a larger IrO_2 size. The drastic growth of Ir particles, which reduced the surface for anchoring, coupled with structure change during oxidation, likely promoted the sintering of Pt. Despite the sintering of the Ir-Pt/BN catalysts, the growth of Pt was

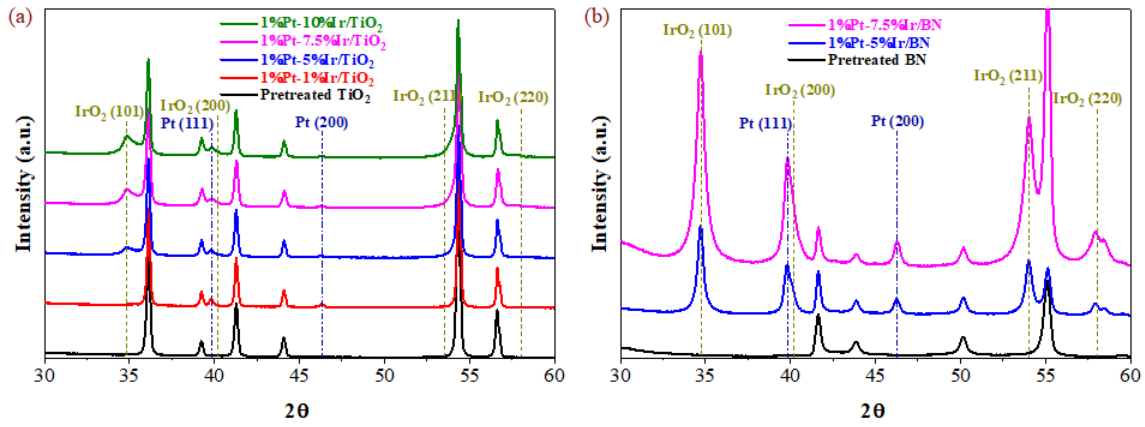

Figure 2.10 XRD patterns of calcined bimetallic Ir-Pt catalysts: Ir-Pt/TiO_2 (left) and Ir-Pt/BN (right).

Table 2.2 XRD particle size estimates of Pt and Ir phases of bimetallic catalysts after 300°C reduction and after a second 800°C calcination.

Catalyst	Fresh [nm]		Calcined [nm]	
	Pt	Ir	Pt	IrO_2
1%Pt-1%Ir/TiO_2	-	-	27.6	-
1%Pt-5%Ir/TiO_2	-	4.7	24.5	-
1%Pt-7.5%Ir/TiO_2	-	5.6	22.1	11.0
1%Pt-10%Ir/TiO_2	-	5.9	21.0	9.0
1%Pt-5%Ir/BN	-	2.8	11.4	14.7
1%Pt-7.5%Ir/BN	-	3.2	16.4	22.1

still less than when supported on TiO_2. The higher metallic surface area of Ir on the BN provided greater stability for the deposited Pt. The larger BN surface area may have also further aided in stabilizing the particles.

2.4.5 Evaluation of Catalysts for SO_3 Decomposition

The fresh catalysts were evaluated for performance in the decomposition reaction of SO_3. The reactor temperature was set at 800 °C, the same as the standard calcination treatment. Each reaction experiment lasted for 72 h time on stream, and the SO_2 production rates are shown in Figure 2.11. The 1% Pt/TiO_2 catalyst gave the

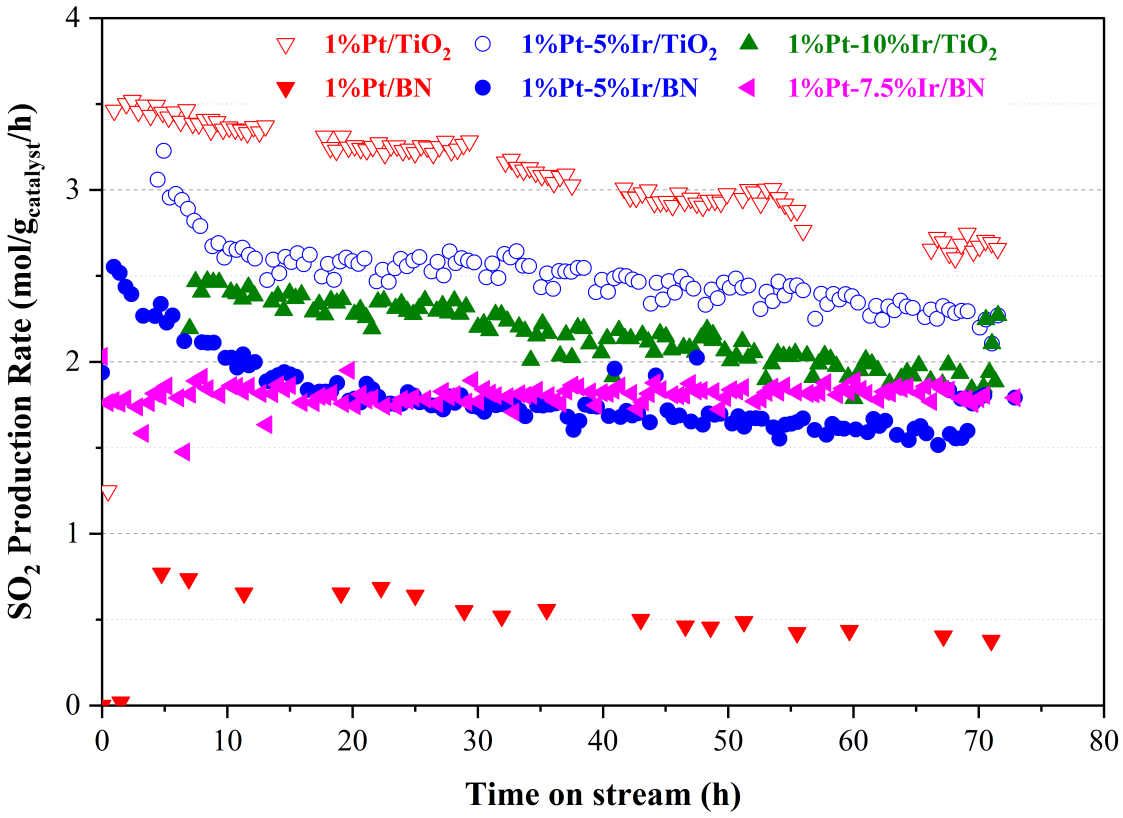

Figure 2.11 XRD patterns of calcined bimetallic Ir-Pt catalysts: Ir-Pt/TiO_2 (left) and Ir-Pt/BN (right).

highest rate of SO_2 production; however, there was a significant decrease in activity throughout the evaluation. The drop-in activity is less than reported in the literature using Pt/TiO_2 catalysts, suggesting that the support pretreatment helped stabilize the catalyst [145, 146]. The slow deactivation trend can be due to continued sintering and oxidation of Pt and structural changes of the TiO_2 as observed in prior ex-situ experiments [145]. On the other hand, the 1% Pt/BN catalyst had the lowest activity.

In addition, the bimetallic Ir-Pt/TiO_2 catalysts had a lower SO_2 production rate than 1% Pt/TiO_2, although still higher than cited literature [145, 146]. The lower activity can be due to decreased Pt to TiO_2 interaction as Pt particles were deposited on Ir surface and not on TiO_2. The milder activity loss through time for the bimetallic catalysts than the monometallic catalyst suggests better stability under reaction

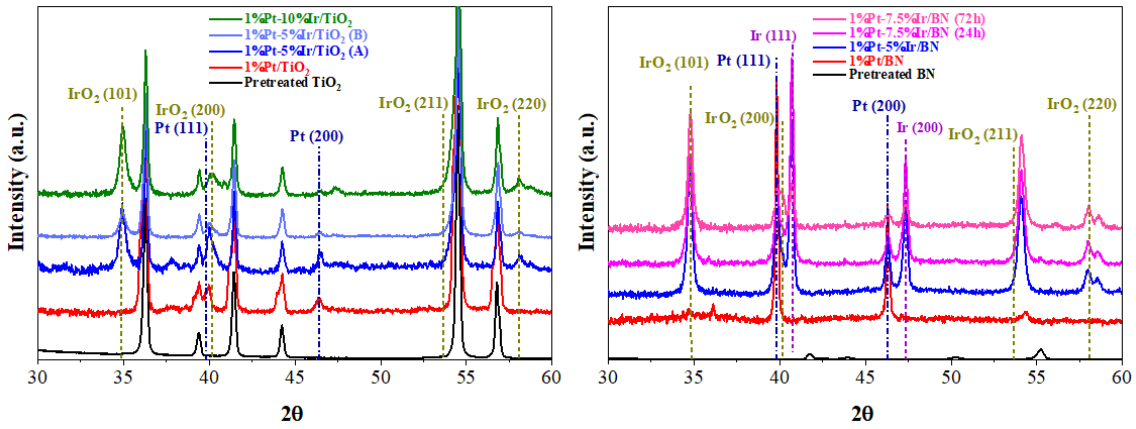

Figure 2.12 XRD patterns of spent catalysts supported on TiO_2 (left) and BN (right).

conditions. On BN, the Ir-Pt/BN catalysts have higher activity than 1% Pt/BN. The SO_2 production rates using Ir-Pt/BN catalysts were slightly lower than Ir-Pt/TiO_2 but showed better stability. The 1% Pt – 7.5% Ir/BN catalyst had the most stable activity with no observable loss in catalytic performance.

Ex-situ XRD analysis of the spent catalyst samples shown in Figure 2.12 indicated rapid sintering during the 1%Pt/BN sample evaluation, giving rise to larger particles, 63 nm, resulting in low catalytic activity. The estimated particle sizes of the spent catalyst are presented in Table 2.3. These calculated particle sizes correspond with the trend in catalyst performance where samples that have sintered to form larger particle sizes had lower activity. While BN supported catalysts had undergone sintering of Pt, the stability during evaluation suggests robustness of the Pt-Ir/BN system can be a synergistic effect of the BN to support nanoparticles and the anchoring of Pt on the Ir surface.

2.5 Conclusions

This study prepared, evaluated, and characterized a series of Pt-based catalysts

Table 2.3 XRD particle size estimates of Pt of spent (post-tested) catalysts.

Catalyst	Pt NPs size [nm]	
	TiO_2-supported	BN-supported
1%Pt	20	63
1%Pt-5%Ir	19*	29
1%Pt-7.5%Ir-24 h	Not measured	24
1%Pt-7.5%Ir-72 h	Not measured	19
1%Pt-10%Ir	14	Not measured

* measured twice (known as A and B) and found identical particle size

supported on both TiO_2 and BN. TiO_2 supported monometallic Pt catalyst is highly active but has low stability for SO_3 decomposition. The significant loss of the TiO_2 surface, as a result of high-temperature exposure, and Pt sintering causes rapid deactivation. The stabilization of TiO_2 through pretreatment by calcination at 800 °C improved the stability to some extent. Evaluation for SO_3 decomposition still indicated activity degradation with exposure to the harsh reaction conditions under high temperature and corrosive, oxidative environment. BN was shown to have a highly stable surface under high-temperature calcination. However, in SO_3 decomposition, monometallic Pt NPs on BN support quickly sintered and deactivated. Stabilization of the Pt was achieved by electroless deposition on Ir, taking advantage of the higher SFE Ir as anchoring surface for low SFE Pt. Evaluation of Pt-Ir bimetallic compositions supported on TiO_2 and BN showed improved catalyst stability compared to monometallic Pt catalysts. Pt-Ir formulations supported on high surface area BN were determined to have the best stability, suggesting improved anchoring of NPs on the support surface and reduced mobility of Pt through deposition on Ir surface.

Chapter 3

The Stabilization of Ultrasmall Platinum Nanoparticles by Nitrogen-doped Carbon

3.1 Abstract

Carbon-supported Pt NPs have numerous applications, including fuel cell electrodes and heterogeneous catalysts. The effective application of these materials will be greatly advanced by the ability to control the oxidation and sintering of the NPs by modifications of the carbon support. One attempt of such control has been doping carbon supports with nitrogen. In this work, a cutting-edge, high sensitivity, in-situ XRD instrument, which allows observation of ultrasmall Pt NPs, has been combined with in-situ XPS to provide unprecedented clarity in the characterization of supported Pt NPs in oxidizing and high-temperature environments. On a nitrogen-doped carbon support derived from poly-phenylporphyrin, Pt NPs show increased stability to oxidation and thermal sintering. The enhanced Pt-support interaction arising from the N dopant versus the N-free carbon is manifested by (1) decreased initial Pt particle sizes, (2) small particle size at higher surface densities, (3) increased resistance of Pt NPs to oxidation, (4) increased electron binding energy of Pt^0, and (5) increased resistance of Pt NPs to sintering. It is expected that the higher stability of Pt on NC will be manifested in higher activity in applications such as fuel cells and catalytic reactions.

3.2 Introduction

Heterogeneous materials comprising Pt NPs on carbon supports have numerous applications, including fuel cell electrodes [53–57] and catalysts for hydrogenation [47–52] and oxidation [175–182] reactions. To enable future applications, it will often be critical to maximizing the number of active catalytic sites per mass of Pt by minimizing the size of the NPs. As the NPs become ultra-small (< 2 nm), however, they are prone to oxidization at ambient conditions, as demonstrated in recent XRD studies using synchrotron radiation [183] and benchtop powder XRD with a high

sensitivity silicon strip detector [173, 184, 185]. While for some reactions this is beneficial [186–191], for others this can lead to a loss in reactivity [190–195], and can eventually lead to sintering of the Pt phase into larger particles and a corresponding loss of catalytically active sites [192, 196–199]. In either case, the effective application of these materials will be greatly advanced by the ability to control the oxidation and sintering of the NPs by modifications of the carbon support.

One attempt of such control has been doping carbon supports with nitrogen; N atoms form irregular and disrupt edge plane defects which provide higher densities of nucleation sites during NP genesis from deposited metal precursors, resulting in high NP density and uniformly distributed, smaller particles on the surface [27–30]. Also, doped N atoms within the carbon structure have higher electronegativity than C atoms and strongly interact with metals [29, 200–202]. While a reduction in average NP size by N-doping has been recognized in the literature, its effect on the oxidative stability of Pt NPs has not been adequately understood to date. Furthermore, the interpretation of XPS analysis of these systems [202–206] is inconsistent; the observed Pt^{2+} and Pt^{4+} valences have been attributed to Pt-N interactions [202, 205], or Pt oxidation [202, 205, 206], while some reports do not discuss the observed higher valences [203, 204].

The ability to distinguish oxidized and reduced ultra-small Pt NPs (on the order of 1 nm) via high sensitivity XRD sheds much light on this system. This data, combined with XPS analysis utilizing an in-situ pretreatment chamber, has allowed a clear and consistent picture of NP behavior to emerge. The poly-phenylporphyrin-derived N-doped carbon studied in this work stabilizes Pt NPs to oxidation as well as to thermal sintering, and the effect of Pt NP size on both properties has been isolated. With the combination of high sensitivity XRD and XPS with in-situ pretreatment, it can be concluded that the higher valences of Pt observed by XPS come from Pt NP oxidation, which can occur with room temperature exposure to air, and that the

true signature for Pt-N interaction is not higher Pt valences, but rather, an upward shift in the Pt^0 electron binding energy.

3.3 Experimental

3.3.1 Materials

Two different carbon materials, including poly-phenylporphyrin-derived (surface area 900 m^2/g, denoted NC) and Black Pearls-2000 (surface area 1400 m^2/g), were studied in this work. The NC support was derived from terephthalaldehyde by a high-temperature pyrolysis process (details in Appendix-B). Black Pearls-2000 (denoted C), a commercially used carbon black, was obtained from Cabot. In most cases, hydrogen hexachloroplatinate (IV) hydrate (H_2PtCl_6, 99.98%) was used as the anionic metal precursor; for dry impregnation preparations, sodium tetrachloroplatinate (II) hydrate (Na_2PtCl_4, >99%) was used. Both were purchased from Sigma-Aldrich. In addition, sodium hydroxide (NaOH, 10 N, Rica Chemical Company) and hydrochloric acid (HCl, 37%, Sigma Aldrich) were used to adjust the pH of the precursor solutions.

3.3.2 Metal deposition, nanoparticle genesis, and characterization

SEA was employed to synthesize most of the supported NPs studied. SEA is a wet impregnation synthesis method in which charged metal precursors are adsorbed onto an oppositely charged support surface [86, 207, 208]. In this case, an anionic Pt hexachloride precursor is strongly adsorbed onto a positively charged carbon surface [208]. First, the supports were weighed out to attain a surface loading of 500 m^2 carbon/L of solution. Next, the required concentration of precursor solution was contacted with the support for an hour at the optimal pH (see Table 3.1). A stirrer was used to ensure uniform contact between support and metal precursor, operated at 140 rpm speed. Afterward, the catalyst slurry was filtered using a vacuum pump

Table 3.1 Metal adsorption on carbons by SEA

Catalyst	BET surface area [m^2/g]	SEA pH	Deposited metal density [$\mu mol/m^2$]	Weight loading [%]
Pt/NC	900	1.50	0.81	12.5
Pt/C	1400	2.50	0.26	6.5
		2.75	0.51	12.1
		2.75	0.87	18.9

and dried in ambient air overnight, then dried in static air at 120 °C for 8 h. The final weight loading of Pt on carbons was measured utilizing the concentration difference between solutions before and after the adsorption. A Perkin-Elmer Optima 2000DV ICP-EOS instrument was used to estimate the metal concentration in the solutions.

The dry impregnation (DI) method was used to synthesize control samples for Pt/NC and Pt/C catalysts, including 12.1%Pt/C, 18.9% Pt/C, and 12.5%Pt/NC, where an aqueous solution of the appropriate concentration of Na_2PtCl_4 was introduced into carbon supports to incipient wetness. The impregnated catalysts slurries were subsequently dried and reduced using the same method applied for SEA catalysts.

STEM characterization

An aberration-corrected JEOL 2100F STEM equipped with a 200kV field emission electron gun and a double tilt holder was used to obtain Z contrast images. The tilting holder can tilt the sample across a range of angles ($\pm$ 20°). High angle annular dark-field (HAADF) STEM images were acquired on a Fischione Model 3000 HAADF detector with a camera length. The inner cutoff angle of the detector was 50 mrad [209]. To perform STEM imaging, catalyst samples were suspended in isopropanol, and a drop of the suspension was deposited onto a holey carbon film attached to a Cu-TEM grid. A digital micrograph software was used to record images, and particle

size distribution was obtained by counting more than 1000 particles on each sample.

XPS characterization

In-situ X-ray photoelectron spectroscopy (XPS) analysis was carried out using a Kratos AXIS Ultra DLD XPS (Kratos Analytical). The XPS system is equipped with a monochromatic Al Kα source operated at 15 keV and 150 W, a hemispherical analyzer, charge neutralizer, catalysis cell, and a load lock chamber for rapid introduction of samples without breaking vacuum. The X-rays were incident at an angle of 45°, with respect to the surface normal. Analysis was performed at a pressure of 1×10^{-9} mbar, and high-resolution core-level spectra were measured with a pass energy of 40 eV. In XPS experiments, an electron beam was directed on the sample for charge neutralization. The curve fitting procedure was carried out using the XPS Peak41 software. The peak approximation was carried out using Gaussian - Lorentzian functions, with subtraction of Shirley-type background. The in-situ reduction of the materials was performed in a reaction cell (Model: ES-009R01) directly attached to the XPS chamber, which allows the sample to be treated at gas flow conditions. The samples were transferred inside the reaction cell and back to the analysis chamber without exposure to the atmosphere.

XRD characterization

A Rigaku SmartLab SE X-ray diffractometer equipped with a D/tex Ultra 250 1D silicon strip detector was used in this study for in-situ XRD measurements. A cross-beam optics module is attached to the equipment, which switches between the parallel beam and Bragg-Brentano mode without altering the optics. Additionally, it contains a corrosion resistance high-temperature reactor (Reactor-X), which permits measurement to be performed at temperatures 1000 °C in different reaction environments, including vacuum, reactive gas, inert gas, or a mixture of these. An

infrared heating technique is employed in the reactor, which enables quick heating and cooling of the samples, and exhibits good temperature stability. XRD patterns were recorded using Cu-Kα radiation (k=1.5406 Å) operated at 30 mA and 15KV with a scanning rate of 3°/min and sampling width of 0.01°. The 2θ range of 20-80° was employed.

The pre-dried samples of Pt-complex containing support were further dried in SmartLab SE equipment under flowing He at 120 °C for 30 min to ensure no water was present in the sample. The dried samples were subsequently reduced in a flowing 20%H_2 balance Helium (He) at 300 °C for an hour to convert Pt complex into metallic Pt NPs and measured XRD to identify different phases of Pt formed after reduction. Afterward, the reduced catalysts were cooled to 30° and measured XRD. Before the oxidation of Pt NPs, He gas was flown for 30 minutes through the reactor to purge all remaining H_2 from inside the chamber. A stream of pure air was flown across the samples to oxidize the sample as XRD measurements were made at temperatures between 25 °C and 300 °C. The samples were kept at a constant stage temperature for 30 minutes before scanning for a stable temperature to measure XRD. The temperature ramp rate was 10 °C/min with airflow at 100 sccm.

The heat treatment study was conducted under flowing He, where the in-situ reduced NPs were heated at temperatures between 25 to 900 °C. Like the oxidation study, the materials were stabilized 30 minutes prior to XRD measurements at each temperature. The temperature ramp, gas flow rate, XRD scanning rate, and 2θ range for XRD measurements were the same as the oxidation study.

3.4 Results and discussions

A micrograph of the N-doped carbon support (denoted NC, 900 m^2/g) without metal is shown in Figure 3.1a, and in Figure 3.1b with 12.5 wt% (surface density 0.81 μmol Pt/m^2) Pt NPs (denoted Pt/NC) of average size 1.1 nm, deposited by

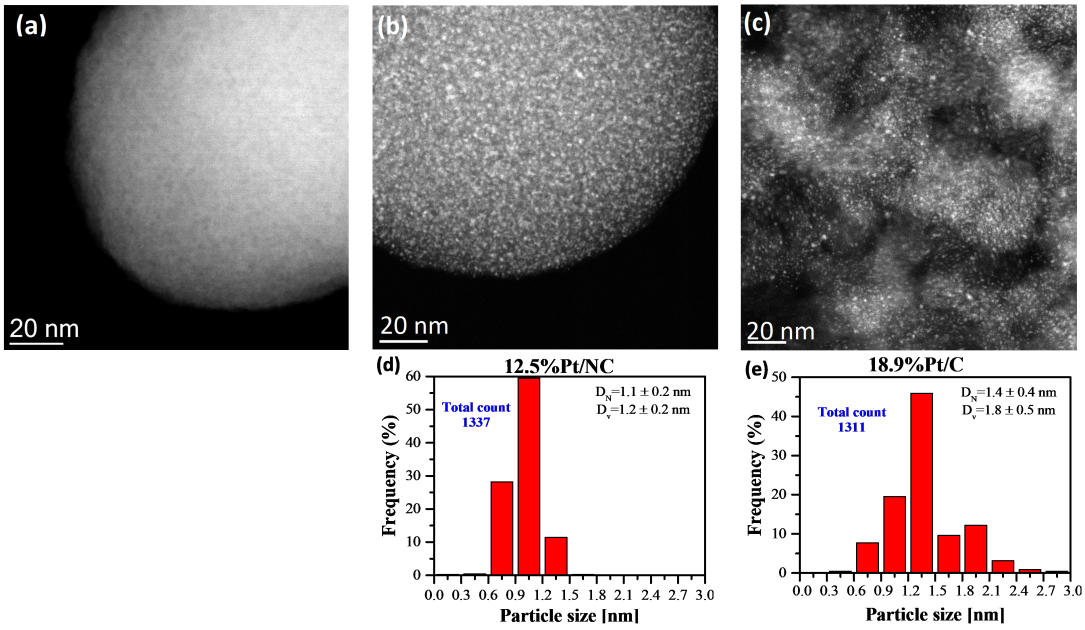

Figure 3.1 STEM images with particle size distributions for (a) NC, (b,d) 12.5%Pt/NC and (c,e) 18.9%Pt/C.

strong electrostatic adsorption [86, 207, 208]. Imaged in Figure 3.1c for comparison is to a nitrogen-free high surface area carbon black (BP 2000, 1400 m^2/g) onto which approximately the same surface density (0.87 µmol Pt/m^2, 18.9 wt%) of Pt (denoted Pt/C) was deposited. Both metal-containing materials had undergone a 300 °C reduction in 20% H_2/80% He to generate the NPs from the adsorbed Pt precursors. The particle size histograms in Figure 3.1d and Figure 3.1e reveal a smaller average particle size and a tighter size distribution of Pt/NC relative to Pt/C. In addition, the number and volume average diameters for the Pt/NC at 1.1 and 1.2 nm are significantly lower than the values for Pt/C, 1.4 and 1.8 nm, respectively. The influence of the N dopant is thus manifested after the initial reduction.

First, the oxidative stability of these two materials was compared with in-situ XRD. The in-situ protocol is illustrated in Figure 3.2a. It consisted of an initial drying step, 300 °C H_2-reduction, cooling to room temperature and then oxidation in air at

incrementally higher temperatures with accompanying XRD measurement, indicated with asterisks (details in Appendix-B). The diffraction patterns for the 12.5%Pt/NC sample are shown in Figure 3.2b, first for the metal-free support (bottom pattern), and then the reduced sample at 300 °C and cooled to room temperature (2nd and 3rd patterns from the bottom), followed by patterns in the air at successively higher temperatures. As oxidation occurs, the diffracted peaks broaden and shift to the left as Pt oxides form as observed previously for carbon and oxide-supported Pt particles [184, 210, 211]. The same leftward shift in broad XRD Pt peaks of air-exposed Pt/NC can actually be seen in two previous reports [203, 206] (Figure 2 of each reference) but was not recognized as oxidation. Figure 3.2c accentuates the difference of the fully reduced versus fully oxidized sample by comparison with the background.

With careful background subtraction and fitting as developed in previous studies [185, 209, 210] and described in detail in the Apendix-B with Figures B.3 and B.4, the peaks can be fit as shown in Figure 3.2d. The fully reduced sample is fit with Pt (111) and (200) fcc peaks with FWHMs, per the Scherrer equation, corresponding to a size of 0.98 nm. (Figure B.5 displays fits of all reduced samples at 300 °C and room temperature.) The fully oxidized sample required the presence of an intermediate Pt oxide, Pt_3O_4, as well as a fully oxidized phase, PtO_2, all in size range of 0.96 – 0.98 nm. While at first glance, the fully oxidized pattern appears to have lower overall intensity than the fully reduced pattern, when the overall fitted patterns are overlaid, as in Figure 3.2e, it is seen that the integrated area of the oxidized sample drops only seven percent. This slight decrease may be caused by slightly increased X-ray absorption, and a corresponding decreased sampling volume, accompanying the mass gain of the Pt phase from the metal oxidation.

Three snapshots of the progression of oxidation of the Pt/NC sample are shown in Figure 3.3a-c (full set in Figure B.4). These show an initial room temperature oxidation of a small amount of Pt_3O_4 and then the combination of Pt_3O_4 and PtO_2

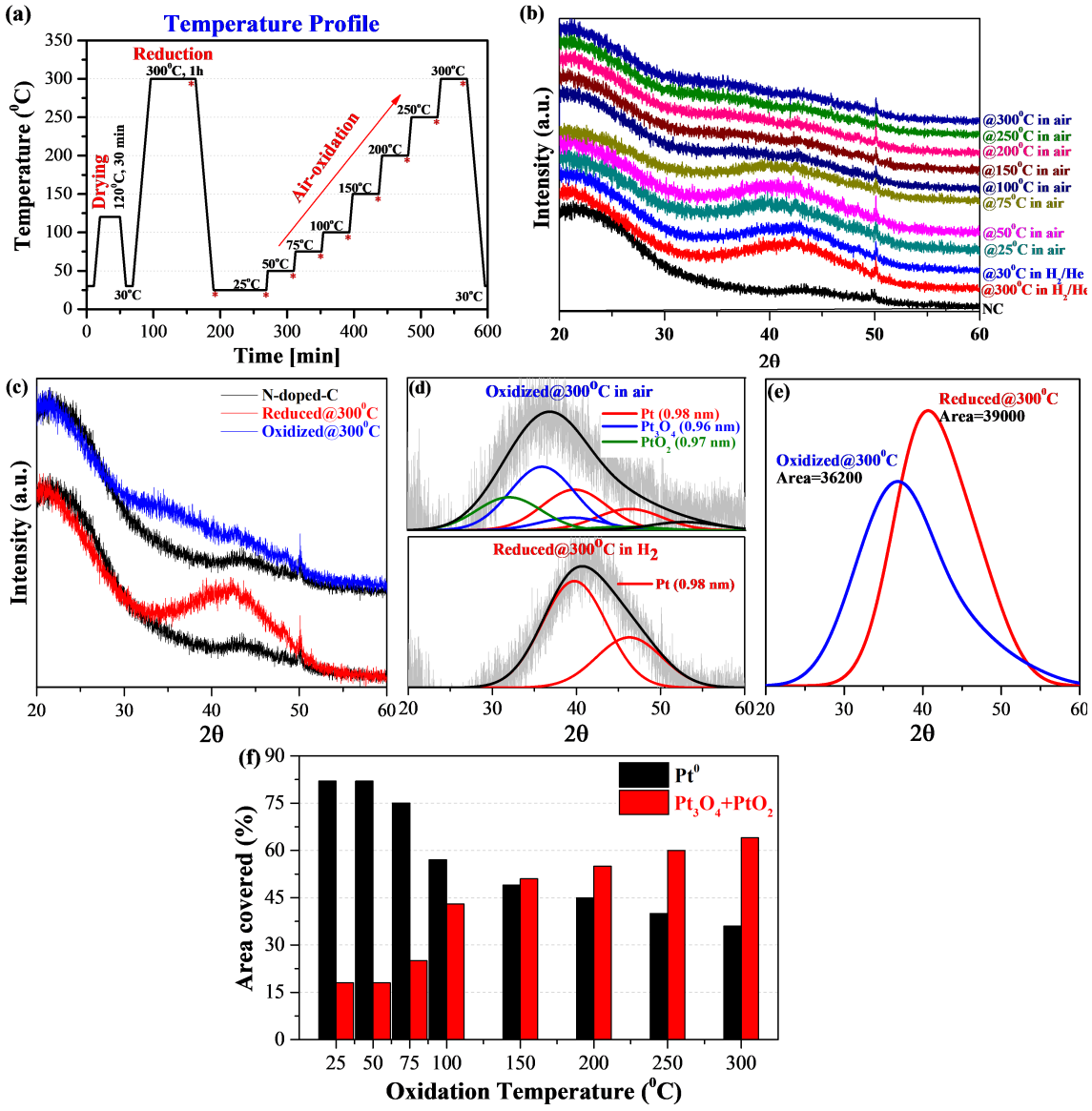

Figure 3.2 In-situ oxidation study of 12.5%Pt/NC catalyst: (a) temperature profile for the oxidation experiment, (b) XRD patterns at different environments and temperatures, (c-e) isolation and fitting of XRD patterns, (f) amount of oxide formation as a function of temperature.

phases in the fully oxidized sample. Analogous sets of snapshots in Figure 3.3 (full set in Figure B.6-B.8)are shown for the other carbon support, described below. The oxidation behavior of Pt/NC is summarized in Figure 3.2f, in which the area fractions of metal and oxide are plotted versus temperature. Extensive oxidation starts at 75 °C, and at 300 °C, about 62% of the metallic Pt is oxidized. This data is remarkably similar to the extent of oxidation of a single-atom catalyst [212]. As others have suggested [213–215], the N dopant appears to exert an influence beyond metal ions or atoms to Pt NPs.

The 18.9%Pt/C (N-free) sample was subjected to the same in-situ oxidation protocol. To better understand the effect of metal loading and Pt particle size, two lower loadings were studied. One was at roughly the same weight loading of Pt in the Pt/NC, 12.1 wt%, but corresponds to a lower surface density of 0.51 μmol/m^2, and the lowest loading, 6.5 wt%Pt/C, corresponds to 0.26 μmol/m^2 (see Table 3.1 for a summary). The XRD data for the oxidation study of this series is shown in Figure 3.4a-c. For each weight loading, the patterns are arranged in the same order as before: support on the bottom followed by the reduced samples at 300 °C and room temperature, and then the oxidized samples at the successively higher temperature. As expected, the higher the Pt loading, the more intense the XRD pattern. The peaks broaden and shift to the left as the particles oxidize in all cases. For an overall comparison, fits of the fully reduced patterns are compared to those of the fully oxidized patterns in Figure 3.4d. The peaks for the fully reduced samples sharpen with loading, indicating an increase in particle size, and these peaks diminish and shift left in the oxidized samples to the same extent.

The extent of Pt oxidation by temperature is summarized in the bar chart of Figure 3.4e. In contrast to the Pt/NC sample, the three Pt/C materials are majority oxides at ambient temperature and reach about 85% oxide at 300 °C. For clarity, this data can be recast as oxide ratios to metallic Pt versus temperature as shown

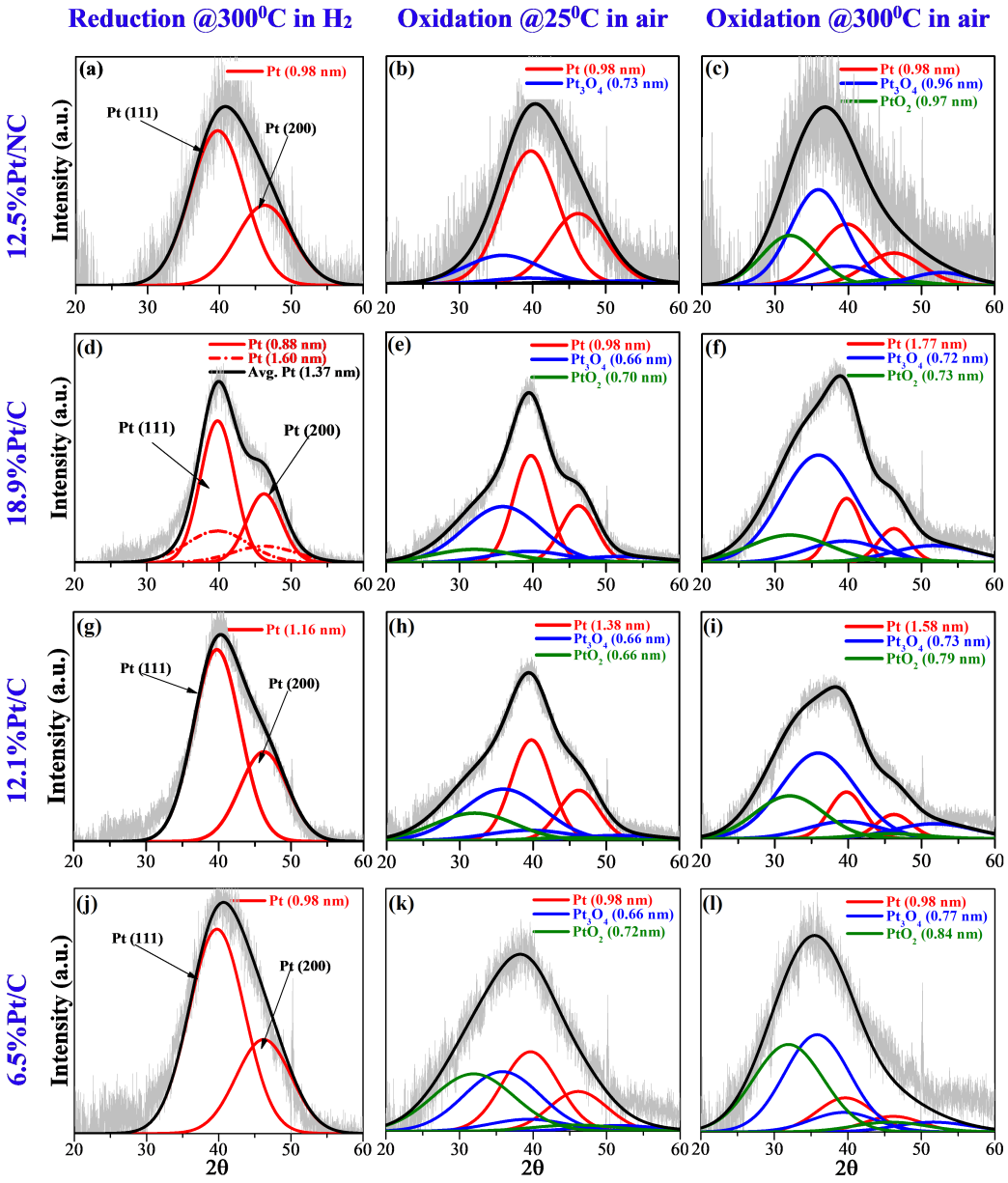

Figure 3.3 Snapshots of the oxidation of Pt/NC and Pt/C materials, a-c) 12.5%Pt/NC, d-f) 18.9%Pt/C, g-i) 12.2%Pt/C, j-l) 6.5%Pt/C.

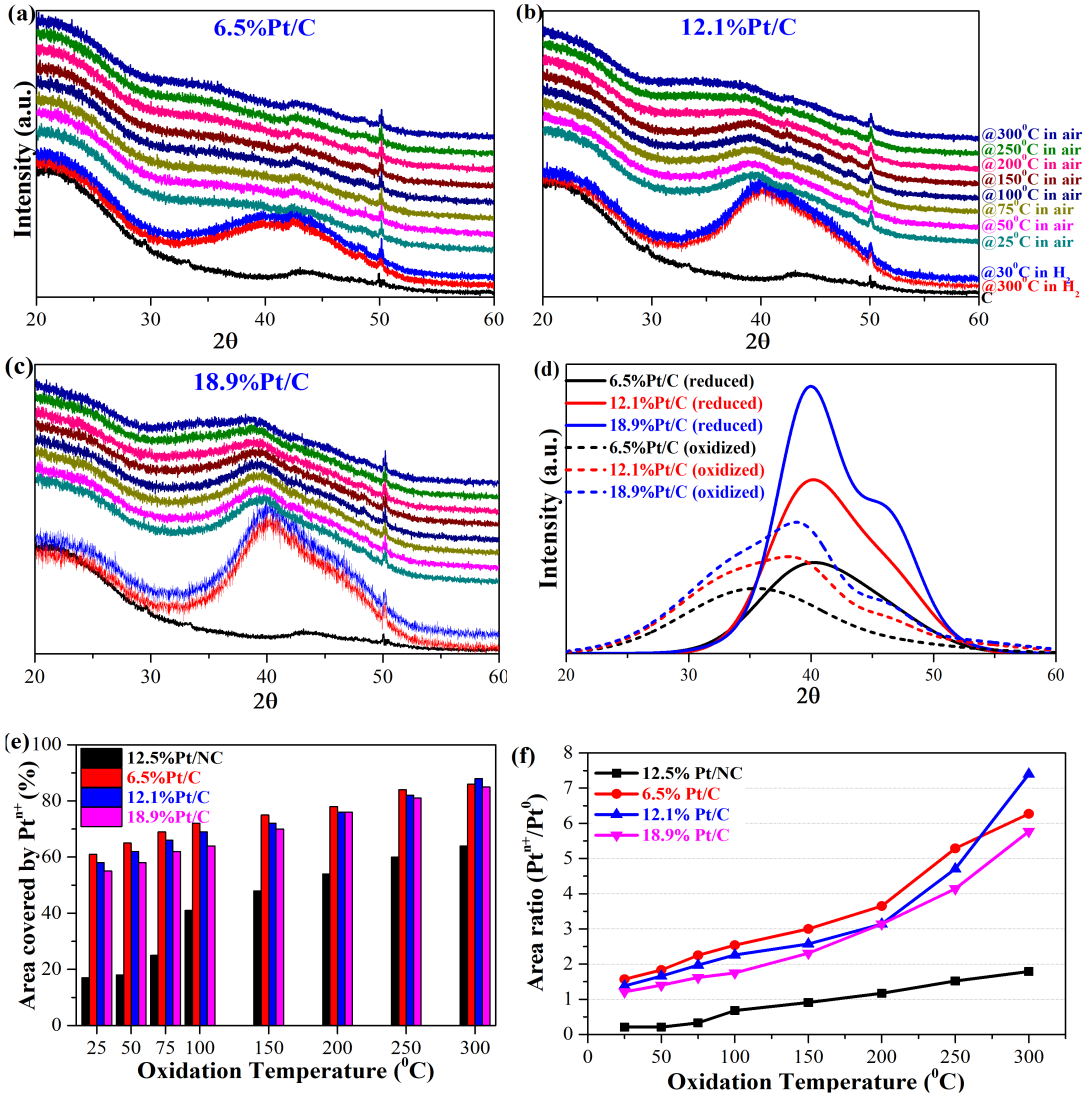

Figure 3.4 In-situ XRD oxidation study of Pt/C materials: (a) 6.5 wt%, (b), 12.1 wt%, (c) 18.9 wt%, (d) overall comparison of fits of fully reduced and oxidized samples of each weight loading, (e) summary of oxide formation as a function of temperature for all samples, including Pt/NC, (f) area ratio of oxide to metallic Pt for all nanoparticle series.

in Figure 3.4f (and in more detail in Figure B.9). The low-temperature oxidative stability of the Pt/NC material is pronounced in this plot. This will likely affect Pt reactivity at low-temperature reactions conditions such as PEM fuel cells, which usually operate at 80 °C [55, 216–218].

High sensitivity XRD has demonstrated the ubiquity of Pt oxides in small, air-

exposed NPs, which suggests this to be the sole reason for the observation of higher Pt valences in previous XPS data of Pt/NC catalysts [203, 204], in contradiction to the speculation that the cause is strong Pt-N bonding [202, 205]. To explore the effects of Pt-N bonding on Pt valence, both Pt/NC and Pt/C materials were investigated with XPS experiments with in-situ reduction and oxidation treatments (details in Appendix-B and Experimental).

A complete set of XPS data for the Pt-free NC and C supports is given in Figure B.16; these show that the C 1s and N 1s of the NC and the C 1s of the C support are relatively unchanged by reduction at 300 °C, oxidation at 25 °C, and oxidation at 300 °C. The N 1s spectra for the NC support can be fit with the same species at precisely the same binding energies (oxidized N, 404.0 eV, graphitic N, 401.8 eV, pyrrolic N, 400.7 eV, amino, 399.6 eV, and pyridinic N, 398.2 eV) as reported by Melke et al. [202]. A full set of C 1s, N 1s, and Pt 4f spectra for the 12.5% Pt/NC sample is shown in Figure B.17, and like the metal-free NC material (FigureB.16), the C 1s and N 1s spectra show minor sensitivity to the reductive and oxidative pretreatments. The most significant difference between the Pt-containing and Pt-free samples is shown in Figure 3.5a (Pt-free N 1s spectrum) and Figure 3.5b (Pt-containing N 1s spectrum). Just as reported in Melke et al. [202], the amino peak in the Pt-free sample was replaced by a new peak at 399.0 eV in the spectrum of the Pt-containing sample, which can be attributed to Pt-N interactions. In contrast to the Melke et al. study, which did not employ in-situ treatment for XPS, the Pt 4f spectrum of the reduced sample (Figure 3.5d) exhibits a single valence with a binding energy of 71.5 eV. This is 0.3 eV above the Pt 4f binding energy of the reduced, N-free Pt/C material shown in Figure 3.5c at 71.2 eV, the value of which is commonly cited in the literature [62]. Several other studies have reported an upward shift of Pt^0 of 0.2 – 0.3 eV over N-doped carbon [205, 206]. As expected, Pt oxidizes over both N-doped and N-free supports at 25 °C and to a higher degree at 300 °C as shown in Figures B.17 and B.18

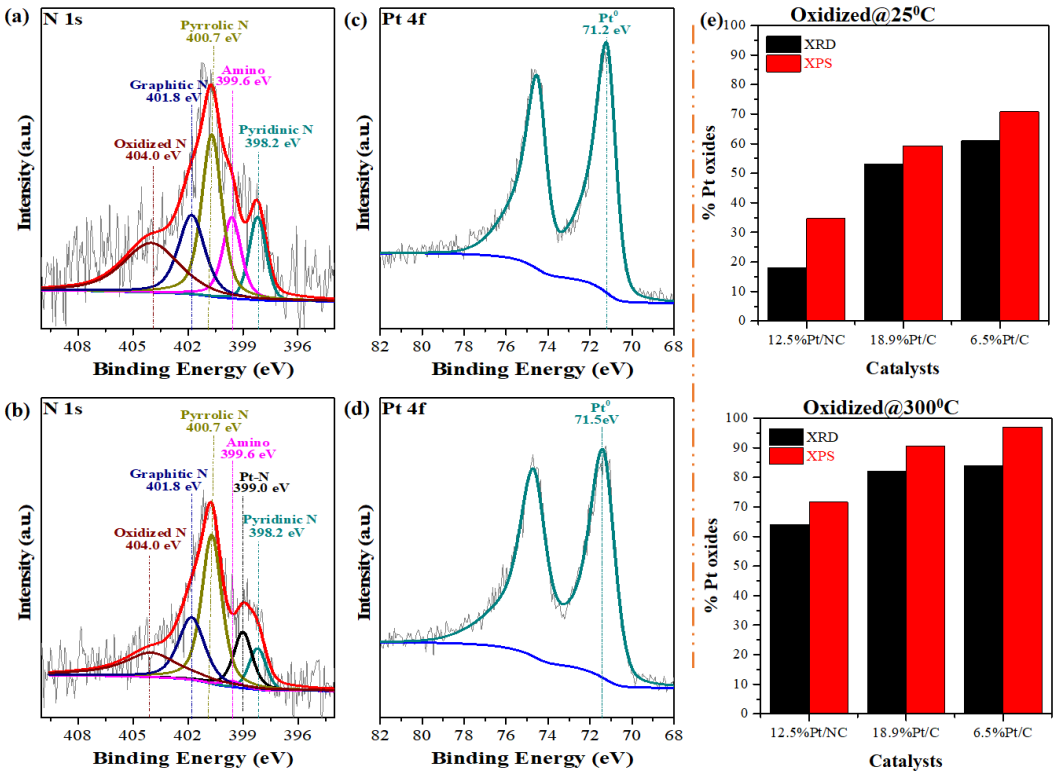

Figure 3.5 XPS spectra of N 1s for (a) N-doped carbon and (b) 12.5%Pt/NC; Pt 4f spectra for (c) 18.9%Pt/C and (d) 12.5%Pt/NC; and (e) the comparison between XRD and XPS on fraction of Pt oxidized at 25 °C and 300 °C.

(and for the 6.5wt% Pt/C sample in Figure B.19). Instead, the Pt-N peak in the N 1s spectra is virtually unchanged by the treatments (Figure B.17); it is independent of the Pt valence.

It can thus be concluded that higher Pt valence observed by XPS is not indicative of Pt-N bonds. The higher Pt valence must therefore arise from Pt-O bonds in nanoparticulate Pt oxides. Several XPS studies have alluded to the oxidation of Pt as the cause of the higher valences [202, 205, 206] but have not had the means to confirm this independently. In this work, high sensitivity XRD provides this confirmation. Furthermore, while Pt-N interactions do not give rise to higher Pt valences, the small but significant (0.2 – 0.3 eV) shift in the Pt^0 electron binding energy to about 71.5 eV

(Figure 3.5d and Figure 3.5b) appear to be the proper fingerprint of electron transfer from the Pt to the N-doped support via the Pt-N interactions [204]. The higher Pt^0 binding energy over N-doped C persists even as the majority of Pt is oxidized (Figure B.17). The fraction of Pt oxidized as estimated from the XPS results (from Figure B.16-B.19) is compared to estimates from XRD (from Figures 3.3 and 3.4) in Figure 3.5e for the 12.5%Pt/NC, 18.9%Pt/C and 6.5%Pt/C catalysts. Trends of XPS follow the XRD trends for all materials at both oxidation temperatures, with the XPS results always being slightly higher given its greater surface sensitivity. The XRD analysis concluded that the N-doped carbon significantly stabilizes the Pt NPs to oxidation, also confirmed with the XPS analysis.

The experimental XPS results in this study are also in excellent agreement with the recent DFT analysis by Ma et al. [204] N atoms (inside the graphene support) on metal-support and metal-O_2 interactions. The DFT calculation revealed that the metal-support interaction energy (binding strength) significantly increases when N atoms are doped into the graphene (G) structure (interaction energy for Pt_4-G, Pt_4-G-1N, and Pt_4-G-3N are -1.15, -2.74, and -2.43 eV, respectively; Pt_4 represents a cluster with four Pt atoms). However, the binding strength of Pt_4-O_2 was higher for Pt/NC samples than Pt/C, indicating easier O_2 dissociation on Pt-NC samples and less resistive to oxidation. Conversely, the investigation based on a cluster of 38 Pt atoms (Pt_{38}), a model system closer to the 1 nm (Approx.) Pt NPs of this study, showed that the Pt_{38}-O_2 bond is weaker for the Pt/NC samples than Pt/C, implying quicker oxidation of Pt NPs supported on N-free graphene. Furthermore, the separation of the Pt cluster from the support was more dominant when O_2 was adsorbed close to the Pt-C interface compared to the adsorption close to the Pt-NC interface, indicating higher stability of Pt-NC bonds than Pt-C bonds. To summarize DFT results predicted that small Pt NPs bonded to NC supports will be more resistant to oxidation and agglomeration than Pt NPs bonded to C.

A second set of XRD experiments, the protocol of which is shown in Figure 3.6a, was conducted to compare the resistance of the NC- versus the C-supported Pt NPs to thermal sintering. In this case, after an initial reduction, the samples were heated in He through 900 °C with XRD patterns recorded at various increments (details in Appendix-B). The Pt/NC material was compared to the two higher Pt/C loadings. In addition, control samples were prepared by dry impregnation (DI), which does not involve Pt precursor – carbon interactions and results in larger particle sizes [219], were included.

The diffraction patterns for the SEA and DI-derived NC supported NPs are shown in Figure 3.6c and 3.6d, those for the 18.9%Pt/C SEA and DI samples in Figure 3.6e and 3.6f, and those of the 12.1%Pt/C material in Figure 3.6g and 3.6h. The DI patterns (right side of the figure) all contain additional peaks for NaCl from the ions remaining in the sample as DI does not involve a filtration step to remove counterions. Additionally, the Pt (111) and (200) peaks for all samples exhibit bimodality; a sharper peak emerges from a broader peak at the same 2θ value. Sharpening of the peaks, indicative of Pt NP sintering, occurs as the temperature increases. The detailed fits of each pattern are given in Figure B.10-B.15. The peaks of the corresponding SEA-prepared samples on the left side of the figure are notably broader than those of the DI samples. As noted previously, with approximately the same surface density (0.81 and 0.87 μmol/m^2) the peaks of the 12.5%Pt/NC SEA sample (Figure 3.6c) are notably broader than those of the 18.9%Pt/C SEA sample (Figure 3.6e). The peaks of all SEA samples also sharpen as the temperature is increased. Detailed fits of each SEA sample are given in Figure B.10-B.15.

From the FWHM of these fits, average particle sizes were calculated at each sample at each temperature, and the results are summarized in Figure 3.6b. The three lower curves represent the SEA-derived samples; Pt/NC particle size starts at 0.98 nm and increases to 1.4 nm at 900 °C, the 12.1%Pt/C size increases from 1.2 to 1.8 nm, and

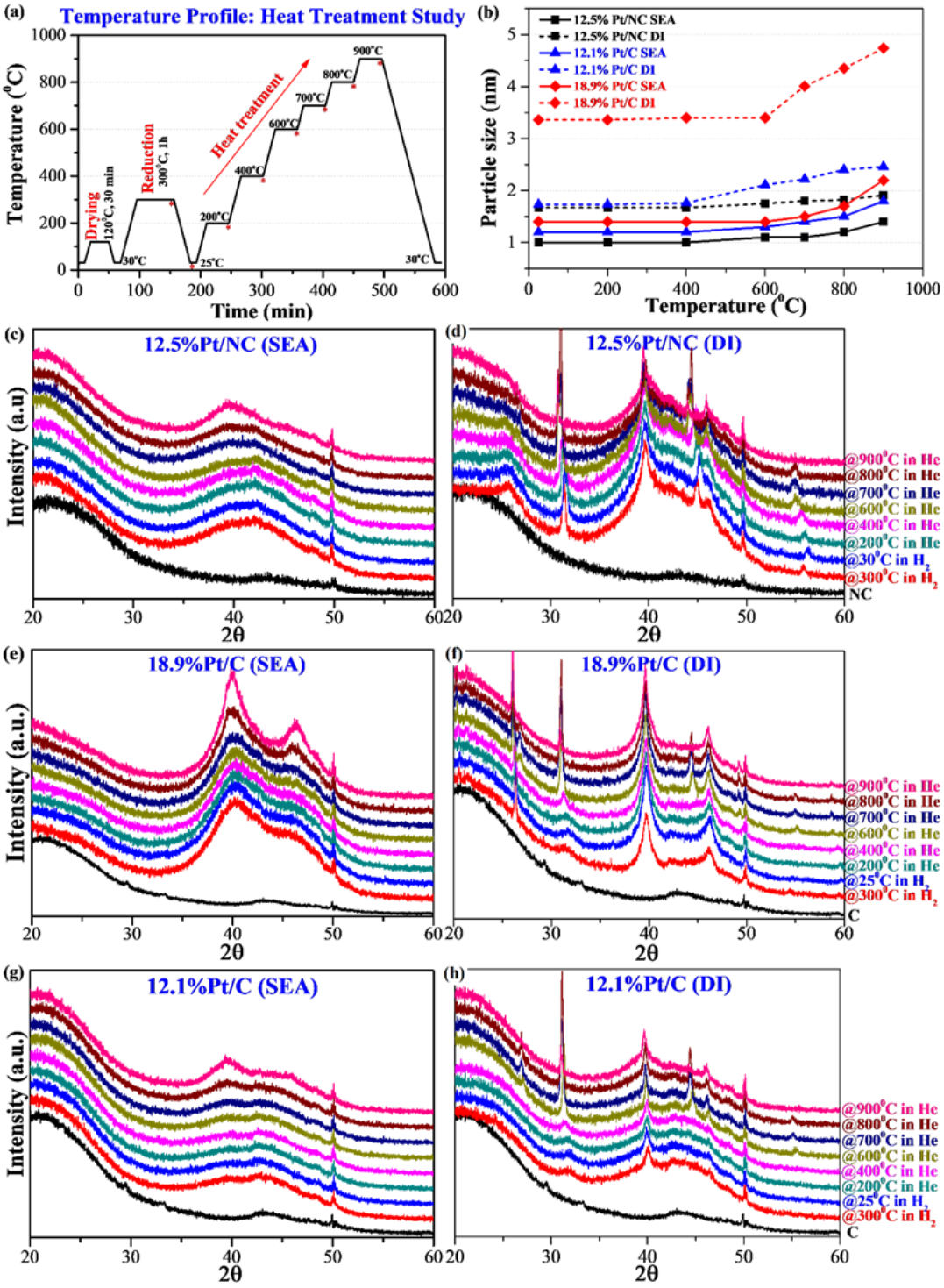

Figure 3.6 XRD sintering study (a) the temperature profile (b) of results (c-h) XRD patterns for the heat-treated Pt/C and Pt/NC materials prepared by both strong electrostatic adsorption (SEA) and dry impregnation (DI).

the 18.9%Pt/C increases from 1.4 to 2.1 nm. Of this set of SEA-derived samples, the two C-supported NPs series increase in size by about 50%. Since particle diameter is inversely proportional to dispersion, they lose about 50% of their active surface area. The NC-supported NPs sinter about 40% and lose 40% of their active area. Perhaps the most notable NC-supported a DI-derived sample, shown as the lowest of the top three dashed curves representing the DI samples.

This sample sinters from an initial size of 1.7 nm to a final size of 1.9 nm, losing only 12% of its active area, while the two C-supported samples sinter from 1.7 to 2.5 nm (lower loading) and from 3.4 to 4.7 nm (high loading). While the DI-prepared sample did not start from the beneficial condition of strong electrostatic interactions of the anionic Pt precursor with the positively charged carbon surface, it appears that the N dopant provides a strong interaction with the formed Pt NPs.

3.5 Conclusions

In summary, Pt NPs supported on a nitrogen-doped carbon support derived from poly-phenylporphyrin have shown increased stability to oxidation and thermal sintering. The enhanced Pt-support interaction arising from the N dopant versus the N-free carbon is manifested by (1) decreased initial Pt particle sizes, (2) smaller particle size at higher surface densities, 3) increased resistance of Pt NPs to oxidation, (4) increased electron binding energy of Pt^0, and (5) increased resistance of Pt NPs to sintering. It is expected that the higher stability of Pt on NC will be manifested in greater long-term performance in applications such as fuel cells and catalytic reactions.

Chapter 4

Strong electrostatic adsorption: An effective technique to synthesize durable Pt/XC72R catalyst for PEM fuel cells

4.1 Abstract

Platinum nanoparticles (Pt NPs) supported on carbon (Pt/C) are active catalysts for the oxygen reduction reaction (ORR) in proton-exchange membrane fuel cells (PEMFCs). However, the inadequate durability of Pt/C catalyst under ORR conditions is preventing the commercialization of PEMFCs. The sintering of Pt NPs due to poor metal-support interactions (MSI) contributes to this poor durability. This work effectively tunes MSI by controlled synthesis of Pt NPs supported on Vulcan XC72R (denoted as C). The MSI was explored through membrane electrode assembly (MEA) durability testing in PEMFCs and thermal stability testing of Pt NPs under 6%H2/Ar at 750 ^{o}C (12 h). Four different synthesis methods, including polyol, incipient wet impregnation (IWI), wet impregnation (WI), and strong electrostatic adsorption (SEA), were investigated to identify the effects of the deposition procedure on MSI. The highest MSI was attained with SEA catalyst, which provides (1) the lowest MEA degradation after 30,000 accelerated stress test (AST) cycles and (2) the least sintering of Pt NPs after high-temperature annealing. In addition, x-ray diffraction (XRD), transmission electron microscopy (TEM), and X-ray photoelectron spectroscopy experiments were performed to understand MSI in Pt/C catalysts.

4.2 Introduction

PEMFC is a promising clean energy technology capable of reducing the usage of fossil fuels, especially in the transport sector, because of its excellent energy conversion efficiency, high energy density, rapid fueling, and environment-friendly emissions. Pt NPs supported on carbon (Pt/C) are the most active catalyst for PEMFCs, and dispersed NPs with narrow size distribution are preferable since this increases the number of active catalyst sites [220]. However, the durability of Pt/C catalyst under ORR conditions in PEMFCs is still a challenge, hindering extensive commercialization

of PEMFCs [221]. The catalyst degradation is predominantly caused by Pt particle growth during ORR at the cathode [222–225]. The literature often reports two key mechanisms to explain Pt sintering in PEMFCs: Oswald ripening and particle coalescence. In Oswald ripening, smaller Pt NPs dissolve and redeposit on larger NPs, resulting in net growth of NP size in the catalyst layer [70, 226, 227]. Conversely, particle coalescence occurs primarily because of poor Pt-C adhesion and because of carbon corrosion at ORR conditions – Pt NPs are detached from the carbon support and attached with other particles, leading to the agglomeration of Pt NPs [228]. Particle growth in PEMFCs significantly lowers the electrochemical surface area (ECSA) and utilization efficiency of Pt, causing a substantial decrease in the catalytic activity [229]. Carbon corrosion denotes the formation of CO2 due to the electrochemical oxidation of carbon in PEMFCs at potential above +0.207 V ($C + 2H_2O \rightarrow CO_2 + 4H^+ + 4e^-$) [230–234]. Typically, Vulcan XC72 carbon corrodes at 65 °C with an applied potential greater than 0.8 V (vs. RHE – reversible hydrogen electrode) [235]. However, in most cases, carbon corrosion at normal fuel cell operation is kinetically sluggish and sometimes negligible [236]. This study synthesizes a list of cathode catalysts using the same support with similar Pt loading (12 wt%) and follows identical experimental procedures to produce similar particle sizes. Therefore, it is assumed that the variation in catalyst durability in this work is caused by weak adhesion of the Pt on the carbon, allowing Pt particles to migrate and then coalesce.

As mentioned above, particle coalescence occurs due to poor MSI and carbon corrosion during PEMFC operation. The specific MSI inherently determines the dissolution of Pt NPs in the MEA; the stronger the interactions, the less the migration of Pt NPs from the MEA catalyst layer [105]. Although carbon graphitization and doping with heteroatoms are prevalent approaches to alleviate catalyst migration in PEMFCs by improving MSI [237–240], carbon modification includes numerous complex steps (e.g., high-temperature pyrolysis) [240–242] that might complicate the

catalyst synthesis processes. Nevertheless, in recent years, significant progress has been observed in the synthesis methodology, enabling tuning of the MSI to improve the catalytic performance of supported metal NPs [31–36]. Impregnation methods, including WI and IWI, are the most common methods to synthesize Pt/C catalysts for PEMFCs. However, these methods usually yield NPs with poor dispersion and broad size distribution owing to induced interactions between the precursor and the support. Also, the pH of the precursor solution is rarely controlled before impregnating into the support, while controlling solution pH is critical to optimize MSI [70]. Polyol methods, also known as 'colloidal methods,' are another common synthesis approach that produces metallic NPs beforehand that are deposited later on the support with controlled size, uniformity, and dispersion in alkaline ethylene glycol (EG) solution; EG functions as a reducing agent [83]. However, the deposition of colloidal NPs into the support surface in EG solution is still a concern; deposition typically occurs through continuous mixing of support and the solution having metal NPs. Furthermore, like impregnation approaches, the polyol method does not control the solution pH, which may cause insufficient interactions between colloidal metal NPs and the support [84].

Conversely, SEA is a comparatively new method employed to synthesize Pt/C catalysts for PEMFCs. SEA is a particular type of WI method where metal precursors are adsorbed onto a charged surface of the support. The support surface is charged by carefully adjusting the solution pH, creating coulombic interactions between the charged surface and the oppositely charged precursor [85]. The optimum SEA pH and the desired precursor are determined based on the pH when the maximum amount of precursor adsorbs and the point of zero charge (PZC, the pH when the net surface charge of the support is zero), respectively. Based on SEA protocol [86, 208, 243], an anionic precursor (i.e., H_2PtCl_6) is typically used for high PZC supports like Vulcan XC72R (PZC = 8.5) [244]. The SEA method enables improved distribution

of precursors across the support. As a result, small, uniform, and dispersed metallic NPs with strong MSI are formed. In addition, the particle size distribution by SEA is significantly narrower than typical impregnation approaches [208, 243, 245–248], resulting in high catalytic activity. For example, Nathalie et al. [249] synthesized 2 nm-sized (mean) Pt NPs by depositing 22.3 wt% of Pt onto a carbon xerogel (BET SA – 643 m^2/g) using successive SEA techniques (successive adsorption – reduction cycles), which was tested later in an H_2/air PEMFC system. The MEA activity for SEA prepared Pt/Xerogel catalyst was about twice that of impregnated Pt/Xerogel catalyst with the same metal weight percent. However, insufficient research has been performed to scrutinize the durability of SEA catalysts for ORR in PEMFCs, demanding a profound investigation of SEA catalyst synthesis and its performance in PEMFCs.

Since ionic interactions occur at the precursor-support interface during SEA synthesis, this work hypothesizes that the SEA method builds stronger MSI, stabilizing Pt NPs and reducing Pt sintering during ORR in PEMFCs and high-temperature annealing treatments. A systematic comparison was made to validate the above hypothesis on a series of Pt/C catalysts prepared by the polyol, WI, and IWI methods. In addition, this work investigated the MEA durability of Pt/C catalysts in ORR environments and the thermal stability of Pt NPs in a high-temperature H2 atmosphere. All the catalysts were characterized by XRD, TEM, and XPS.

Therefore, this study hypothesizes that the SEA technique, which provides strong MSI, can alleviate metal sintering during ORR in PEMFCs and annealing at high temperatures, which will increase catalyst durability and stability, respectively. In this work, four different synthesis methods, including polyol, IWI, WI, and SEA, have been investigated with comparisons of the MEA durability in PEMFCs and the stability of Pt NPs under high-temperature annealing conditions. In addition, the catalysts have been characterized by (1) XRD to observe Pt sintering due to high-

temperature exposure and (2) TEM to detect particle growth during heat treatment and MEA durability testing.

4.3 Experimental

4.3.1 Materials

Vulcan XC72R carbon black (BET SA – 200 m^2/g) obtained from FuelCell Store was used as support. Two Pt precursors: hydrogen hexachloroplatinate (IV) hydrate (HCP, H_2PtCl_6.xH2O, $\geq$ 99.9%, Sigma Aldrich), and Platinum (II) acetylacetonate ($Pt(acac)_2$, 97%, Sigma Aldrich), which are respectively anionic and neutral salts, were used in this study. Sodium hydroxide (NaOH, 5.0 M) and hydrochloric acid (HCl, 37%) from Sigma Aldrich were used to adjust the pH of the precursor solution. A list of chemicals was also used during catalyst synthesis, including deionized water (DI-water, 18.2W, Q-series, Millipore), acetone (ACS Certified, Fisher Scientific), ethylene glycol (EG, ACS Certified, Fisher Scientific), n-propanol (NPA, $\geq$ 99.5%, Sigma Aldrich), and isopropanol (IPA, 99.5%, Sigma Aldrich). Materials used in this study also comprise ultra-high purity nitrogen (N_2) and forming gas (6%H_2 balance Ar) from Airgas, Nafion ionomer solution (D2020), and Nafion membrane (NR211) from Ion Power, and gas diffusion layer (GDL, Sigracet 22BB) from SGL Carbon. In addition, a commercial Pt/C catalyst (TEC10V20E, 20 wt% Pt on Vulcan carbon, TKK) was used as the anode. All materials were used as received without further purification.

4.3.2 Preparation of Pt/C catalyst

A stock solution of Pt precursor (0.1 M, non-hydrous basis) was prepared by dissolving 2.045 g of HCP salt in 50 mL of DI-water, used in polyol, WI, and IWI methods. The stock solution was sealed in an aluminum foil-wrapped vial and stored

in a dark place to avoid photoreaction.

Polyol Synthesis (Colloidal method)

Polyol synthesis comprises suspending the metal precursor in the glycol solvent and subsequently heating the solution at refluxing temperature, yielding metal nanoparticle synthesis in the solution phase with controlled size and shape [250]. This study includes two different pathways of polyol synthesis: 1-step (Polyol-1) and 2-step (Polyol-2) synthesis techniques. In Polyol-1, Pt precursor is simultaneously transformed into Pt NPs and deposited on carbon. Conversely, in Polyol-2, the precursor was transformed into Pt NPs beforehand, and later Pt NPs were deposited into the carbon using the wet impregnation technique [251]. Both polyol synthesis methods are shown in Figure 4.1.

In Polyol-1, 200 mg of XC72R was mixed with 200 mL of EG and 100 mL of DI-water in a 500 mL three-neck flask. First, the mixture was sonicated for an hour to attain a homogeneous solution. Later, 1.8 mL of HCP stock solution (0.1 M) was added to the dispersed carbon solution and stirred for 24 h at room temperature. Finally, the Pt precursor was reduced under reflux conditions (108 ^{o}C, 2 h, N_2 atmosphere). A thermocouple associated with a programmable temperature controller was inserted into the solution to control heating rate, reflux temperature, and temperature holding time. In Polyol-2, 1.8 mL of HPA stock solution (0.1 M) was first added to 200 mL of EG solution in a 500 mL three-neck flask and mixed for two days using a magnetic stirrer. After that, the mixture was heated under reflux conditions (108 ^{o}C, 2 h, N_2 atmosphere) to transform Pt precursor into Pt NPs. Meanwhile, 200 mg of XC72R was mixed with 200 mL H_2O/NPA solution (H_2O: NPA = 4:3; volume basis), followed by bath sonication for 2 h. Next, the suspension was added into the Pt NPs solution and mixed for 24 h before vacuum filtration.

In both cases, the resulting catalyst was separated by vacuum filtration and

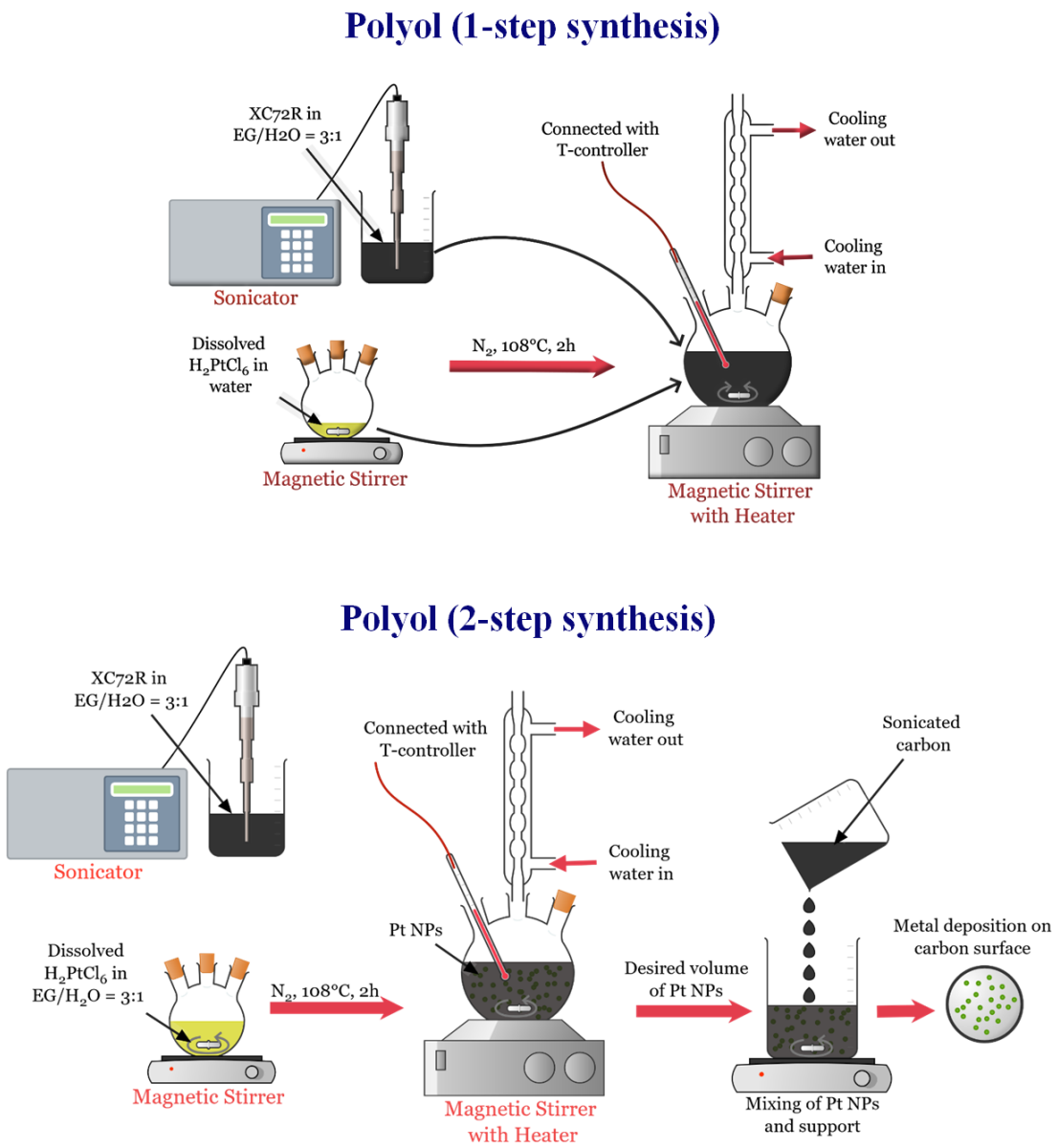

Figure 4.1 Experimental schematic of Polyol-1 and Polyol-2 synthesis methods.

washed with 3 L of DI-water for 200 mg of catalyst to remove all chloride residues. The sample was dried in a vacuum oven at 80 oC overnight, then annealed at 400 °C for 2 h in a fluidized bed reactor under an N_2 environment (200 SCCM) to remove residual EG. TGA measurements quantified the final Pt loadings; 12.4 wt% and 12.2 wt% Pt were deposited with Polyol-1 and Polyol-2 methods, respectively.

Wet impregnation (WI)

WI refers to the deposition of a metal precursor into the support with an excess volume of impregnating precursor solution than the pore volume of the support material. The desired amount of a metal precursor solution is mixed with the support, subsequently dried, and reduced to transfer metal precursor to metal NPs [252]. In this study, using DI-water, 1.8 mL of stock solution (0.1 M) was first diluted to 100 mL. Afterward, 200 mg of XC72R carbon black (pore volume 4.6 mL/g) was added to the diluted precursor solution. The mixture was sonicated with a tip sonicator for 3 min, followed by bath sonication for an hour. Finally, the slurry was magnetically stirred in a hot plate at 70 °C until complete evaporation of the solvent. The residual sample after the evaporation was first dried in a vacuum oven at 80 °C overnight, then dried at 120 °C for 2 h in a fluidized bed reactor under an N^2 environment (200 SCCM). Finally, the dried sample was reduced under forming gas (200 SCCM) at 250 °C for an hour. The Pt loading on XC72R was found to be 12.8 wt% using TGA measurement.

The impregnation of precursor solution with the same volume as the support pore is known as IWI [252]. This work used two different Pt precursors, HCP and $Pt(acac)_2$ (denoted as PA), to synthesize Pt/C catalysts with the IWI method. The synthesis method of Pt/C catalysts using PA and HCP precursors is denoted as IWI-PA and IWI, respectively. The precursor was dissolved in solvent: (1) 70 mg of the PA pre-

cursor in 1 mL of acetone and (2) 80 mg of HCP precursor in 1 mL of DI-water before mixing with 200 mg of XC72R. Like WI, the mixed slurry was magnetically stirred in a hot plate at 70 oC until the complete evaporation of the solvent. The drying and reduction steps for IWI were identical to the WI method. TGA confirmed 12.2 and 12.1 wt% of Pt deposition on carbon using PA and HCP precursor, respectively.

Strong-electrostatic adsorption (SEA)

A 120 mL solution of Pt precursor with a nominal concentration of 300 ppm was prepared by dissolving HCP salt in DI-water. The pH of the solution was adjusted to 3.0 using NaOH and HCl solutions, as the optimum uptake of HCP on XC72 was obtained at pH = 3.0 [253]. The solution was aged for 12 h before starting SEA. Meanwhile, 200 mg of XC72R was mixed with 40 mL of water solution at pH=3.0. This mixture was sonicated in tip sonicator for 3 min, followed by bath sonication for an hour. When carbon was entirely dispersed, the 70 mL of precursor solution (pH = 3.0) was added to the dispersed carbon with a 500 m^2/L surface loading of XC72R. Afterward, the mixture was magnetically stirred for an hour at 400 rpm speed. The mixed slurry was subsequently filtered using the vacuum filtration technique and dried in a vacuum oven at 80 °C overnight, then dried at 120 °C for 2 h in a fluidized bed reactor under an N_2 environment (200 SCCM). Finally, the dried sample was reduced under forming gas (200 SCCM) at 250 °C for an hour. The Pt loading on XC72R was about 7.2 wt% after the first SEA cycle, measured by TGA. Therefore, another cycle of SEA on 7.2% Pt/C catalyst was performed using the remaining 50 mL of precursor solution to obtain desired Pt loading. After the second SEA cycle, the TGA result showed that the final Pt loading was approximately 11.6 wt%.

4.3.3 Characterization of Pt/C catalyst

A TGA Q50 (TA Instruments, USA) instrument was used to determine the de-

posited weight percentage of Pt on XC72R utilizing the thermogravimetric analysis technique. About 5.0 mg of Pt/C catalyst was heated under air (10 sccm – balance gas and 90 sccm – purge gas) from room temperature to 800 °C with a heating rate of 5 °C/min followed by a 30 min hold at 800 °C. The crystal structure of Pt was investigated by a Bruker D5000 powder XRD instrument (Siemens, USA), which is equipped with a monochromatic Cu-Kα radiation source (λ = 1.54184 Å) and operated at 35 mA and 40 kV. The XRD data were obtained from 20 to 80° 2θ with a scanning rate of 0.5° 2θ/min and a sample width of 0.02. In addition, bright-field TEM characterization was carried out on an FEI Technai F30 (Thermo Fisher Scientific, USA) electron microscope, operated at an accelerating voltage of 200 keV, to determine the average size and size distribution of Pt NPs. The TEM images were recorded using the DigitalMicrograph software, and particle size distributions were obtained based on approximately 1000 Pt NPs (manually counted using Particulate2 software) on each catalyst. The number (DN), area (DS), and volume (DV) average sizes of Pt NPs were determined using the equations below:

$$D_{\mathrm{N}} = \frac{\sum n_{\mathrm{i}} {d_{\mathrm{i}}}^2}{\sum n_{\mathrm{i}} d_{\mathrm{i}}} \tag{4.1}$$

$$D_{\mathrm{S}} = \frac{\sum n_{\mathrm{i}} {d_{\mathrm{i}}}^3}{\sum n_{\mathrm{i}} {d_{\mathrm{i}}}^2} \tag{4.2}$$

$$D_{\mathrm{V}} = \frac{\sum n_{\mathrm{i}} {d_{\mathrm{i}}}^4}{\sum n_{\mathrm{i}} {d_{\mathrm{i}}}^3} \tag{4.3}$$

Where n_i and d_i respectively denote the number of particles and diameter of each particle. These equations assume the particles are either hemispherical or spherical [244].

A QUANT'X XRF spectrometer (Thermo Scientific, USA) equipped with an aluminum filter, an accelerating voltage of 25 kV, a tube current of 1.98 mA, and a scan duration of 1 minute was used to determine Pt concentration (mg/cm^2) in MEAs.

The metal-support interactions for fresh (as-prepared) catalysts were characterized by XPS experiments in a Kratos Ultra DLD XPS system (Kratos Analytical, USA). The XPS instrument is equipped with a monochromatic Al-Kα source operated at 1486.6 eV and 150 W, a hemispherical analyzer, a charge neutralizer, and a load lock chamber that enables the rapid introduction of samples without breaking the vacuum. An electron beam was directed on the sample in XPS measurements to neutralize the charge. XPS spectra analysis was conducted at an approximate pressure of 2×10^{-9} mbar, and charge compensation was accomplished using low-energy electrons. All spectra were charged referenced by adjusting the C 1s region to 284.6. High-resolution C 1s and Pt 4f spectra were acquired at a pass energy of 20 eV. The obtained XPS spectrums were fitted in Casa XPS software using the combination of Gaussian and Lorentzian functions with the subtraction of Shirley-type background.

4.3.4 Catalyst ink preparation and MEA fabrication

MEAs with an active area of 5.0 cm^2 were fabricated by directly spraying catalyst ink onto the Nafion NR211 membrane using a program-controlled ultrasonic spray coater (Sono-Tek, USA). Cathode catalyst was sprayed first to obtain the desired Pt loading of about 0.1 mg/cm^2, verified by XRF measurements. The Pt loading in the anode was also set to be 0.1 mg/cm^2. The ink was prepared by mixing the catalyst with Nafion D2020 ionomer and H_2O/NPA solution (H_2O: NPA = 4:3; volume basis). The amount of D2020 was selected to achieve an ionomer to carbon ratio (I/C) of 0.5. An arbitrary number (428) was multiplied with the amount of carbon in the catalyst to obtain the required amount of H_2O/NPA solution. The recipes to prepare ink using different cathode catalysts are summarized in Table 4.1. In ink preparation, the mixture was magnetically stirred for 10-15 minutes, followed by ultra-sonication for about 30 minutes in an ice bath to get a homogeneous ink dispersion. Before spraying ink, the membrane was immobilized on a heated vacuum plate at 95-98 ^oC, which

Table 4.1 Recipe for cathode Ink Preparation.

Method	Pt deposition [wt%]	Catalyst [mg]	D2020 [g]	I/C ratio	4:3 H_2O/NPA [g]
Polyol-1	12.4	41.5	0.0861	0.521	15.07
Polyol-2	12.2	40.8	0.0865	0.502	15.56
IWI	12.1	66.0	0.1352	0.505	24.86
IW	12.8	41.7	0.0872	0.528	15.06
SEA	11.6	25.4	0.0555	0.537	9.66
IWI-PA	12.2	25.3	0.0523	0.511	9.61

helped rapidly dry the coated surface, preventing ink flooding on the membrane. The cell was assembled by sandwiching the prepared MEA between two 22BB GDLs. A pair of polyurethane gasket sheets were used to seal the edges of the MEA, averting gas leakage during fuel cell operations. An 80 lb_f.inch torque was gradually applied to eight bolts to tighten the hardware through two insulated endplates.

4.3.5 Fuel cell testing

The single fuel cell performance of the cathode catalysts was tested at an 850e Fuel Cell Test Station (Scribner, USA). A standard break-in protocol was repetitively run until a plateau current was reached at 0.6 V in 150 kPa absolute pressure (kP_{abs}) H_2/Air (80 °C, 100% relative humidity (RH), 1000/3000 SCCM). The break-in protocol subsequently measured hydrogen underpotential deposition (HUPD) ECSA, H_2 Crossover, MA, and H_2/Air polarization curve (pol-curve). Cyclic voltammetry (CV) with seven repetitive cycles of forward-scanning from 0.08 V to 0.98 V and reverse scanning from 0.98 V to 0.08 V at a rate of 50 mV/s to measure HUPD-ECSA with the cell and humidifier temperatures set to 30 and 80 °C, respectively. The H_2 crossover was estimated by measuring current at 0.5 V in H_2/N_2 (150 kPa_{abs}, 80 °C, 100% RH, 1000/1000 SCCM), while MA was measured at 0.9 V (iR-free) under H_2/O_2 (150 kPa_{abs}, 80 °C, 100% RH, 1000/3000 SCCM). The cell potential was held at 0.9 V

(iR-free) for 15 min in MA measurement, followed by a minute held for OCV and HFR measurement. This study estimated the MA based on the last-minute current average at 0.9 V (iR-free) with correction for measured H_2 crossover. Next, the polarization curve at cell potential between 0.4 V and 0.91 V was measured in H_2/Air (150 kPa_{abs}, 80 oC, 100% RH, 1000/3000 SCCM). First, the cell potential was raised from 0.4 V to 0.8 V with a step size of 0.05 V, followed by 0.025 V steps up to 0.9 V; then measured current at 0.91 V and OCV. The applied potential was held for four minutes at each step.

An additional ECSA measurement was conducted after the break-in using carbon monoxide (CO) stripping at four different RHs (30%, 50%, 75%, and 100%) with three CV cycles (seven cycles were used in HUPD-ECSA measurement). First, 1000 ppm CO in N_2 was applied to the cathode to form an adsorbed CO monolayer, followed by N_2 purging to remove gas-phase CO from the system(150 kPa_{abs}, cell temperature-30 ^oC, humidified temperature-80 ^oC, 500/1000 SCCM) with two subsequent oxidations under 5% H_2 (balance N_2)/N_2 to remove adsorbed CO from the cathode surface oxidatively. The CO-ECSA was estimated by utilizing the CO oxidation charge. When the CO-ECSA measurement was done, the cathode layer was recovered through three recovery cycles using the same procedure as the break-in. The HUPD-ECSA, MA, and polarization curves reported in this study were measured by analyzing recovery cycle data.

The AST experiment was performed using the trapezoidal wave method at cell voltage between 0.6 and 0.95 V with 2.5 s hold time and 0.5 s rise time under H_2/N_2 (150 kPaabs¬, 80 oC, 100%RH, 200/200 SCCM) for 30,000 cycles.

4.4 Results and Discussions

This study investigated six different Pt/C catalysts prepared by the polyol, IWI, WI, and SEA methods. XRD was used to characterize the crystal lattice of Pt/C

Table 4.2 XRD particle size estimates of Pt and Pt_3O_4 of fresh and annealed catalysts

Catalyst	Fresh [nm]		Annealed [nm]
	Pt	Pt_3O_4	Pt
Polyol-1	2.3	0.9	6.7
Polyol-2	3.0	-	7.2
IWI	2.4	1.0	5.8
IW	2.7	0.9	5.3
SEA	2.4	0.9	3.5
IWI-PA	2.6	1.0	6.3

catalysts to determine the thermal stability of Pt NPs after standard annealing treatment (6% H2/Ar at 750 °C for 12 h). The annealing condition used in this study is a typical treatment condition for synthesizing an ordered PtCo intermetallic catalyst supported on carbon; improved stability is desired to prevent sintering during intermetallic PtCo formation [254]. The XRD patterns of fresh catalysts in Figure 4.2a shows fcc Pt peaks with identical intensity at 39.8° and 46.2° 2θ for all catalysts except Polyol-2. The high-intensity Pt peaks in the Polyol-2 catalyst indicate the formation of larger Pt NPs than other catalysts, which is confirmed by subsequent support subtraction and deconvolution of the XRD pattern (Figure 4.2d). The XRD particle size for all Pt/C catalysts is listed in Table 4.2. Figure 4.2c shows the XRD patterns for fresh SEA and Polyol-2 catalysts along with the bare support XRD pattern. The diffraction peaks of the SEA catalyst in Figure 4.2c broaden and shift to the left as Pt oxides form as observed previously for carbon and oxide-supported Pt NPs [184, 210, 211]. With careful support-subtraction and fitting as developed in prior studies [185, 209, 210], the peaks for the SEA catalyst were fitted with a combination of Pt and Pt_3O_4 (deconvolution of other catalysts are in Figure C.1). In contrast, only metallic Pt peaks appear for Polyol-2 catalyst, as shown in Figure 4.2d.

Table 4.2 revealed that metallic Pt NPs transform into Pt oxides when the XRD

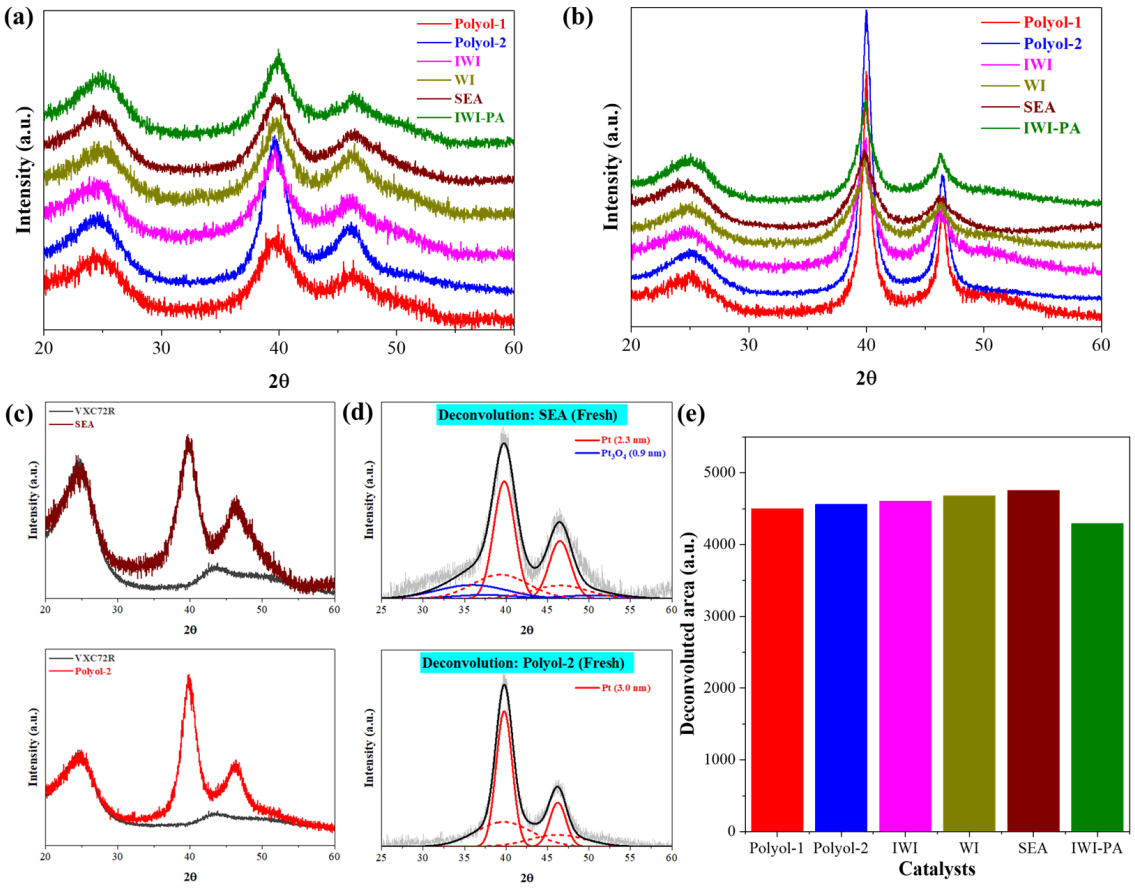

Figure 4.2 **XRD Characterization.** XRD patterns of (a) fresh and (b) annealed Pt/C catalysts; (c) XRD patterns of SEA and Polyol-2 catalysts with respect to XC72R (as purchased) pattern (d) Deconvolution after support subtraction of fresh SEA and Polyol-2 catalysts; (d) total area obtained after deconvolution.

particle size is below 3 nm, which agrees with previously published work by Banerjee et al. [184], who showed that partial Pt oxidation occurs for Pt particles with a size between 1.5 and 2.7 nm. However, the total deconvoluted area under Pt and Pt_3O_4 peaks are consistent for all catalysts (Figure 4.2e). Although the IWI-PA catalyst showed a slightly lower value of the deconvoluted area than others, the percentile difference is insignificant. The XRD patterns of annealed catalysts in Figure 2b demonstrated significant Pt sintering, especially for polyol and IWI-PA catalysts. The degree of sintering for SEA and WI catalysts were the lowest, while IWI showed

intermediate sintering after standard annealing, indicating strong MSI for SEA and WI catalysts [255]. Moreover, no Pt_3O_4 was observed after annealing treatment since the particle size for all catalysts was greater than 3 nm.

As mentioned, SEA is a type of WI with a controlled solution pH. Therefore, when the solution pH in WI approaches the optimal pH range for SEA, a portion of the precursor is adsorbed on the support due to electrostatic interaction, while rest of the precursor deposits by impregnation. In this study, the solution pH in the WI method was 2.2, which is close to the optimum SEA pH (=3.0) for the HCP-XC72R system. Thus, WI would be expected to exhibit weaker MSI than SEA, but stronger MSI than can be achieved with the other techniques. The metal adsorption in IWI is similar to the WI method as HCP precursor was used, but because of the high surface loading (m^2/L), IWI produces heterogeneous dispersion; a portion of the support is crowded with Pt NPs while other portions are empty or show lower particle density (Figure C.2), which increases the possibility of Pt sintering at high temperatures compared to SEA and WI. In the case of IWI-PA, a neutral precursor was used that does not electrostatically interact with the support, in contrast to IWI. Although the XRD particle size of fresh IWI-PA catalyst is similar to IWI, annealed catalysts sinters more drastically for IWI-PA than IWI, which may be due to the weaker MSI resulting from IWI-PA (Figure 4.2b).

The thermal stability of Pt NPs prepared by SEA and WI was also explained by the TEM characterization of fresh and annealed catalysts. For example, the TEM micrograph of fresh SEA catalyst in Figure 3a showed highly dispersed and narrowly distributed Pt NPs on XC72R, similar to Polyol-1 (Figure 4.3a) and Polyol-2 (Figure C.2). On the other hand, Pt NPs prepared by WI were highly dispersed on XC72R. However, some clusters of particles were observed that might cause by the combined effects of electrostatic interactions and impregnation (Figure 4.3a), which was explained by Job et al. [256], who found that the portion of precursor adsorbed

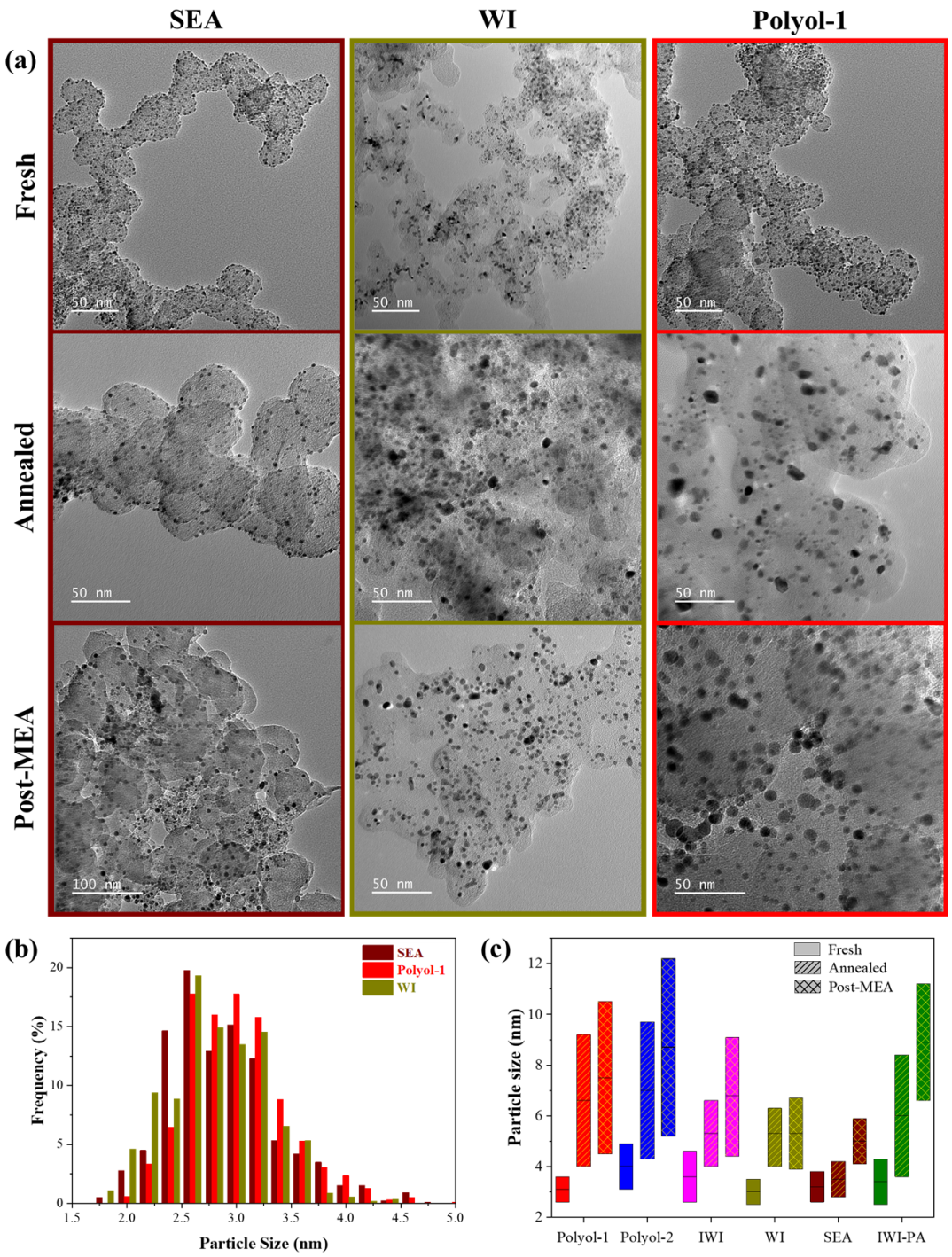

Figure 4.3 **TEM Characterization.** (a) TEM images of fresh (as-prepared), annealed, and post-MEA catalysts and (b) particle size distribution of fresh catalysts prepared by SEA, WI, and Polyol-1; (c) the growth of Pt particles due to high temperature annealing and 30K AST. Annealing was performed under 6%H_2/He at 750 °C for 12 h, and AST was performed at a potential between 0.6 and 0.95 V under H_2/N_2 (150 kPa_{abs}, 80 °C, 100%RH, 200/200 SCCM) for 30,000 cycles.

by electrostatic interaction produces smaller Pt NPs, while the excess portion of precursor in the solution leads to the formation of larger particles after reduction treatment. The particle size distribution for fresh catalysts prepared by the SEA, WI, and Polyol-1 method is presented in Figure 4.3b, demonstrating a similar particle size distribution for these catalysts. However, others made a broader range of particle sizes due to a lack of electrostatic interactions between the support and the precursor. In addition, when these catalysts were subjected to the standard annealing treatment, Pt NPs in polyol catalysts significantly agglomerated and formed larger particles.

In contrast, strong MSI in SEA catalyst inhabits the mobility of Pt NPs, limiting metal sintering even under extreme treatment conditions [257]. The growth of Pt NPs due to the standard annealing treatment is shown with a floating bar chart in Figure 4.3c, which is made based on volume-averaged diameter ± standard deviation. As seen in Figure 4.3c, the degree of particle growth due to annealing treatment increases in the order: SEA < WI < IWI < IWI-PA < Polyol-1 < Polyol-2. The highest range of particle growth was observed for Polyol-2 catalyst as pre-prepared Pt NPs were deposited on carbon without any chemical interactions between Pt NPs and support, which caused instability of Pt NPs at higher temperatures, leading to significant Pt sintering. Although Pt NPs in Polyol-1 behaved similar to Polyol-2, they were slightly more resistant to sintering than Polyol-2 at high temperatures (Table 4.3). In the Polyol-1 method, the precursor solution was physically mixed with dispersed XC72R in EG solution before reducing metal precursor to NPs. Therefore, a portion of the precursor might be electrostatically adsorbed on the support since the pH of the mixture was close to 2.5. However, support-precursor interactions in Polyol-1 are expected to be less than WI due to the probable adverse effects of EG on the adsorption process. Furthermore, IWI-PA showed the highest sintering among the impregnated catalysts. As mentioned above, IWI-PA catalyst was prepared using a neutral precursor, resulting in weaker MSI than in IWI and WI. Among WI and

Table 4.3 The size of Pt NPs estimated by TEM for fresh, annealed, and post-MEA samples.

Catalyst	TEM particle size [nm]		
	Fresh	Annealed	Post-MEA
Polyol-1	3.1	6.6	7.5
Polyol-2	4.0	7.0	8.7
IWI	3.6	5.3	6.8
IW	3.0	5.3	5.3
SEA	3.2	3.5	5.0
IWI-PA	3.4	6.0	8.9

IWI, WI showed more resistance to thermal sintering because the precursor solution in the WI method was closer to the optimal SEA pH. Additionally, the IWI method involves a low pH that can cause a synergistic effect during adsorption. The lowest particle growth was found for the SEA catalyst as Pt NPs were deposited on support with complete electrostatic interactions.

As-prepared catalysts were also subjected to 30K AST cycles from 0.6 to 0.95 V under H_2/N_2 environments in PEMFCs (details in experimental section) to evaluate their stability under fuel cell conditions. These catalysts were tested as the cathode in MEAs under H_2/air atmosphere using 5 cm^2 differential cells with 14 parallel flow channels. Similar to thermal stability results, Pt/C catalysts prepared by the SEA method exhibited superior stability during AST, with the lowest (41%) mass activity (MA) loss at 0.9 V under 150 kPa_{abs} H_2/O_2 (Figure 4.4e), while the MA loss was above 50% for other catalysts. The slightly lower MA of SEA catalyst prior to AST (BOL) may be due to insufficient breakin. However, the SEA catalyst had the highest MA after 30K AST cycles (EOL), suggesting the strongest MSI among the tested catalysts. The EOL MA after durability testing decreased in the order: SEA < WI < IWI < IWI-PA < Polyol-1 < Polyol-2. Also, the SEA catalyst produced a higher current density than impregnated and polyol catalysts in the usual operating potential range (> 0.6 V). The generated current density for SEA catalyst was about 0.16 A/cm^2 at

0.8 V (Figure 4.4c), which is higher than a similar commercial TEC10V20E catalyst (0.10 A/cm^2 at 0.80 V) [254]. According to Figure 4.4c, the current density at 0.8 V for SEA and WI was the same, but the SEA catalyst lost 43% of current density after AST, compared to 56% for the WI catalyst. Also, IWI and IWI-PA had similar BOL current density at 0.8 V (but lower than SEA and WI), and IWI-PA catalyst showed about 5% more current density loss in EOL. Furthermore, the BOL current density of Polyol-1 and Polyol-2 catalysts at 0.8 V was about 31% and 63% lower than WI and SEA catalysts, and they ended up with the lowest current density value at 0.8 V after the AST. The MEA performance of the SEA catalyst was also examined at 0.8 A/cm^2 (Figure 4.4d). The potential loss of SEA catalyst at 0.8 A/cm^2 was the lowest (6.5%) compared to WI (9.9%), IWI (10.9%), Polyol-1 (16.3%), Polyol-2 (13.4%), and IWI-PA (21.2%).

Additionally, the BOL performance of WI and IWI catalysts were slightly lower than the SEA catalyst with the following trend: SEA > WI > IWI (Figure 4.4a), indicating the impact of electrostatic interaction in both WI and IWI. However, the durability of Pt/C catalysts after 30K AST was significantly affected by the degree of MSI, as stronger MSI provided higher durability [258]. The lowest durability of IWI catalyst among the above three was attributed to the Pt NPs agglomeration under ORR conditions which was confirmed by TEM analysis of post-MEA sample (Figure C.2). The TEM micrographs of the post-MEA WI sample demonstrated less agglomeration of Pt NPs than IWI. At the same time, agglomeration was comparatively low for the post-MEA SEA sample (Figure 4.3a), indicating the least particle mobility of SEA catalyst under ORR conditions. Conversely, the durability of IWI-PA was found to be the worst of the tested catalysts, even though the BOL performance was close to IWI, suggesting lesser MSI in IWI-PA catalyst than IWI. The TEM comparison on the post-MEA sample of SEA and Polyol-1 catalysts (Figure 4.3a) revealed that Polyol-1 catalyst has lower interactions with the support as higher agglomeration

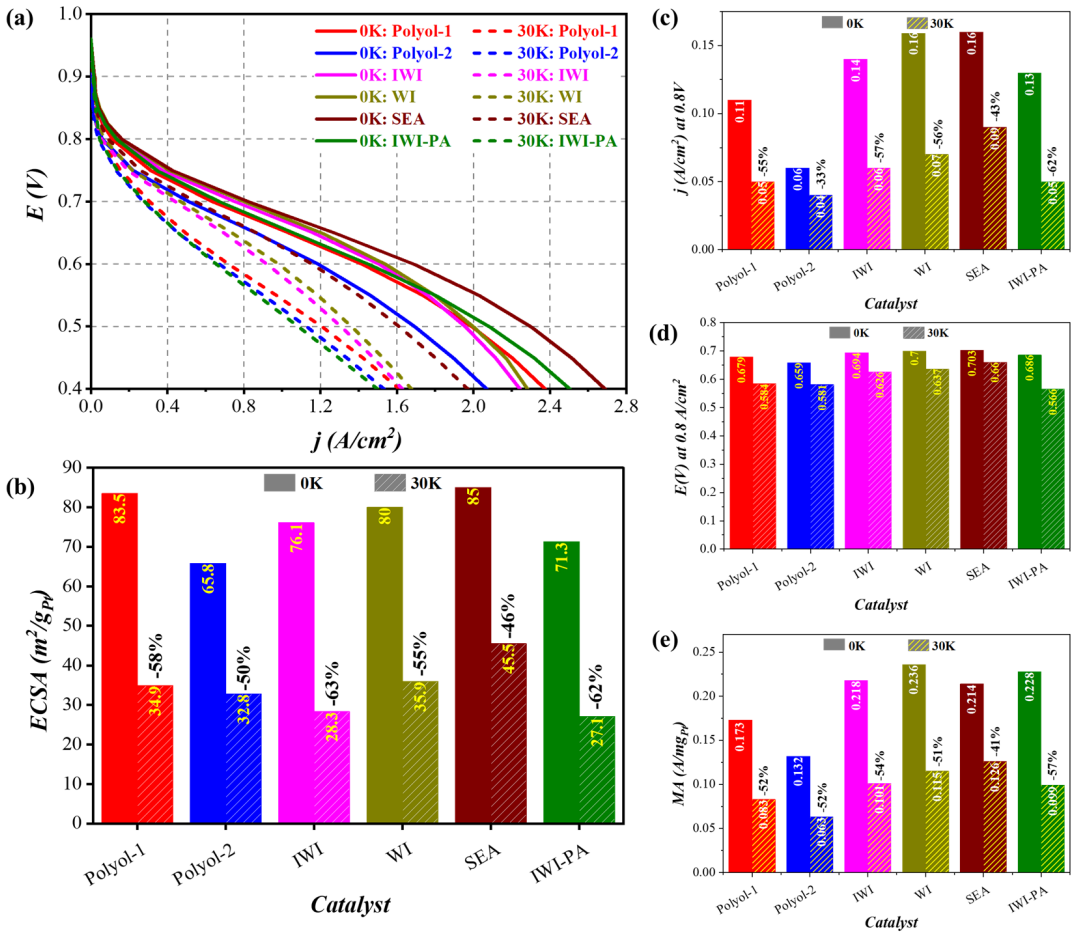

Figure 4.4 **Fuel cell testing results of Pt/C catalysts.** (a) polarization curves before (0K) and after AST (30K) – performed in 1000/3000 SCCM H_2/air; (b) CO-ECSA at 0K and 30K; (c) current density (j) at 0.8 V and (d) cell voltage at 0.8 A/cm^2 – obtained from polarization curves at 0K and 30K; and (e) mass activity at 0K and 30K – measured in 1000/3000 H_2/O_2 at 0.9 V (iR-free). All experiments were conducted at 80 °C, 150 kPa, and 100% RH.

occurred for Polyol-1 catalyst than SEA.

Among the two polyol-synthesized catalysts, Polyol-1 showed higher BOL and EOL performance than the Polyol-2 catalyst, suggesting superior MSI of Polyol-1 over Polyol-2 catalyst. As mentioned, Polyol-1 might produce some degree of electrostatic interaction between metal precursor and support during synthesis, while Polyol-2 is a type of physical mixing of Pt NPs and support. Also, fresh Polyol-2 catalyst produced larger particles than Polyol-1, which lowered the accessible Pt surface area, resulting in poor MEA performance. The TEM particle size for the fresh, annealed, and post-MEA samples are summarized in Table 4.3.

The ECSA results, measured by CO stripping at 100% RH (details of CO-ECSA measurement in experimental section), are shown in Figure 4.4b, demonstrating the accessible Pt surface for the ORR. The ECSA value is dependent on the particle size, inter-particle distance, and metal weight percent. When Pt NPs are closely present within a critical part (low inter-particle distance), mutual effects on the diffusion or other parameters limit the number of available surface sites for the reaction [259, 260]. Since this study used similar metal weight percent for each Pt/C catalyst, particle size and inter-particle distance are critical in changing the ECSA value. For example, the TEM particle size for fresh SEA, WI, and Polyol-1 catalysts increased in the order: WI $<$ Polyol-1 $<$ SEA with minimal difference. Therefore, it can be expected that the CO-ECSA should follow the opposite order since ECSA is inversely proportional to the particle size [260]. However, the SEA catalyst had the highest ECSA compared to the Polyol-1 and WI catalysts. The visual inspection of TEM images in Figure 3a showed that as-prepared SEA and Polyol-1 had similar particle dispersion and inter-particle distance. The reason for the higher ECSA value of SEA than Polyol-1 remains to be determined but could be related to differences in surface cleanliness resulting from the different synthesis techniques. Also, the WI catalyst contained some clusters (Figure 4.3a, fresh sample) that decreased the accessible Pt surface.

The same explanation applies to IWI and IWI-PA catalysts since both had uneven distributions of Pt NPs with cluster formation in the fresh samples. Furthermore, the support surface with denser particles had a lower inter-particle distance, resulting in lower ECSA values for IWI and IWI-PA catalysts than WI. In the case of Polyol-2, the low ECSA may be attributed to (1) the larger particles formation during synthesis, (2) possible contamination of the Pt surface, and (3) lower inter-particle distance.

On the other hand, IWI and IWI-PA catalysts had lesser growth of particles after AST testing than polyol catalysts due to the higher MSI. However, ECSA in EOL was higher for polyol catalysts due to better dispersion and lower inter-particle distance. The broad range of TEM micrographs for polyol and impregnated catalysts are shown in Figure C.3, which demonstrates the dispersion of Pt NPs over the surface for post-MEA samples. It can be seen that a portion of the support surface for IWI and IWI-PA catalysts was still empty, while the particle size of these catalysts was smaller than polyol catalysts, indicating tight packing of Pt NPs in a comparatively lesser support surface, resulting in lower ECSA. Conversely, in SEA catalysts, Pt NPs were homogeneously dispersed with minimal Pt sintering even after the AST, owing to the higher MSI, leading to the highest ECSA after AST testing.

As discussed above, the different Pt deposition techniques resulted in strikingly different behavior during annealing and during fuel cell testing, even in cases where particle size distribution and dispersion were similar. Difference in the MSI at the interface between Pt and XC72R were hypothesized to cause these differences. Therefore, XPS (details in section experimental section) was used to qualitatively assess differences in MSI by observing the binding energy shift of metallic Pt in the Pt 4f spectra. The relative shift of binding energy of metallic Pt for SEA, WI, Polyol-1, and Polyol-2 were shown with respect to the IWI catalyst in Figure 4.5 (full spectrum of Pt/C catalysts and C 1s peak of XC72R are shown in Figure C.4). The highest positive (towards higher energy) binding energy shift was observed for the SEA cata-

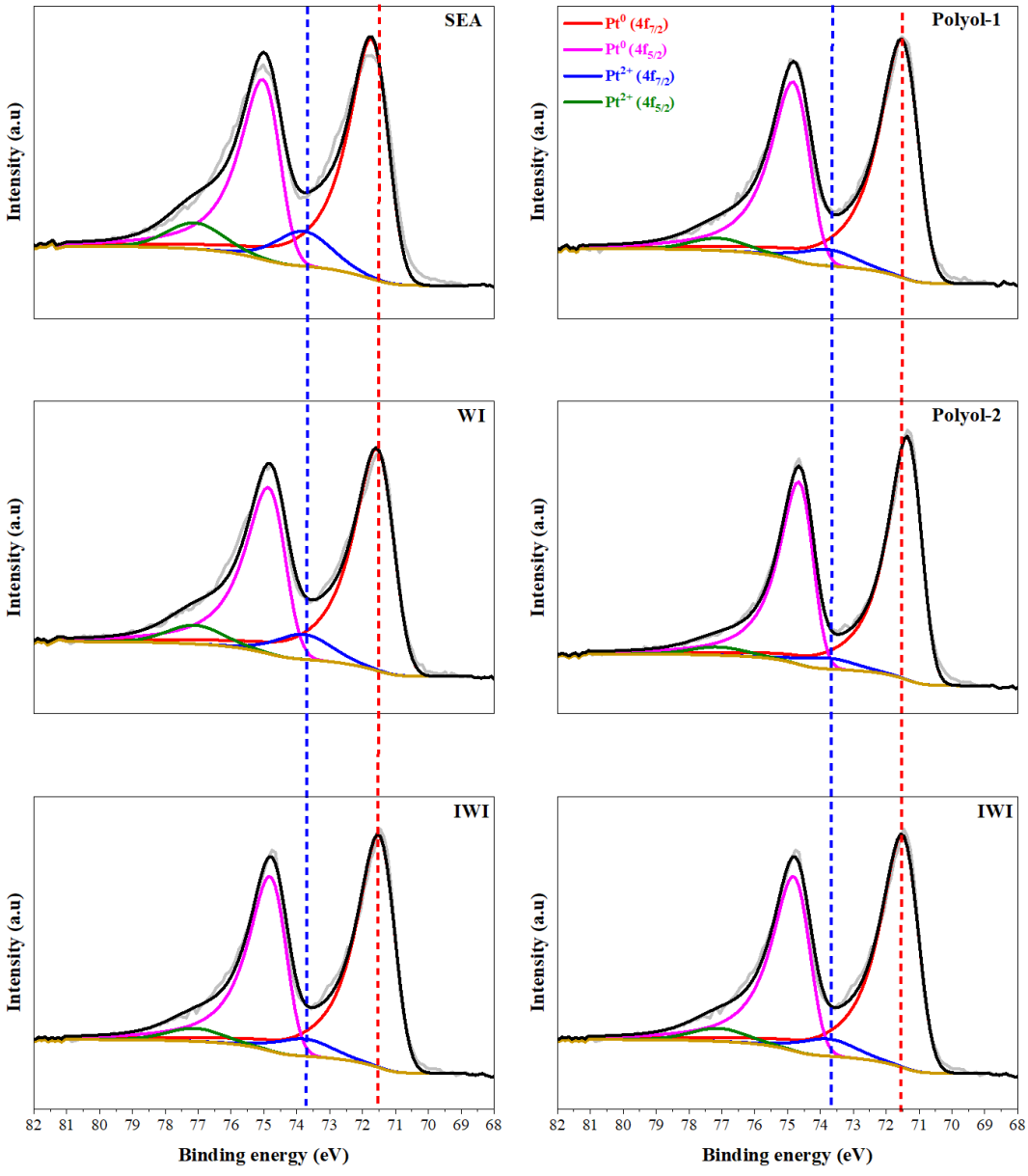

Figure 4.5 **XPS characterization.** XPS spectra of Pt 4f for Pt/C catalysts prepared by SEA, WI, IWI, Polyol-1, and Polyol-2. The red and blue dotted lines correspond to metallic Pt and PtO, respectively.

lyst, followed by WI. In addition, Polyol-1 and IWI showed identical binding energy for metallic Pt, while a negative (towards lower energy) energy shift was observed for Polyol-2 catalyst. Typically, a positive shift occurs due to charge transfer from the metal to the support; the higher the positive shift, the more the charge transfer to the support [261]. Keiko and Mikio demonstrated that the positive shift of binding energy is attributed to Pt-support electronic effects; the more robust the electronic interactions at the metal-support interface, the higher the shifting [262]. Besides MSI due to electronic effects, particle size and nature of the support are also critical to positive energy shift [263–265]. Since this study used identical metal and support materials, it was assumed that support had a similar impact on the binding energy shift for all catalysts. Additionally, Polyol-1 catalyst produced smaller NPs than IWI (Table 4.3), so higher binding energy for Polyol-1 catalyst was expected. However, the identical binding energy of metallic Pt for Polyol-1 and IWI catalysts indicates that MSI in IWI catalyst is higher compared to Polyol-1 catalyst. On the other hand, when Polyol-1 catalyst was compared with WI, only electronic effects were accounted to demonstrate the positive energy shift since the particle size difference between them was minimal compared to the difference between IWI and Polyol-1. Therefore, based on the above discussion, the MSI can be summarized in the following order: SEA > WI > IWI > Polyol-1 > Polyol-2, which agrees with both MEA durability and thermal stability results.

4.5 Conclusions

In summary, this work explored the impact of MSI on the stability of Pt/C catalysts under fuel cell and high-temperature environments. The thermal stability and MEA durability of Pt/C catalysts were evaluated by comparing a series of Pt/C catalysts prepared using different synthesis techniques, including polyol, IWI, WI, and SEA. The SEA method tuned the MSI more effectively than other methods, confirmed by systemic analyses of experimental XRD, XPS, and TEM data. Furthermore, the

low loss in MA and polarization performance after AST for SEA catalysts validated the hypothesis of the SEA catalyst's highest MSI. This work also explained how the stability of Pt/C catalysts is influenced by the degree of electrostatic interactions, as techniques that involve higher degrees of electrostatic adsorption result in higher MSI and stability.

Bibliography

[1] M Boudart. “Perspectives in Catalysis”. In: (1992).

[2] Eric Keightley Rideal. *Catalysis in theory and practice*. Macmillan and Company, limited, 1919.

[3] G Ertl, H Knözinger, and J Weitkamp. *Handbook of heterogeneous catalysis*. Weinheim: VCH, 1997.

[4] National Research Council. *Catalysis looks to the future*. National Academies Press, 1992.

[5] Sieghard E Wanke and Peter C Flynn. “The sintering of supported metal catalysts”. In: *Catalysis Reviews* 12.1 (1975), pp. 93–135.

[6] John N Armor. “New catalytic technology commercialized in the USA during the 1990s”. In: *Applied Catalysis A: General* 222.1-2 (2001), pp. 407–426.

[7] B A Averill et al. *Catalysis: An integrated approach*. Elsevier, 1999.

[8] Calvin H Bartholomew and Robert J Farrauto. *Fundamentals of industrial catalytic processes*. John Wiley & Sons, 2011.

[9] Ib Chorkendorff and Johannes W Niemantsverdriet. *Concepts of modern catalysis and kinetics*. John Wiley & Sons, 2017.

[10] John Meurig Thomas and W John Thomas. *Principles and practice of heterogeneous catalysis*. John Wiley & Sons, 2014.

[11] Wolf Vielstich, Arnold Lamm, and Hubert Gasteiger. “Handbook of fuel cells. Fundamentals, technology, applications”. In: (2003).

[12] Seungdoo Park, John M Vohs, and Raymond J Gorte. “Direct oxidation of hydrocarbons in a solid-oxide fuel cell”. In: *Nature* 404.6775 (2000), pp. 265–267.

[13] S Ha, R Larsen, and R I Masel. “Performance characterization of Pd/C nanocatalyst for direct formic acid fuel cells”. In: *Journal of Power Sources* 144.1 (2005), pp. 28–34.

[14] Avelino Corma and Hermenegildo Garcia. “Lewis acids: from conventional homogeneous to green homogeneous and heterogeneous catalysis”. In: *Chemical Reviews* 103.11 (2003), pp. 4307–4366.

[15] Roger A Sheldon. “Green solvents for sustainable organic synthesis: state of the art”. In: *Green Chemistry* 7.5 (2005), pp. 267–278.

[16] Jose E Herrera et al. “Relationship between the structure/composition of Co–Mo catalysts and their ability to produce single-walled carbon nanotubes by CO disproportionation”. In: *Journal of Catalysis* 204.1 (2001), pp. 129–145.

[17] George W Huber, J W Shabaker, and J A Dumesic. “Raney Ni-Sn catalyst for H2 production from biomass-derived hydrocarbons”. In: *Science* 300.5628 (2003), pp. 2075–2077.

[18] George W Huber et al. “Production of liquid alkanes by aqueous-phase processing of biomass-derived carbohydrates”. In: *Science* 308.5727 (2005), pp. 1446–1450.

[19] Sriram Varadarajan and Dennis J Miller. “Catalytic upgrading of fermentation-derived organic acids”. In: *Biotechnology progress* 15.5 (1999), pp. 845–854.

[20] A K Datye et al. “Particle size distributions in heterogeneous catalysts: What do they tell us about the sintering mechanism?” English. In: *Catalysis Today* 111.1-2 (2006), pp. 59–67.

[21] P N Plessow and F Abild-Pedersen. “Sintering of Pt Nanoparticles via Volatile PtO2: Simulation and Comparison with Experiments”. English. In: *ACS Catalysis* 6.10 (2016), pp. 7098–7108.

[22] Søren Bredmose Simonsen et al. “Ostwald ripening in a Pt/SiO2 model catalyst studied by in situ TEM”. In: *Journal of Catalysis* 281.1 (2011), pp. 147–155.

[23] Calvin H Bartholomew. “Sintering and redispersion of supported metals: Perspectives from the literature of the past decade”. In: *Studies in Surface Science and Catalysis*. Vol. 111. Elsevier, 1997, pp. 585–592.

[24] W J Diao et al. “Preparation and Characterization of Pt-Ru Bimetallic Catalysts Synthesized by Electroless Deposition Methods”. English. In: *ACS Catalysis* 5.9 (2015), pp. 5123–5134.

[25] J M M Tengco et al. “Synthesis and Electrochemical Evaluation of Carbon Supported Pt-Co Bimetallic Catalysts Prepared by Electroless Deposition and Modified Charge Enhanced Dry Impregnation”. English. In: *Catalysts* 6.6 (2016).

[26] B T Egelske et al. “An analysis of electroless deposition derived Ni-Pt catalysts for the dry reforming of methane”. English. In: *Journal of Catalysis* 381 (2020), pp. 374–384.

[27] Y G Chen et al. “Nitrogen Doping Effects on Carbon Nanotubes and the Origin of the Enhanced Electrocatalytic Activity of Supported Pt for Proton-Exchange Membrane Fuel Cells”. English. In: *Journal of Physical Chemistry C* 115.9 (2011), pp. 3769–3776.

[28] T Holme et al. “First principles study of doped carbon supports for enhanced platinum catalysts”. English. In: *Physical Chemistry Chemical Physics* 12.32 (2010), pp. 9461–9468.

[29] Y K Zhou et al. “Improving PEM fuel cell catalyst activity and durability using nitrogen-doped carbon supports: observations from model Pt/HOPG systems”. English. In: *Journal of Materials Chemistry* 19.42 (2009), pp. 7830–7838.

[30] Stephen Maldonado and Keith J Stevenson. “Influence of Nitrogen Doping on Oxygen Reduction Electrocatalysis at Carbon Nanofiber Electrodes”. In: *The Journal of Physical Chemistry B* 109.10 (2005), pp. 4707–4716.

[31] C Jackson et al. “Electronic metal-support interaction enhanced oxygen reduction activity and stability of boron carbide supported platinum”. English. In: *Nature Communications* 8 (2017).

[32] Tom W van Deelen, Carlos Hernández Mejía, and Krijn P de Jong. “Control of metal-support interactions in heterogeneous catalysts to enhance activity and selectivity”. In: *Nature Catalysis* 2.11 (2019), pp. 955–970.

[33] J Zecevic et al. “Nanoscale intimacy in bifunctional catalysts for selective conversion of hydrocarbons”. English. In: *Nature* 528.7581 (2015), pp. 245–+.

[34] P M Arnal, M Comotti, and F Schuth. “High-temperature-stable catalysts by hollow sphere encapsulation”. English. In: *Angewandte Chemie-International Edition* 45.48 (2006), pp. 8224–8227.

[35] Gianfranco Pacchioni and Hans-Joachim Freund. “Controlling the charge state of supported nanoparticles in catalysis: lessons from model systems”. In: *Chemical Society Reviews* 47.22 (2018), pp. 8474–8502.

[36] J A Farmer and C T Campbell. “Ceria Maintains Smaller Metal Catalyst Particles by Strong Metal-Support Bonding”. English. In: *Science* 329.5994 (2010), pp. 933–936.

[37] C W Edmunds et al. “Vapor-Phase Stabilization of Biomass Pyrolysis Vapors Using Mixed-Metal Oxide Catalysts”. English. In: *Acs Sustainable Chemistry & Engineering* 7.7 (2019), pp. 7386–7394.

[38] I V Yentekakis et al. “Stabilization of catalyst particles against sintering on oxide supports with high oxygen ion lability exemplified by Ir-catalyzed decomposition of N2O”. English. In: *Applied Catalysis B-Environmental* 192 (2016), pp. 357–364.

[39] W Yin et al. “Stabilization of fast pyrolysis liquids from biomass by catalytic hydrotreatment using Raney nickel "type" catalysts”. English. In: *Fuel Processing Technology* 219 (2021).

[40] S P Ding et al. “High-temperature flame spray pyrolysis induced stabilization of Pt single-atom catalysts”. English. In: *Applied Catalysis B-Environmental* 281 (2021).

[41] A P Dral et al. “Micropore structure stabilization in organosilica membranes by gaseous catalyst post-treatment”. English. In: *Journal of Membrane Science* 548 (2018), pp. 157–164.

[42] D D Sun. “Stabilization treatment for reutilization of spent refinery catalyst into value-added product”. English. In: *Energy Sources* 25.6 (2003), pp. 607–615.

[43] L Bonneviot, D Olivier, and M Che. “Stabilization of Ni+ by Thermal-Treatment of Silica Nickel-Catalysts”. English. In: *Journal of the Chemical Society-Chemical Communications* 16 (1982), pp. 952–953.

[44] Claire Gillan et al. “Ethane Steam Reforming over a Platinum/Alumina Catalyst: Effect of Sulfur Poisoning”. In: *Industrial & Engineering Chemistry Research* 52.37 (2013), pp. 13350–13356.

[45] Um-e-Salma Amjad et al. “Methane Steam Reforming on the Pt/CeO2 Catalyst: Effect of Daily Start-Up and Shut-Down on Long-Term Stability of the Catalyst”. In: *Industrial & Engineering Chemistry Research* 58.36 (2019), pp. 16395–16406.

[46] A Claudio-Piedras et al. “One dimensional Pt/CeO2-NR catalysts for hydrogen production by steam reforming of methanol: Effect of Pt precursor”. English. In: *Catalysis Today* 360 (2021), pp. 55–62.

[47] H Amanuma, H Nanao, and M Shirai. “Cinnamaldehyde Hydrogenation over Platinum Nanosheet Intercalated Graphite Layers in Supercritical Carbon Dioxide Solvent”. English. In: *Chemistry Letters* 47.4 (2018), pp. 475–478.

[48] S X Bai et al. “Highly Efficient Carbon Dioxide Hydrogenation to Methanol Catalyzed by Zigzag Platinum-Cobalt Nanowires”. English. In: *Small* 13.22 (2017).

[49] B Zhao et al. “Electrocatalytic hydrogenation of furfural to furfuryl alcohol using platinum supported on activated carbon fibers”. English. In: *Electrochimica Acta* 135 (2014), pp. 139–146.

[50] Y Motoyama et al. “Platinum Nanoparticles Supported on Nitrogen-doped Carbon Nanofibers as Efficient Poisoning Catalysts for the Hydrogenation of Nitroarenes”. English. In: *Chemcatchem* 3.10 (2011), pp. 1578–1581.

[51] S D Kushch, N S Kuyunko, and B P Tarasov. “Preparation of Hydrogenation Catalysts Based on Platinum Nanoparticles Supported on Carbon Nanomaterials”. English. In: *Kinetics and Catalysis* 50.6 (2009), pp. 860–862.

[52] S D Kushch, N S Kujunko, and B P Tarasov. “Platinum nanoparticles on carbon nanomaterials with graphene structure as hydrogenation catalysts”. English. In: *Russian Journal of General Chemistry* 79.4 (2009), pp. 706–710.

[53] H Begum and Y B Kim. “Improvement of Catalytic Activity of Platinum Nanoparticles Decorated Carbon Graphene Composite on Oxygen Electroreduction for Fuel Cells”. English. In: *Processes* 7.9 (2019).

[54] Z A C Ramli and S K Kamarudin. “Platinum-Based Catalysts on Various Carbon Supports and Conducting Polymers for Direct Methanol Fuel Cell Applications: a Review”. English. In: *Nanoscale Research Letters* 13 (2018).

[55] R C P Oliveira et al. “Platinum/polypyrrole-carbon electrocatalysts for direct borohydride-peroxide fuel cells”. English. In: *Applied Catalysis B-Environmental* 238 (2018), pp. 454–464.

[56] F Mirzaei, M J Parnian, and S Rowshanzamir. “Durability investigation and performance study of hydrothermal synthesized platinum-multi walled carbon nanotube nanocomposite catalyst for proton exchange membrane fuel cell”. English. In: *Energy* 138 (2017), pp. 696–705.

[57] S S Gwebu et al. “Platinum Nanoparticles Supported on Carbon Nanodots as Anode Catalysts for Direct Alcohol Fuel Cells”. English. In: *International Journal of Electrochemical Science* 12.7 (2017), pp. 6365–6378.

[58] C X Ding, F Dong, and Z C Tang. “Construction of hollow carbon polyhedron supported Pt catalyst for methanol electrocatalytic oxidation”. English. In: *Electrochimica Acta* 390 (2021).

[59] Y P Luo et al. “Improved electrocatalytic activity of Pt catalyst supported on core-shell CMs@NiO for methanol oxidation”. English. In: *New Journal of Chemistry* 45.29 (2021), pp. 12879–12885.

[60] H F Wang et al. “Photoassisted Reduction Synthesis of Pt@SnO2/Graphene Catalysts with Excellent Activities toward Methanol Oxidation”. English. In: *Energy & Fuels* 35.15 (2021), pp. 12516–12526.

[61] Y M Xing et al. “Single Atomic Pt on SrTiO3 Catalyst in Reverse Water Gas Shift Reactions”. English. In: *Catalysts* 11.6 (2021).

[62] S S Schmidt. “Water gas shift reaction for CeO2-supported Pt catalyst occurs at Pt perimeter”. English. In: *Mrs Bulletin* 46.8 (2021), p. 672.

[63] Y Y Li et al. “Dynamic structure of active sites in ceria-supported Pt catalysts for the water gas shift reaction”. English. In: *Nature Communications* 12.1 (2021).

[64] K Matsubara et al. “Photocatalytic water splitting over Pt-loaded TiO2 (Pt/TiO2) catalysts prepared by the polygonal barrel-sputtering method”. English. In: *Applied Catalysis B-Environmental* 254 (2019), pp. 7–14.

[65] Y M Zhang et al. “Plasmon-Induced Water Splitting on Ag-Alloyed Pt Single-Atom Catalysts”. English. In: *Frontiers in Chemistry* 9 (2021).

[66] X F Zhang et al. “Green synthesis of g-C3N4-Pt catalyst and application to photocatalytic hydrogen evolution from water splitting”. English. In: *Fullerenes Nanotubes and Carbon Nanostructures* 26.10 (2018), pp. 688–695.

[67] James A Dumesic, George W Huber, and Michel Boudart. “Principles of Heterogeneous Catalysis”. In: *Handbook of Heterogeneous Catalysis*.

[68] J R Regalbuto. “Paving the trail blazed by Jim Schwarz: A scientific method to prepare supported metal catalysts”. English. In: *Abstracts of Papers of the American Chemical Society* 230 (2005), U1085–U1086.

[69] G Busca. “The use of vibrational spectroscopies in studies of heterogeneous catalysis by metal oxides: An introduction”. English. In: *Catalysis Today* 27.3-4 (1996), pp. 323–352.

[70] S Pothaya et al. “Preparation of Pt/graphene catalysts for polymer electrolyte membrane fuel cells by strong electrostatic adsorption technique”. English. In: *International Journal of Hydrogen Energy* 44.48 (2019), pp. 26361–26372.

[71] R Arulmurugan et al. “Effect of zinc substitution on Co-Zn and Mn-Zn ferrite nanoparticles prepared by co-pecipitation”. English. In: *Journal of Magnetism and Magnetic Materials* 288 (2005), pp. 470–477.

[72] I Sondi, D V Goia, and E Matijevic. “Preparation of highly concentrated stable dispersions of uniform silver nanoparticles”. English. In: *Journal of Colloid and Interface Science* 260.1 (2003), pp. 75–81.

[73] A L Wang et al. “Methanol Dehydrogenation to Methyl Formate Catalyzed by Cu/SiO2 Catalysts: Impact of Precipitation Procedure and Calcination Temperature”. English. In: *Russian Journal of Applied Chemistry* 94.9 (2021), pp. 1302–1312.

[74] F Fievet et al. “Homogeneous and Heterogeneous Nucleations in the Polyol Process for the Preparation of Micron and Sub-Micron Size Metal Particles”. English. In: *Solid State Ionics* 32-3 (1989), pp. 198–205.

[75] W H Wang et al. “Synthesis and characterization of Pt-Cu bimetallic alloy nanoparticles by reverse micelles method”. English. In: *Colloids and Surfaces a-Physicochemical and Engineering Aspects* 273.1-3 (2006), pp. 35–42.

[76] L Wolski et al. “Influence of Co-Precipitation Agent on the Structure, Texture and Catalytic Activity of Au-CeO2 Catalysts in Low-Temperature Oxidation of Benzyl Alcohol”. English. In: *Catalysts* 11.5 (2021).

[77] O D Jayakumar et al. “Magnetism in Mn-doped ZnO nanoparticles prepared by a co-precipitation method”. English. In: *Nanotechnology* 17.5 (2006), pp. 1278–1285.

[78] G S Qi, R T Yang, and R Chang. “MnOx-CeO2 mixed oxides prepared by co-precipitation for selective catalytic reduction of NO with NH3 at low temperatures”. English. In: *Applied Catalysis B-Environmental* 51.2 (2004), pp. 93–106.

[79] Martijn K van der Lee et al. “Deposition Precipitation for the Preparation of Carbon Nanofiber Supported Nickel Catalysts”. In: *Journal of the American Chemical Society* 127.39 (2005), pp. 13573–13582.

[80] P Burattin, M Che, and C Louis. “Characterization of the Ni(II) phase formed on silica upon deposition-precipitation”. English. In: *Journal of Physical Chemistry B* 101.36 (1997), pp. 7060–7074.

[81] D L Nguyen et al. “Deposition-precipitation versus anionic-exchange Au/Al2O3 catalysts: A comparative investigation towards the selective reduction of NOx”. English. In: *Catalysis Communications* 26 (2012), pp. 225–230.

[82] M H Seo et al. “The graphene-supported Pd and Pt catalysts for highly active oxygen reduction reaction in an alkaline condition”. English. In: *Electrochemistry Communications* 13.2 (2011), pp. 182–185.

[83] H Dong, Y C Chen, and C Feldmann. “Polyol synthesis of nanoparticles: status and options regarding metals, oxides, chalcogenides, and non-metal elements”. English. In: *Green Chemistry* 17.8 (2015), pp. 4107–4132.

[84] Andrew Phillip Wong. “The Rational Synthesis of Bimetallic Catalysts on Oxide Supports”. In: (2018).

[85] John R Regalbuto. “Electrostatic Adsorption”. In: *Synthesis of Solid Catalysts*. 2009, pp. 33–58.

[86] J P Brunelle. “Preparation of Catalysts by Metallic Complex Adsorption on Mineral Oxides”. English. In: *Pure and Applied Chemistry* 50.9-10 (1978), pp. 1211–1229.

[87] L D’Souza, J R Regalbuto, and J T Miller. “Preparation of carbon supported cobalt by electrostatic adsorption of [Co(NH3)(6)]Cl-3”. English. In: *Journal of Catalysis* 254.2 (2008), pp. 157–169.

[88] N Santhanam et al. “Nature of Metal Catalyst Precursors Adsorbed onto Oxide Supports”. English. In: *Catalysis Today* 21.1 (1994), pp. 141–156.

[89] W A Spieker and J R Regalbuto. “A fundamental model of platinum impregnation onto alumina”. English. In: *Chemical Engineering Science* 56.11 (2001), pp. 3491–3504.

[90] M Schreier and J R Regalbuto. “A fundamental study of Pt tetraammine impregnation of silica 1. The electrostatic nature of platinum adsorption”. English. In: *Journal of Catalysis* 225.1 (2004), pp. 190–202.

[91] Q Liu et al. “A pinch of salt to control supported Pt nanoparticle size”. English. In: *Catalysis Today* 280 (2017), pp. 246–252.

[92] H R Cho and J R Regalbuto. “The rational synthesis of Pt-Pd bimetallic catalysts by electrostatic adsorption”. English. In: *Catalysis Today* 246 (2015), pp. 143–153.

[93] R M Heck and R J Farrauto. “Automobile exhaust catalysts”. English. In: *Applied Catalysis a-General* 221.1-2 (2001), pp. 443–457.

[94] Y J Song et al. “Bimetallic Ag-Ir/Al2O3 catalysts prepared by electroless deposition: Characterization and kinetic evaluation”. English. In: *Journal of Catalysis* 315 (2014), pp. 59–66.

[95] I Ohno, O Wakabayashi, and S Haruyama. “Anodic-Oxidation of Reductants in Electroless Plating”. English. In: *Journal of the Electrochemical Society* 132.10 (1985), pp. 2323–2330.

[96] J Rebelli et al. “Synthesis and characterization of Au-Pd/SiO2 bimetallic catalysts prepared by electroless deposition”. English. In: *Journal of Catalysis* 270.2 (2010), pp. 224–233.

[97] Florence Gauthard, Florence Epron, and Jacques Barbier. “Palladium and platinum-based catalysts in the catalytic reduction of nitrate in water: effect of copper, silver, or gold addition”. In: *Journal of Catalysis* 220.1 (2003), pp. 182–191.

[98] Gregory Tate et al. “Preparation of Pt-containing bimetallic and trimetallic catalysts using continuous electroless deposition methods”. In: *Catalysis Today* 334 (2019), pp. 113–121.

[99] K D Beard et al. “Preparation of highly dispersed PEM fuel cell catalysts using electroless deposition methods”. English. In: *Applied Catalysis B-Environmental* 72.3-4 (2007), pp. 262–271.

[100] Paola Luches et al. “Nature of Ag islands and nanoparticles on the CeO2 (111) surface”. In: *The Journal of Physical Chemistry C* 116.1 (2012), pp. 1122–1132.

[101] B Coq. “Metal-Support Interaction In Catalysis”. In: *Metal-Ligand Interactions in Chemistry, Physics and Biology*. Ed. by Nino Russo and Dennis R Salahub. Dordrecht: Springer Netherlands, 2000, pp. 49–71.

[102] Matteo Farnesi Camellone et al. “Catalytic proton dynamics at the water/solid interface of ceria-supported Pt clusters”. In: *Journal of the American Chemical Society* 138.36 (2016), pp. 11560–11567.

[103] Sara E Davis, Matthew S Ide, and Robert J Davis. “Selective oxidation of alcohols and aldehydes over supported metal nanoparticles”. In: *Green Chemistry* 15.1 (2013), pp. 17–45.

[104] Michele Melchionna, Paolo Fornasiero, and Matteo Cargnello. “Chapter 1 - Opportunities and Challenges in the Synthesis, Characterization, and Catalytic Properties of Controlled Nanostructures”. In: *Studies in Surface Science and Catalysis*. Ed. by Paolo Fornasiero and Matteo Cargnello. Vol. 177. Elsevier, 2017, pp. 1–56.

[105] Yuyan Shao, Geping Yin, and Yunzhi Gao. “Understanding and approaches for the durability issues of Pt-based catalysts for PEM fuel cell”. In: *Journal of Power Sources* 171.2 (2007), pp. 558–566.

[106] Chenyu Wang and Jacob S Spendelow. “Recent Developments in Pt-Co catalysts for PEM Fuel Cells”. In: *Current Opinion in Electrochemistry* (2021), p. 100715.

[107] S J Tauster, S C Fung, and R L Garten. “Strong metal-support interactions. Group 8 noble metals supported on titanium dioxide”. In: *Journal of the American Chemical Society* 100.1 (1978), pp. 170–175.

[108] M S Chen and D W Goodman. “Interaction of Au with titania: the role of reduced Ti”. In: *Topics in Catalysis* 44.1 (2007), pp. 41–47.

[109] W J Yuan et al. “Point-Defect-Rich Carbon Sheets as the High-Activity Catalyst Toward Oxygen Reduction and Hydrogen Evolution”. English. In: *Catalysts* 9.4 (2019).

[110] Y Yang et al. “Donor/Acceptor Concepts for Developing Efficient Suzuki Cross-Coupling Catalysts Using Graphene-Supported Ni, Cu, Fe, Pd, and Bimetallic Pd/Ni Clusters”. English. In: *Journal of Physical Chemistry C* 122.44 (2018), pp. 25396–25403.

[111] Y Yang et al. “A fundamental analysis of enhanced cross-coupling catalytic activity for palladium clusters on graphene supports”. English. In: *Nanoscale* 8.47 (2016), pp. 19564–19572.

[112] Y Yang et al. “More than just a support: Graphene as a solid-state ligand for palladium-catalyzed cross-coupling reactions”. English. In: *Journal of Catalysis* 360 (2018), pp. 20–26.

[113] W J Peng et al. “A review on heavy metal ions adsorption from water by graphene oxide and its composites”. English. In: *Journal of Molecular Liquids* 230 (2017), pp. 496–504.

[114] G X Zhao et al. “Removal of Pb(II) ions from aqueous solutions on few-layered graphene oxide nanosheets”. English. In: *Dalton Transactions* 40.41 (2011), pp. 10945–10952.

[115] L S Zhang et al. “Identification of the nitrogen species on N-doped graphene layers and Pt/NG composite catalyst for direct methanol fuel cell”. English. In: *Physical Chemistry Chemical Physics* 12.38 (2010), pp. 12055–12059.

[116] Y F Deng et al. “Review on recent advances in nitrogen-doped carbons: preparations and applications in supercapacitors”. English. In: *Journal of Materials Chemistry A* 4.4 (2016), pp. 1144–1173.

[117] Zhen-Huan Sheng et al. “Catalyst-Free Synthesis of Nitrogen-Doped Graphene via Thermal Annealing Graphite Oxide with Melamine and Its Excellent Electrocatalysis”. In: *Acs Nano* 5.6 (2011), pp. 4350–4358.

[118] Li-Feng Chen et al. “Synthesis of Nitrogen-Doped Porous Carbon Nanofibers as an Efficient Electrode Material for Supercapacitors”. In: *Acs Nano* 6.8 (2012), pp. 7092–7102.

[119] Li Sun et al. “Nitrogen-doped graphene with high nitrogen level via a one-step hydrothermal reaction of graphene oxide with urea for superior capacitive energy storage”. In: *Rsc Advances* 2.10 (2012), pp. 4498–4506.

[120] Yang Zhao et al. “A Versatile, Ultralight, Nitrogen-Doped Graphene Framework”. In: *Angewandte Chemie International Edition* 51.45 (2012), pp. 11371–11375.

[121] Roshni Yadav and C K Dixit. “Synthesis, characterization and prospective applications of nitrogen-doped graphene: A short review”. In: *Journal of Science: Advanced Materials and Devices* 2.2 (2017), pp. 141–149.

[122] Dacheng Wei et al. “Synthesis of N-doped graphene by chemical vapor deposition and its electrical properties”. In: *Nano Letters* 9.5 (2009), pp. 1752–1758.

[123] Chong-an Di et al. “Patterned graphene as source/drain electrodes for bottom-contact organic field-effect transistors”. In: *Advanced Materials* 20.17 (2008), pp. 3289–3293. ISSN: 0935-9648.

[124] Ziyin Lin et al. “Facile Synthesis of Nitrogen-Doped Graphene via Pyrolysis of Graphene Oxide and Urea, and its Electrocatalytic Activity toward the Oxygen-Reduction Reaction”. In: *Advanced Energy Materials* 2.7 (2012), pp. 884–888.

[125] Yong Jae Cho et al. “Selective nitrogen-doping structure of nanosize graphitic layers”. In: *The Journal of Physical Chemistry C* 115.9 (2011), pp. 3737–3744.

[126] Mika Sillanpää, Anu Matilainen, and Tanja Lahtinen. “Chapter 2 - Characterization of NOM”. In: *Natural Organic Matter in Water*. Ed. by Mika Sillanpää. Butterworth-Heinemann, 2015, pp. 17–53.

[127] Wei Luo et al. “Pyrolysis of Cellulose under Ammonia Leads to Nitrogen-Doped Nanoporous Carbon Generated through Methane Formation”. In: *Nano Letters* 14.4 (2014), pp. 2225–2229.

[128] Gao Cheng et al. “Nitrogen-Doped Ketjenblack Carbon Supported Co3O4 Nanoparticles as a Synergistic Electrocatalyst for Oxygen Reduction Reaction”. English. In: *Frontiers in Chemistry* 7 (2019).

[129] B Ashourirad et al. “A cost-effective synthesis of heteroatom-doped porous carbons as efficient CO2 sorbents”. English. In: *Journal of Materials Chemistry A* 4.38 (2016), pp. 14693–14702.

[130] M Balat. “Potential importance of hydrogen as a future solution to environmental and transportation problems”. English. In: *International Journal of Hydrogen Energy* 33.15 (2008), pp. 4013–4029.

[131] A C Dillon et al. “Importance of turning to renewable energy resources with hydrogen as a promising candidate and on-board storage a critical barrier”. English. In: *Life-Cycle Analysis Tools for Green Materials and Process Selection* 895 (2006), pp. 115–+.

[132] J A Turner. “Sustainable hydrogen production”. English. In: *Science* 305.5686 (2004), pp. 972–974.

[133] I P Jain. “Hydrogen the fuel for 21st century”. English. In: *International Journal of Hydrogen Energy* 34.17 (2009), pp. 7368–7378.

[134] N Negurescu et al. “Performance Comparison between Hydrogen and Gasoline Fuelled Spark Ignition Engine”. English. In: *Thermal Science* 15.4 (2011), pp. 1155–1164.

[135] I E A. *Global hydrogen production in the Sustainable Development Scenario, 2019-2070*. Paris, 2020.

[136] Richa Kothari, D Buddhi, and R L Sawhney. “Comparison of environmental and economic aspects of various hydrogen production methods”. In: *Renewable and Sustainable Energy Reviews* 12.2 (2008), pp. 553–563.

[137] V K Budama et al. “Thermodynamic development and design of a concentrating solar thermochemical water-splitting process for co-production of hydrogen and electricity”. English. In: *International Journal of Hydrogen Energy* 43.37 (2018), pp. 17574–17587.

[138] Z Wang et al. “Comparison of thermochemical, electrolytic, photoelectrolytic and photochemical solar-to-hydrogen production technologies”. English. In: *International Journal of Hydrogen Energy* 37.21 (2012), pp. 16287–16301.

[139] A S M Nur et al. “Catalytic SO3 Decomposition Activity and Stability of Pt Supported on Anatase TiO2 for Solar Thermochemical Water-Splitting Cycles”. In: *ACS Omega* 2.10 (2017), pp. 7057–7065.

[140] Christian Sattler et al. “Solar hydrogen production via sulphur based thermochemical water-splitting”. In: *Solar Energy* 156 (2017), pp. 30–47.

[141] D R Okeefe, J H Norman, and D G Williamson. “Catalysis Research in Thermochemical Water-Splitting Processes”. English. In: *Catalysis Reviews-Science and Engineering* 22.3 (1980), pp. 325–369.

[142] J H Norman et al. “Studies of the Sulfur-Iodine Thermochemical Water-Splitting Cycle”. English. In: *International Journal of Hydrogen Energy* 7.7 (1982), pp. 545–556. URL: %3CGo%20to%20ISI%3E://WOS:A1982NS71200002.

[143] H Tagawa and T Endo. “Catalytic Decomposition of Sulfuric-Acid Using Metal-Oxides as the Oxygen Generating Reaction in Thermochemical Water Splitting Process”. English. In: *International Journal of Hydrogen Energy* 14.1 (1989), pp. 11–17.

[144] Lloyd Brown, Paul Trester, and Gottfried Besenbruch. *High-Pressure Catalytic Metal Reactor in a Simulated Solar Central Receiver*. 1986.

[145] L M Petkovic et al. “Pt/TiO2 (rutile) catalysts for sulfuric acid decomposition in sulfur-based thermochemical water-splitting cycles”. English. In: *Applied Catalysis a-General* 338.1-2 (2008), pp. 27–36.

[146] Lucia Petkovic et al. “Catalyst Activity and Post-operation Analyses of Pt/TiO2 (Rutile) Catalysts Used in the Sulfuric Acid Decomposition Reaction”. In: (2007).

[147] D M Ginosar et al. “Stability of supported platinum sulfuric acid decomposition catalysts for use in thermochemical water splitting cycles”. English. In: *International Journal of Hydrogen Energy* 32.4 (2007), pp. 482–488.

[148] D M Ginosar et al. “High-temperature sulfuric acid decomposition over complex metal oxide catalysts”. English. In: *International Journal of Hydrogen Energy* 34.9 (2009), pp. 4065–4073.

[149] Z Ma and S Dai. “Stabilizing Gold Nanoparticles by Solid Supports”. English. In: *Heterogeneous Gold Catalysts and Catalysis* 18 (2014), pp. 1–26.

[150] D A H Hanaor and C C Sorrell. “Review of the anatase to rutile phase transformation”. English. In: *Journal of Materials Science* 46.4 (2011), pp. 855–874.

[151] J Yin et al. “Boron Nitride Nanostructures: Fabrication, Functionalization and Applications”. English. In: *Small* 12.22 (2016), pp. 2942–2968.

[152] M Hubacek et al. “High-temperature behaviour of hexagonal boron nitride”. English. In: *Thermochimica Acta* 283 (1996), pp. 359–367.

[153] L J Gao et al. “Enhanced Nickel-Catalyzed Methanation Confined under Hexagonal Boron Nitride Shells”. English. In: *ACS Catalysis* 6.10 (2016), pp. 6814–6822.

[154] N Meyer et al. “Boron nitride as an alternative support of Pd catalysts for the selective oxidation of lactose”. English. In: *Catalysis Communications* 29 (2012), pp. 170–174.

[155] G Postole et al. “Boron nitride: A high potential support for combustion catalysts”. English. In: *Thermochimica Acta* 434.1-2 (2005), pp. 150–157.

[156] J C S Wu, C Y Chen, and S D Lin. “Boron nitride supported Pt catalyst for selective hydrogenation”. English. In: *Catalysis Letters* 102.3-4 (2005), pp. 223–227.

[157] W S Zhu et al. “Taming interfacial electronic properties of platinum nanoparticles on vacancy-abundant boron nitride nanosheets for enhanced catalysis”. English. In: *Nature Communications* 8 (2017).

[158] M Parizad et al. “Stabilization of Catalytic Surfaces through Core–Shell Structures: Ag–Ir/Al2O3 Case Study”. In: *ACS Catalysis* 10.22 (2020), pp. 13352–13363.

[159] Z W Li, Z G Wang, and S Kawi. “Sintering and Coke Resistant Core/Yolk Shell Catalyst for Hydrocarbon Reforming”. English. In: *Chemcatchem* 11.1 (2019), pp. 202–224.

[160] Z F Bian et al. “A Review on Bimetallic Nickel-Based Catalysts for CO2 Reforming of Methane”. English. In: *Chemphyschem* 18.22 (2017), pp. 3117–3134.

[161] K An et al. “High-Temperature Catalytic Reforming of n-Hexane over Supported and Core-Shell Pt Nanoparticle Catalysts: Role of Oxide-Metal Interface and Thermal Stability”. English. In: *Nano Letters* 14.8 (2014), pp. 4907–4912.

[162] S H Joo et al. “Thermally stable Pt/mesoporous silica core-shell nanocatalysts for high-temperature reactions”. English. In: *Nature Materials* 8.2 (2009), pp. 126–131.

[163] M Ohashi et al. “Electrochemical and structural characterization of carbon-supported Pt-Pd bimetallic electrocatalysts prepared by electroless deposition”. English. In: *Electrochimica Acta* 55.24 (2010), pp. 7376–7384.

[164] K D Beard, J W Van Zee, and J R Monnier. “Preparation of carbon-supported Pt-Pd electrocatalysts with improved physical properties using electroless deposition methods”. English. In: *Applied Catalysis B-Environmental* 88.1-2 (2009), pp. 185–193.

[165] K D Beard et al. “Preparation and Structural Analysis of Carbon-Supported Co Core/Pt Shell Electrocatalysts Using Electroless Deposition Methods”. English. In: *Acs Nano* 3.9 (2009), pp. 2841–2853.

[166] Liancheng Wang et al. “A general route for the convenient synthesis of crystalline hexagonal boron nitride micromesh at mild temperature”. In: *Journal of Materials Chemistry* 19.14 (2009), pp. 1989–1994.

[167] M J Uddin et al. “Surface Structure and Phase Composition of TiO(2)P25 Particles After Thermal Treatments and HF Etching”. English. In: *Frontiers in Materials* 7 (2020).

[168] Nicholas T Nolan, Michael K Seery, and Suresh C Pillai. “Spectroscopic Investigation of the Anatase-to-Rutile Transformation of SolGel-Synthesized TiO2 Photocatalysts”. In: *The Journal of Physical Chemistry C* 113.36 (2009), pp. 16151–16157.

[169] J S Ma, M C Wen, and C H Lu. “Reaction mechanism and kinetics analysis of the phase transformation of TiO2 from the anatase phase to the rutile phase”. English. In: *Journal of Materials Science-Materials in Electronics* 24.7 (2013), pp. 2506–2512.

[170] H Kominami et al. “Novel synthesis of microcrystalline titanium(IV) oxide having high thermal stability and ultra-high photocatalytic activity: thermal decomposition of titanium(IV) alkoxide in organic solvents”. In: *Catalysis Letters* 46.3 (1997), pp. 235–240.

[171] Lu Hua Li et al. “Strong Oxidation Resistance of Atomically Thin Boron Nitride Nanosheets”. In: *Acs Nano* 8.2 (2014), pp. 1457–1462.

[172] Kamyar Keyvanloo et al. “Effect of Support Pretreatment Temperature on the Performance of an Iron Fischer–Tropsch Catalyst Supported on Silica-Stabilized Alumina”. In: *Catalysts* 8.2 (2018).

[173] K O'Connell and J R Regalbuto. "High Sensitivity Silicon Slit Detectors for 1 nm Powder XRD Size Detection Limit". English. In: *Catalysis Letters* 145.3 (2015), pp. 777–783.

[174] L Z Mezey and J Giber. "The Surface Free Energies of Solid Chemical Elements: Calculation from Internal Free Enthalpies of Atomization". In: *Japanese Journal of Applied Physics* 21.Part 1, No. 11 (1982), pp. 1569–1571.

[175] I J McPherson et al. "Electrochemical CO Oxidation at Platinum on Carbon Studied through Analysis of Anomalous in Situ IR Spectra". English. In: *Journal of Physical Chemistry C* 121.32 (2017), pp. 17176–17187.

[176] L C Ordonez et al. "CO oxidation on carbon-supported PtMo electrocatalysts: Effect of the platinum particle size". English. In: *International Journal of Hydrogen Energy* 32.15 (2007), pp. 3147–3153.

[177] B N Grgur, N M Markovic, and P N Ross. "Electrochemical oxidation of carbon monoxide: from platinum single crystals to low temperature fuel catalysts. Part II: Electrooxidation of H-2, CO and H-2/CO mixtures on well characterized PtMo alloy". English. In: *Journal of the Serbian Chemical Society* 68.3 (2003), pp. 191–205.

[178] R W Yan et al. "Preparation of platinum/polyaniline/multi-walled carbon nanotube nanocomposite with sugarcoated haws structure for electrocatalytic oxidation of methanol". English. In: *Synthetic Metals* 250 (2019), pp. 146–151.

[179] R Sha, S S Jones, and S Badhulika. "Controlled synthesis of platinum nanoflowers supported on carbon quantum dots as a highly effective catalyst for methanol electro-oxidation". English. In: *Surface & Coatings Technology* 360 (2019), pp. 400–408.

[180] J Polasek et al. “Methanol oxidation on pure and platinum-doped tungsten oxide supported by activated carbon”. English. In: *Materials Chemistry and Physics* 228 (2019), pp. 147–159.

[181] Z H Su et al. “Enhanced electrocatalytic performance of platinum nanoparticles on thiolated polyaniline-multiwalled carbon nanotubes for methanol oxidation”. English. In: *Rsc Advances* 8.59 (2018), pp. 33742–33747.

[182] D Pan, X W Li, and A F Zhang. “Platinum assisted by carbon quantum dots for methanol electro-oxidation”. English. In: *Applied Surface Science* 427 (2018), pp. 715–723.

[183] J R Gallagher et al. “In situ diffraction of highly dispersed supported platinum nanoparticles”. English. In: *Catalysis Science & Technology* 4.9 (2014), pp. 3053–3063.

[184] Ritubarna Banerjee et al. “Detection of Ambient Oxidation of Ultrasmall Supported Platinum Nanoparticles with Benchtop Powder X-Ray Diffraction”. In: *Catalysis Letters* 147.7 (2017), pp. 1754–1764.

[185] R Banerjee et al. “Electrostatic Adsorption of Platinum onto Carbon Nanotubes and Nanofibers for Nanoparticle Synthesis”. English. In: *C-Journal of Carbon Research* 4.1 (2018).

[186] R Adams and R L Shriner. “Platinum oxide as a catalyst in the reduction of organic compounds III Preparation and properties of the oxide of platinum obtained by the fusion of ceiloroplatinic acid with sodium nitrate”. English. In: *Journal of the American Chemical Society* 45 (1923), pp. 2171–2179.

[187] L Olsson and E Fridell. “The influence of Pt oxide formation and Pt dispersion on the reactions NO2 <-> NO+1/2 O-2 over Pt/Al2O3 and Pt/BaO/Al2O3”. English. In: *Journal of Catalysis* 210.2 (2002), pp. 340–353.

[188] J F Sauvage, R H Baker, and A S Hussey. “The Hydrogenation of Cyclohexenes over Platinum Oxide”. English. In: *Journal of the American Chemical Society* 82.23 (1960), pp. 6090–6095.

[189] G A El-Nagar et al. “Efficient Direct Formic Acid Fuel Cells (DFAFCs) Anode Derived from Seafood waste: Migration Mechanism”. English. In: *Scientific Reports* 7 (2017).

[190] J M H Dirkx and H S Vanderbaan. “The Oxidation of Glucose with Platinum on Carbon as Catalyst”. English. In: *Journal of Catalysis* 67.1 (1981), pp. 1–13.

[191] A P Markusse et al. “Platinum deactivation: in situ EXAFS during aqueous alcohol oxidation reaction”. English. In: *Catalysis Letters* 55.3-4 (1998), pp. 141–145.

[192] C E Carlton et al. “Sub-Nanometer-Resolution Elemental Mapping of "Pt3Co" Nanoparticle Catalyst Degradation in Proton-Exchange Membrane Fuel Cells”. English. In: *Journal of Physical Chemistry Letters* 3.2 (2012), pp. 161–166.

[193] C P O’Brien et al. “Deactivation of Pt/Al2O3 during propane oxidation at low temperatures: Kinetic regimes and platinum oxide formation”. English. In: *Journal of Catalysis* 337 (2016), pp. 122–132.

[194] K Hauff et al. “Platinum oxide formation and reduction during NO oxidation on a diesel oxidation catalyst - Experimental results”. English. In: *Applied Catalysis B-Environmental* 123 (2012), pp. 107–116.

[195] Ritubarna Banerjee et al. “Ambient Oxidation of Ultrasmall Platinum Nanoparticles on Microporous Carbon Catalyst Supports”. In: *ACS Applied Nano Materials* 1.10 (2018), pp. 5876–5884.

[196] S Chu and A Majumdar. "Opportunities and challenges for a sustainable energy future". English. In: *Nature* 488.7411 (2012), pp. 294–303. ISSN: 0028-0836. DOI: 10.1038/nature11475. URL: %3CGo%20to%20ISI%3E://WOS:000307501000028.

[197] C H Bartholomew. "Mechanisms of catalyst deactivation". English. In: *Applied Catalysis a-General* 212.1-2 (2001), pp. 17–60.

[198] P Forzatti and L Lietti. "Catalyst deactivation". English. In: *Catalysis Today* 52.2-3 (1999), pp. 165–181.

[199] S Lee, J Seo, and W Jung. "Sintering-resistant Pt@CeO2 nanoparticles for high-temperature oxidation catalysis". English. In: *Nanoscale* 8.19 (2016), pp. 10219–10228.

[200] R T Lv et al. "Open-Ended, N-Doped Carbon Nanotube-Graphene Hybrid Nanostructures as High-Performance Catalyst Support". English. In: *Advanced Functional Materials* 21.5 (2011), pp. 999–1006.

[201] R Arrigo et al. "Nature of the N-Pd Interaction in Nitrogen-Doped Carbon Nanotube Catalysts". English. In: *ACS Catalysis* 5.5 (2015), pp. 2740–2753.

[202] J Melke et al. "Metal-Support Interactions of Platinum Nanoparticles Decorated N-Doped Carbon Nanofibers for the Oxygen Reduction Reaction". English. In: *Acs Applied Materials & Interfaces* 8.1 (2016), pp. 82–90.

[203] W Shi et al. "Enhanced Stability of Immobilized Platinum Nanoparticles through Nitrogen Heteroatoms on Doped Carbon Supports". English. In: *Chemistry of Materials* 29.20 (2017), pp. 8670–8678.

[204] J W Ma et al. "Electronic interaction between platinum nanoparticles and nitrogen-doped reduced graphene oxide: effect on the oxygen reduction reaction". English. In: *Journal of Materials Chemistry A* 3.22 (2015), pp. 11891–11904.

[205] O Podyacheva et al. “Nitrogen Doped Carbon Nanotubes and Nanofibers for Green Hydrogen Production: Similarities in the Nature of Nitrogen Species, Metal-Nitrogen Interaction, and Catalytic Properties”. English. In: *Energies* 12.20 (2019).

[206] G F Long et al. “Pt/CN-doped electrocatalysts: Superior electrocatalytic activity for methanol oxidation reaction and mechanistic insight into interfacial enhancement”. English. In: *Applied Catalysis B-Environmental* 203 (2017), pp. 541–548.

[207] M S Contreras et al. “A comparison of physical activation of carbon xerogels with carbon dioxide with chemical activation using hydroxides”. English. In: *Carbon* 48.11 (2010), pp. 3157–3168.

[208] X Hao, S Barnes, and J R Regalbuto. “A fundamental study of Pt impregnation of carbon: Adsorption equilibrium and particle synthesis”. In: *Journal of Catalysis* 279.1 (2011), pp. 48–65.

[209] S Eskandari et al. “Pushing the limits of electrostatic adsorption: charge enhanced dry impregnation of SBA-15”. English. In: *Catalysis Today* 338 (2019), pp. 60–71.

[210] S Eskandari et al. “Nanoparticle Synthesis via Electrostatic Adsorption Using Incipient Wetness Impregnation”. English. In: *ACS Catalysis* 8.11 (2018), pp. 10383–10391.

[211] V Gnutzmann and W Vogel. “Surface Oxidation and Reduction of Small Platinum Particles Observed by Insitu X-Ray-Diffraction”. English. In: *Zeitschrift Fur Physik D-Atoms Molecules and Clusters* 12.1-4 (1989), pp. 597–600.

[212] J Liu et al. “High performance platinum single atom electrocatalyst for oxygen reduction reaction”. English. In: *Nature Communications* 8 (2017).

[213] G Wu and P Zelenay. “Nanostructured Nonprecious Metal Catalysts for Oxygen Reduction Reaction”. English. In: *Accounts of Chemical Research* 46.8 (2013), pp. 1878–1889.

[214] K Jukk et al. “Platinum Nanoparticles Supported on Nitrogen-Doped Graphene Nanosheets as Electrocatalysts for Oxygen Reduction Reaction”. English. In: *Electrocatalysis* 7.5 (2016), pp. 428–440.

[215] F B Su et al. “Pt Nanoparticles Supported on Nitrogen-Doped Porous Carbon Nanospheres as an Electrocatalyst for Fuel Cells”. English. In: *Chemistry of Materials* 22.3 (2010), pp. 832–839.

[216] H R Colon-Mercado and B N Popov. “Stability of platinum based alloy cathode catalysts in PEM fuel cells”. English. In: *Journal of Power Sources* 155.2 (2006), pp. 253–263.

[217] Y Y Shao et al. “Proton exchange membrane fuel cell from low temperature to high temperature: Material challenges”. English. In: *Journal of Power Sources* 167.2 (2007), pp. 235–242.

[218] H A Gasteiger and M F Mathias. “Fundamental research and development challenges in polymer electrolyte fuel cell technology”. English. In: *Proton Conducting Membrane Fuel Cells III, Proceedings* 2002.31 (2005), pp. 1–24.

[219] X R Zhu et al. “Charge-Enhanced Dry Impregnation: A Simple Way to Improve the Preparation of Supported Metal Catalysts”. English. In: *ACS Catalysis* 3.4 (2013), pp. 625–630.

[220] Woo-Jae Lee et al. “Synthesis of highly dispersed Pt nanoparticles into carbon supports by fluidized bed reactor atomic layer deposition to boost PEMFC performance”. In: *Npg Asia Materials* 12.1 (2020), p. 40.

[221] Olga A Baturina, Steven R Aubuchon, and Kenneth J Wynne. “Thermal Stability in Air of Pt/C Catalysts and PEM Fuel Cell Catalyst Layers”. In: *Chemistry of Materials* 18.6 (2006), pp. 1498–1504.

[222] Jun Young Kim et al. “Highly durable electrocatalyst with graphitized carbon supports modified by diazonium reaction for polymer electrolyte membrane fuel cell”. In: *Carbon* 77 (2014), pp. 525–537.

[223] Jiejing Zhang et al. “The effect of Pt/C agglomerates in electrode on PEMFC performance using 3D micro-structure lattice models”. In: *International Journal of Hydrogen Energy* 42.17 (2017), pp. 12559–12566.

[224] K Hengge et al. “Accelerated fuel cell tests of anodic Pt/Ru catalyst via identical location TEM: New aspects of degradation behavior”. English. In: *International Journal of Hydrogen Energy* 42.40 (2017), pp. 25359–25371.

[225] Lei Zhang et al. “Rational design of porous structures via molecular layer deposition as an effective stabilizer for enhancing Pt ORR performance”. In: *Nano Energy* 60 (2019), pp. 111–118.

[226] Ambrož Kregar and Tomaž Katrašnik. “Theoretical analysis of particle size re-distribution due to Ostwald ripening in the fuel cell catalyst layer”. In: *Open Physics* 17.1 (2019), pp. 779–789.

[227] A Baldan. “Review Progress in Ostwald ripening theories and their applications to the γ-precipitates in nickel-base superalloys Part II Nickel-base superalloys”. In: *Journal of Materials Science* 37.12 (2002), pp. 2379–2405.

[228] Steven G Rinaldo et al. “Theoretical analysis of electrochemical surface-area loss in supported nanoparticle catalysts”. In: *Physical Chemistry Chemical Physics* 16.48 (2014), pp. 26876–26886.

[229] F A de Bruijn, V A T Dam, and G J M Janssen. “Review: Durability and Degradation Issues of PEM Fuel Cell Components”. In: *Fuel Cells* 8.1 (2008), pp. 3–22.

[230] Jutae Kim, Junhee Lee, and Yongsug Tak. “Relationship between carbon corrosion and positive electrode potential in a proton-exchange membrane fuel cell during start/stop operation”. In: *Journal of Power Sources* 192.2 (2009), pp. 674–678.

[231] Stefan Kreitmeier, Alexander Wokaun, and Felix N Büchi. “Local catalyst support degradation during polymer electrolyte fuel cell start-up and shutdown”. In: *Journal of the Electrochemical Society* 159.11 (2012), F787.

[232] Nicolas Linse et al. “Quantitative analysis of carbon corrosion during fuel cell start-up and shut-down by anode purging”. In: *Journal of Power Sources* 219 (2012), pp. 240–248.

[233] Hyung-Suk Oh, Jin-Hee Lee, and Hansung Kim. “Electrochemical carbon corrosion in high temperature proton exchange membrane fuel cells”. In: *International Journal of Hydrogen Energy* 37.14 (2012), pp. 10844–10849.

[234] L M Roen, C H Paik, and T D Jarvi. “Electrocatalytic corrosion of carbon support in PEMFC cathodes”. In: *Electrochemical and Solid State Letters* 7.1 (2003), A19.

[235] Madhusudhana R Dowlapalli et al. “Electrochemical Oxidation Resistance of Carbonaceous Materials”. In: *ECS Transactions* 1.8 (2019), pp. 41–50.

[236] Carl A Reiser et al. “A reverse-current decay mechanism for fuel cells”. In: *Electrochemical and Solid State Letters* 8.6 (2005), A273.

[237] D A Stevens et al. “Ex Situ and In Situ Stability Studies of PEMFC Catalysts”. In: *Journal of the Electrochemical Society* 152.12 (2005), A2309.

[238] Y Shao. “Investigation on the stability of Pt/carbon nanotube catalysts and novel methods for the preparation of the electrodes for PEMFC”. PhD thesis. 2006.

[239] Reyimjan A Sidik et al. “O2 Reduction on Graphite and Nitrogen-Doped Graphite: Experiment and Theory”. In: *The Journal of Physical Chemistry B* 110.4 (2006), pp. 1787–1793.

[240] F Coloma, A Sepulvedaescribano, and F Rodriguezreinoso. “Heat-Treated Carbon-Blacks as Supports for Platinum Catalysts”. In: *Journal of Catalysis* 154.2 (1995), pp. 299–305.

[241] Feng Zhang et al. “Ultralow Pt Doped on N-based Carbon as a Promising Electrocatalyst for High-Temperature Proton Exchange Membrane Fuel Cells”. In: *Acs Applied Energy Materials* 4.9 (2021), pp. 9881–9890.

[242] Q O Xue et al. “Enhanced PEMFC durability with graphitized carbon black cathode catalyst supports under accelerated stress testing”. English. In: *Rsc Advances* 11.32 (2021), pp. 19417–19425.

[243] Stéphanie Lambert et al. “Synthesis of very highly dispersed platinum catalysts supported on carbon xerogels by the strong electrostatic adsorption method”. In: *Journal of Catalysis* 261.1 (2009), pp. 23–33.

[244] Wen Xiong et al. “Enhanced Performance of Oxygen-Functionalized Multiwalled Carbon Nanotubes as Support for Pt and Pt–Ru Bimetallic Catalysts for Methanol Electrooxidation”. In: *Acs Applied Energy Materials* 3.6 (2020), pp. 5487–5496.

[245] N Job et al. “Efficient Pt/carbon electrocatalysts for proton exchange membrane fuel cells: Avoid chloride-based Pt salts!” English. In: *Journal of Power Sources* 240 (2013), pp. 294–305.

[246] N Job et al. “Carbon xerogels as catalyst supports for PEM fuel cell cathode”. English. In: *Energy Conversion and Management* 49.9 (2008), pp. 2461–2470.

[247] Ling Jiao and John R Regalbuto. “The synthesis of highly dispersed noble and base metals on silica via strong electrostatic adsorption: I. Amorphous silica”. In: *Journal of Catalysis* 260.2 (2008), pp. 329–341.

[248] Nathalie Job et al. “Highly dispersed platinum catalysts prepared by impregnation of texture-tailored carbon xerogels”. In: *Journal of Catalysis* 240.2 (2006), pp. 160–171.

[249] N Job et al. “Preparation of highly loaded Pt/carbon xerogel catalysts for Proton Exchange Membrane fuel cells by the Strong Electrostatic Adsorption method”. English. In: *Catalysis Today* 150.1-2 (2010), pp. 119–127.

[250] Farid Bensebaa. “Chapter 2 - Wet Production Methods”. In: *Interface Science and Technology*. Ed. by Farid Bensebaa. Vol. 19. Elsevier, 2013, pp. 85–146.

[251] Younan Xia, Xiaohu Xia, and Hsin-Chieh Peng. “Shape-Controlled Synthesis of Colloidal Metal Nanocrystals: Thermodynamic versus Kinetic Products”. In: *Journal of the American Chemical Society* 137.25 (2015), pp. 7947–7966.

[252] C J Zhong and J R Regalbuto. “7.04 - Metal Nanoparticle Synthesis”. In: *Comprehensive Inorganic Chemistry II (Second Edition)*. Ed. by Jan Reedijk and Kenneth Poeppelmeier. Amsterdam: Elsevier, 2013, pp. 75–102.

[253] Jadid E Samad, Jayson Keels, and John R Regalbuto. “A Comparison of Pt(II) and Pt(IV) Chloride Precursors for Strong Electrostatic Adsorption Synthesis of Pt/Alumina and Pt/Carbon Catalysts”. In: *Catalysis Letters* 146.1 (2016), pp. 157–162.

[254] Zhi Qiao et al. “Atomically dispersed single iron sites for promoting Pt and Pt3Co fuel cell catalysts: performance and durability improvements”. In: *Energy & Environmental Science* 14.9 (2021), pp. 4948–4960.

[255] H Chen et al. “Sinter-Resistant Nanoparticle Catalysts Achieved by 2D Boron Nitride-Based Strong Metal-Support Interactions: A New Twist on an Old Story”. English. In: *ACS Central Science* 6.9 (2020), pp. 1617–1627.

[256] Nathalie Job et al. “Design of Pt/Carbon Xerogel Catalysts for PEM Fuel Cells”. In: *Catalysts* 5.1 (2015), pp. 40–57.

[257] Xizheng Fan and Qingqing Pang. “Strong Electrostatic Adsorption Strategy to Enhance Interaction Between Ultra-Small Ru Nanoparticles and Carbon for High-Efficient Electrocatalyst Toward HER in Acidic and Alkaline Media”. In: *Chemelectrochem* 8.23 (2021), pp. 4472–4479.

[258] Amod Kumar and Vijay Ramani. “Strong Metal–Support Interactions Enhance the Activity and Durability of Platinum Supported on Tantalum-Modified Titanium Dioxide Electrocatalysts”. In: *ACS Catalysis* 4.5 (2014), pp. 1516–1525.

[259] A Gamez et al. “Oxygen reduction on well-defined platinum nanoparticles inside recast ionomer”. In: *Electrochimica Acta* 41.2 (1996), pp. 307–314.

[260] Patricia Gon Corradini et al. “Effect of the relationship between particle size, inter-particle distance, and metal loading of carbon supported fuel cell catalysts on their catalytic activity”. In: *Journal of Nanoparticle Research* 14.9 (2012), p. 1080.

[261] I C Gerber and P Serp. “A Theory/Experience Description of Support Effects in Carbon-Supported Catalysts”. English. In: *Chemical Reviews* 120.2 (2020), pp. 1250–1349.

[262] Keiko Miyabayashi and Mikio Miyake. “Metal–Support Interactions of Platinum Nanoparticles Modified with Pyrene-functionalized Alkylamine and Improved Electrocatalytic Activity of Oxygen Reduction Reaction”. In: *Chemistry Letters* 46.5 (2017), pp. 707–710.

[263] Jason R Croy et al. “Size Dependent Study of MeOH Decomposition Over Size-selected Pt Nanoparticles Synthesized via Micelle Encapsulation”. In: *Catalysis Letters* 118.1 (2007), pp. 1–7.

[264] S Garbarino et al. “Effect of Size on the Electrochemical Stability of Pt Nanoparticles Deposited on Gold Substrate”. In: *The Journal of Physical Chemistry C* 114.7 (2010), pp. 2980–2988.

[265] Ignacio Lopez-Salido et al. “Electronic and Geometric Properties of Au Nanoparticles on Highly Ordered Pyrolytic Graphite (HOPG) Studied Using X-ray Photoelectron Spectroscopy (XPS) and Scanning Tunneling Microscopy (STM)”. In: *The Journal of Physical Chemistry B* 110.3 (2006), pp. 1128–1136.

Appendix A

Supplementary information for Chapter 2

Table A.1 Estimated XRD particle sizes using Sherrer's equation

Catalyst	Supported on TiO_2 [nm]					Supported on BN [nm]				
	Fresh		Calcined			Fresh		Calcined		
	Pt	Ir	Pt	Ir	IrO_2	Pt	Ir	Pt	Ir	IrO_2
1%Pt	11.6	-	33.5	-	-	**	-	13.2	-	-
1%Ir	-	-	-	**	-	-	**	-	**	**
5%Ir	-	4.6	-	9.1	10.4	-	2.5	-	6.0	6.6
7.5%Ir	-	5.0	-	10.1	11.1	-	3.2	-	6.2	6.6
10%Ir	-	5.4	-	10.6	11.1	***	***	***	***	***
1%Pt-1%Ir	-	-	27.6	-	-	***	***	***	***	***
1%Pt-5%Ir	-	4.7	24.5	-	-	-	2.8	13.6	-	14.7
1%Pt-7.5%Ir	-	5.6	22.1	-	11.0	-	3.2	15.2	-	22.1
1%Pt-10%Ir	-	5.9	21.0	-	9.0	***	***	***	***	***

Appendix B

Supplementary information for Chapter 3

B.1 XRD Analysis

The in-situ XRD patterns obtained for both oxidation and heat-treatment studies were compared to the reference spectra using PDXL software (version 2.0, Rigaku corporation). To deconvolute metal and oxide peaks, the XRD pattern for the support was subtracted from the sample XRD patterns using Fityk software (version 1.3.1). The positions and relative intensity of the Pt (111) and (200) peaks were taken from the powder diffraction files (JCPDS 00-004-0802) and fits were obtained with Gaussian peak asymmetry. The XRD particle size was determined by utilizing the Scherrer equation with an input of the full-width at half maximum (FWHM) [173] and a shape factor of 0.94. The FWHM employed was that value which minimized the sum of squared error of the fit to the background-subtracted patterns. Minima in the sum of squared error for the Pt/NC, 6.5%Pt/C and 12.1%Pt/C samples are seen in Figure B.1f, l, and r. A similar approach was taken to optimize fits of the oxidized samples. This is shown in Figure B.2 for the Pt/NC and all three Pt/C series. To obtain the best fits with the minimal number of oxide phases, a first attempt was made to fit the patterns with only the metallic phase (left-most column of Figure B.2) followed by fits with Pt metal and Pt_3O_4 (center column of the figure) and finally with Pt, Pt_3O_4, and PtO_2. The latter peaks were retained only when the sum of squares of the error was significantly diminished.

The average sizes of Pt phases determined from XRD are summarized in Table

B.1. The STEM-derived, volume-averaged size for the room-temperature Pt/NC sample is 1.2 nm, which is between the XRD size of the Pt^0 phase (0.98 nm) and the Pt^0 + Pt_3O_4 phases (0.98 + 0.73 = 1.7 nm). This is reasonable since the oxidized particles are not all core-shell; the smallest particles are completely oxidized [184]. The STEM-derived size of the 18.9%Pt/C sample, at 1.8 nm is similarly larger than the Pt_0 phase but smaller than Pt^0 + Pt oxide phases.

Table B.1 The average size of Pt-NPs after oxidation at 25 °C and 300 °C

Catalyst	Oxidation temperature [°C]	Pt^0 [nm]	Pt_3O_4 [nm]	PtO_2 [nm]
12.5% Pt/NC STEM D_v=1.2 nm	25	0.98	0.73	-
	50	0.87	0.73	-
	75	0.98	0.78	-
	100	0.98	0.83	0.97
	150	0.98	0.83	0.97
	200	0.98	0.90	0.97
	250	0.98	0.96	0.97
	300	0.98	0.96	0.97
18.9% Pt/C STEM D_v=1.8 nm	25	1.58	0.66	0.70
	50	1.61	0.66	0.70
	75	1.61	0.66	0.70
	100	1.64	0.70	0.70
	150	1.64	0.73	0.70
	200	1.64	0.72	0.73
	250	1.77	0.72	0.79
	300	1.77	0.72	0.73
12.1% Pt/C	25	1.38	0.66	0.66
	50	1.42	0.66	0.72
	75	1.42	0.66	0.72
	100	1.47	0.66	0.72
	150	1.47	0.69	0.72
	200	1.47	0.69	0.79
	250	1.47	0.69	0.79
	300	1.58	0.73	0.79
6.5% Pt/C	25	0.98	0.66	0.72
	50	0.98	0.66	0.72
	75	0.98	0.66	0.72
	100	0.98	0.66	0.72
	150	0.98	0.66	0.78
	200	0.98	0.71	0.78
	250	0.98	0.71	0.78
	300	0.98	0.77	0.84

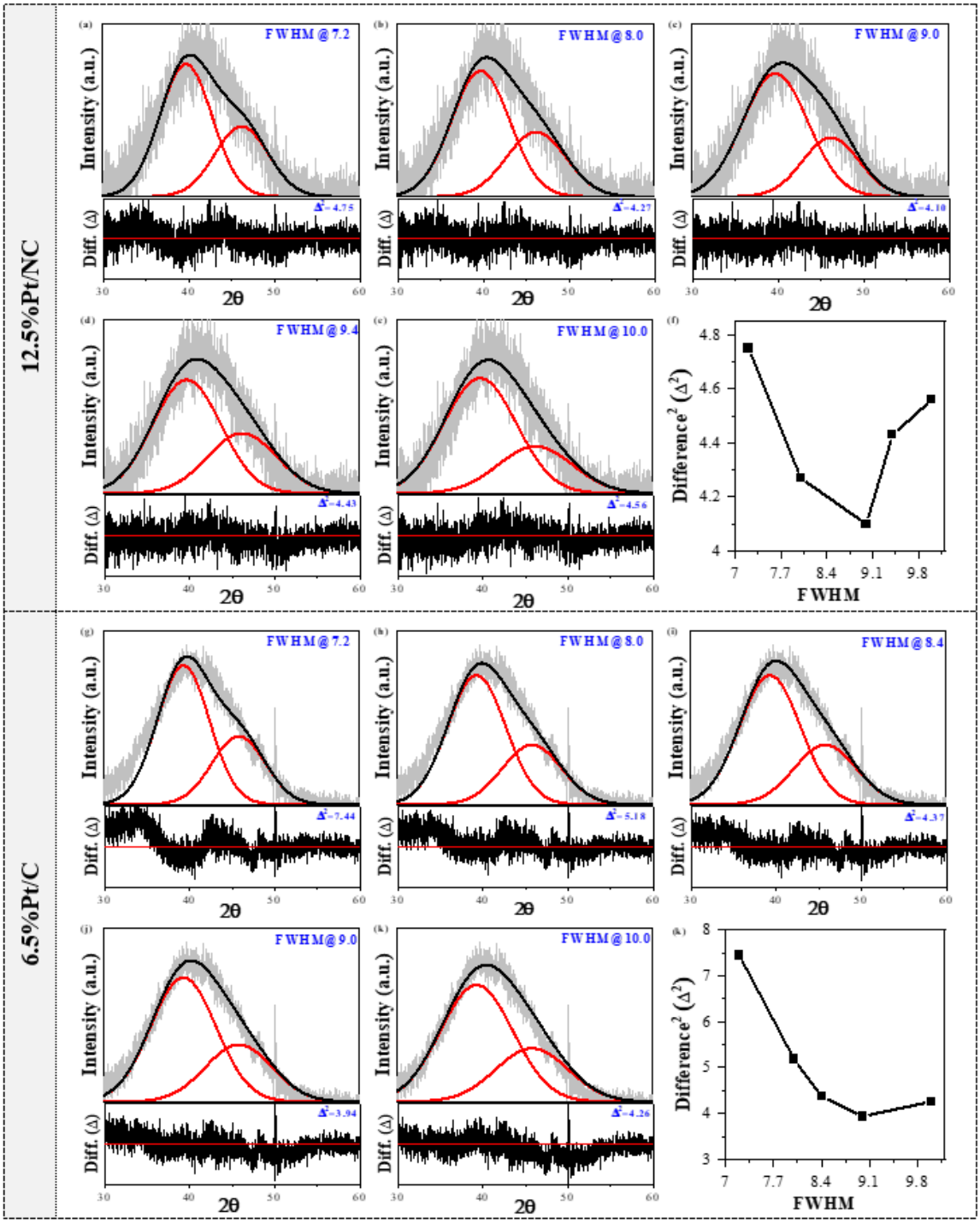
12.5%Pt/NC
6.5%Pt/C
FWHM@7.2
FWHM@8.0
FWHM@9.0
FWHM@9.4
FWHM@10.0
FWHM@8.4
Intensity (a.u.)
Diff. (Δ)
2θ
Difference² (Δ²)
FWHM

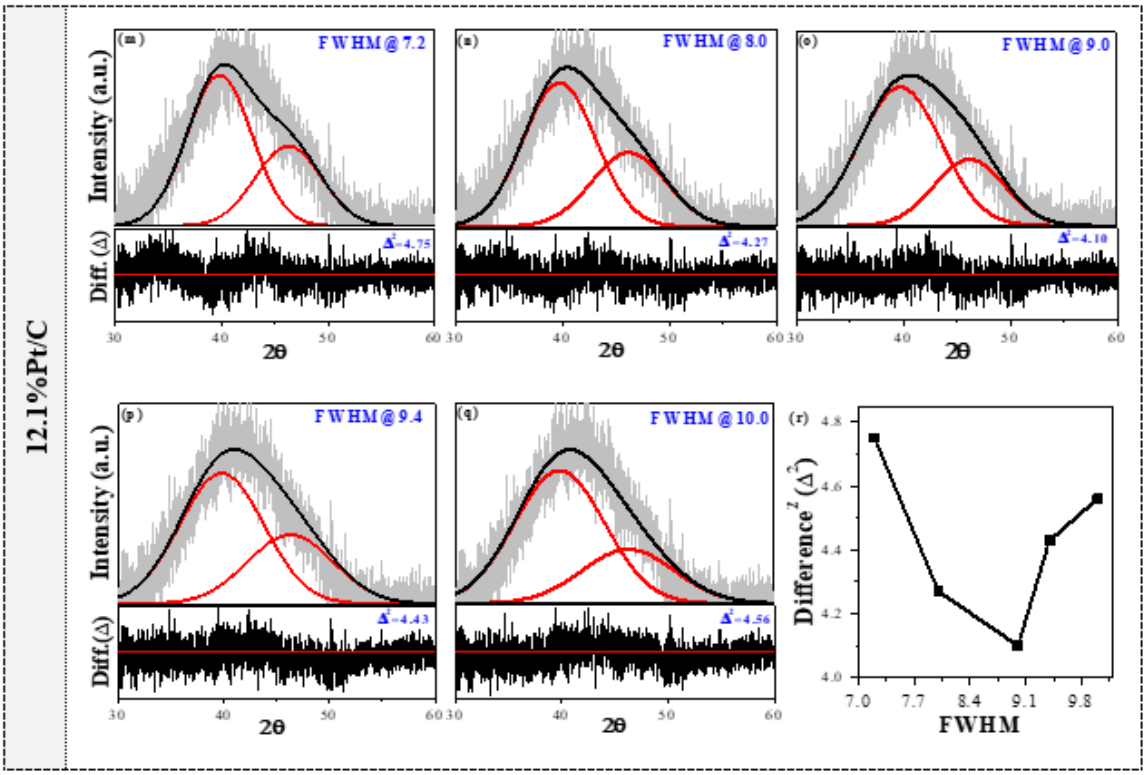

Figure B.1 Determination of appropriate HWHM to estimate particle size of reduced samples for (a-f) 12.5%Pt/NC, (g-l) 6.5%Pt/C, and (m-r) 12.1%Pt/C.

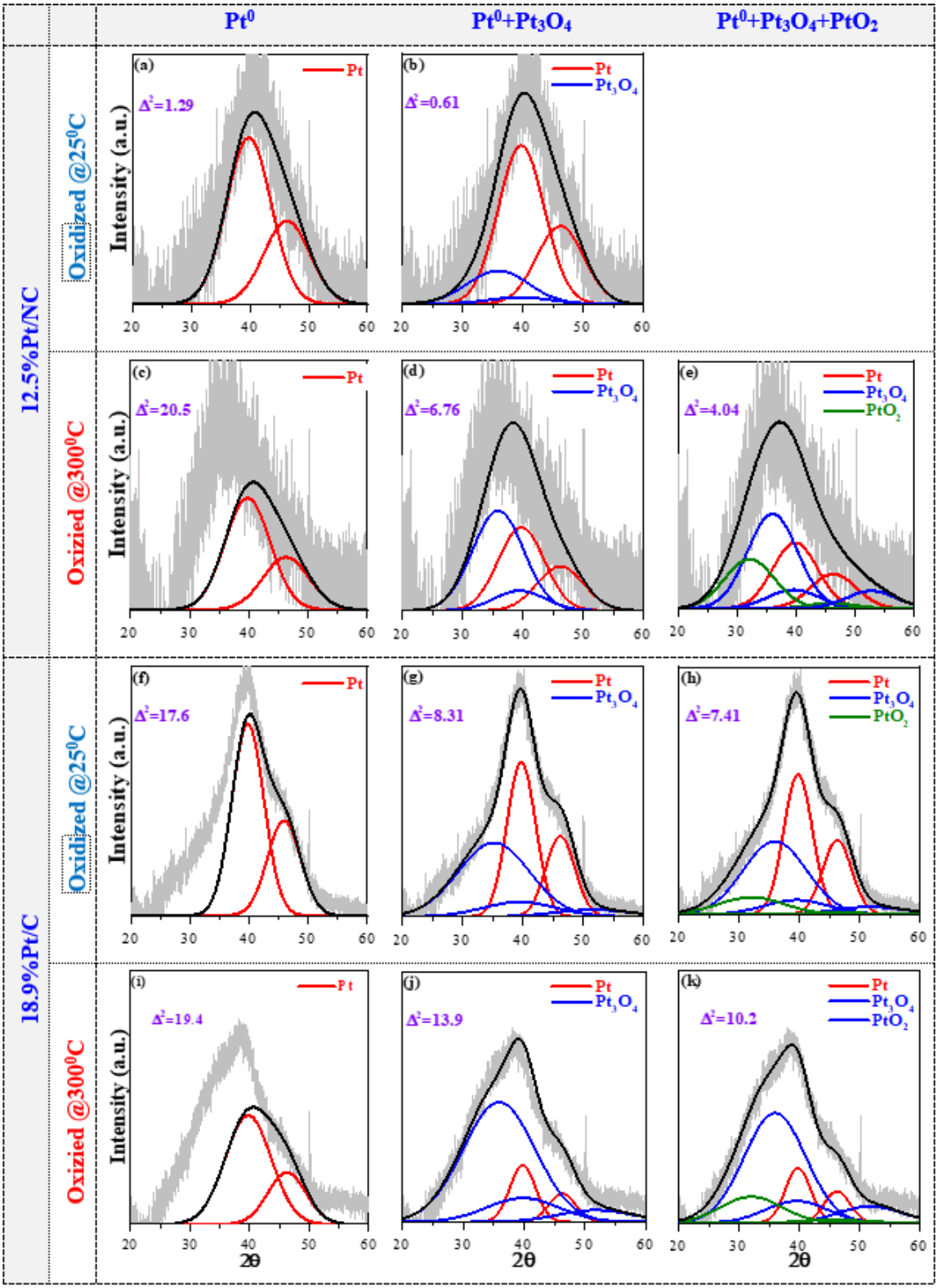
Pt⁰
Pt⁰+Pt₃O₄
Pt⁰+Pt₃O₄+PtO₂
12.5%Pt/NC
18.9%Pt/C
Oxidized @25⁰C
Oxizied @300⁰C
Intensity (a.u.)
2θ
(a) Pt Δ²=1.29
(b) Pt Pt₃O₄ Δ²=0.61
(c) Pt Δ²=20.5
(d) Pt Pt₃O₄ Δ²=6.76
(e) Pt Pt₃O₄ PtO₂ Δ²=4.04
(f) Pt Δ²=17.6
(g) Pt Pt₃O₄ Δ²=8.31
(h) Pt Pt₃O₄ PtO₂ Δ²=7.41
(i) Pt Δ²=19.4
(j) Pt Pt₃O₄ Δ²=13.9
(k) Pt Pt₃O₄ PtO₂ Δ²=10.2

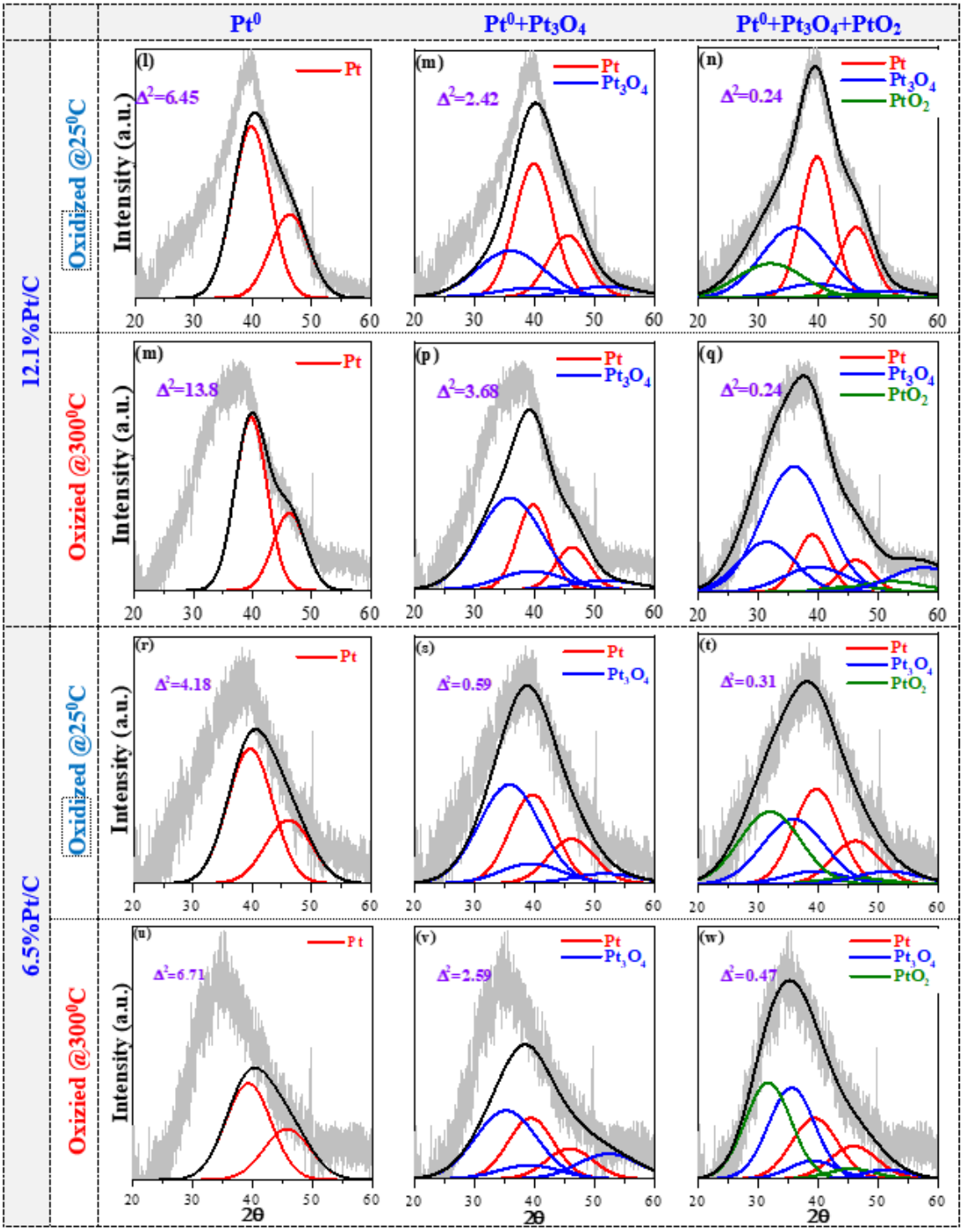

Figure B.2 Confirmation of different Pt phases formed due to oxidation treatment at 25 °C and 300 °C for (a-e) 12.5%Pt/NC, (f-k) 18.9%Pt/C, (l-q) 12.1%Pt/C, and (r-w) 6.5%Pt/C.

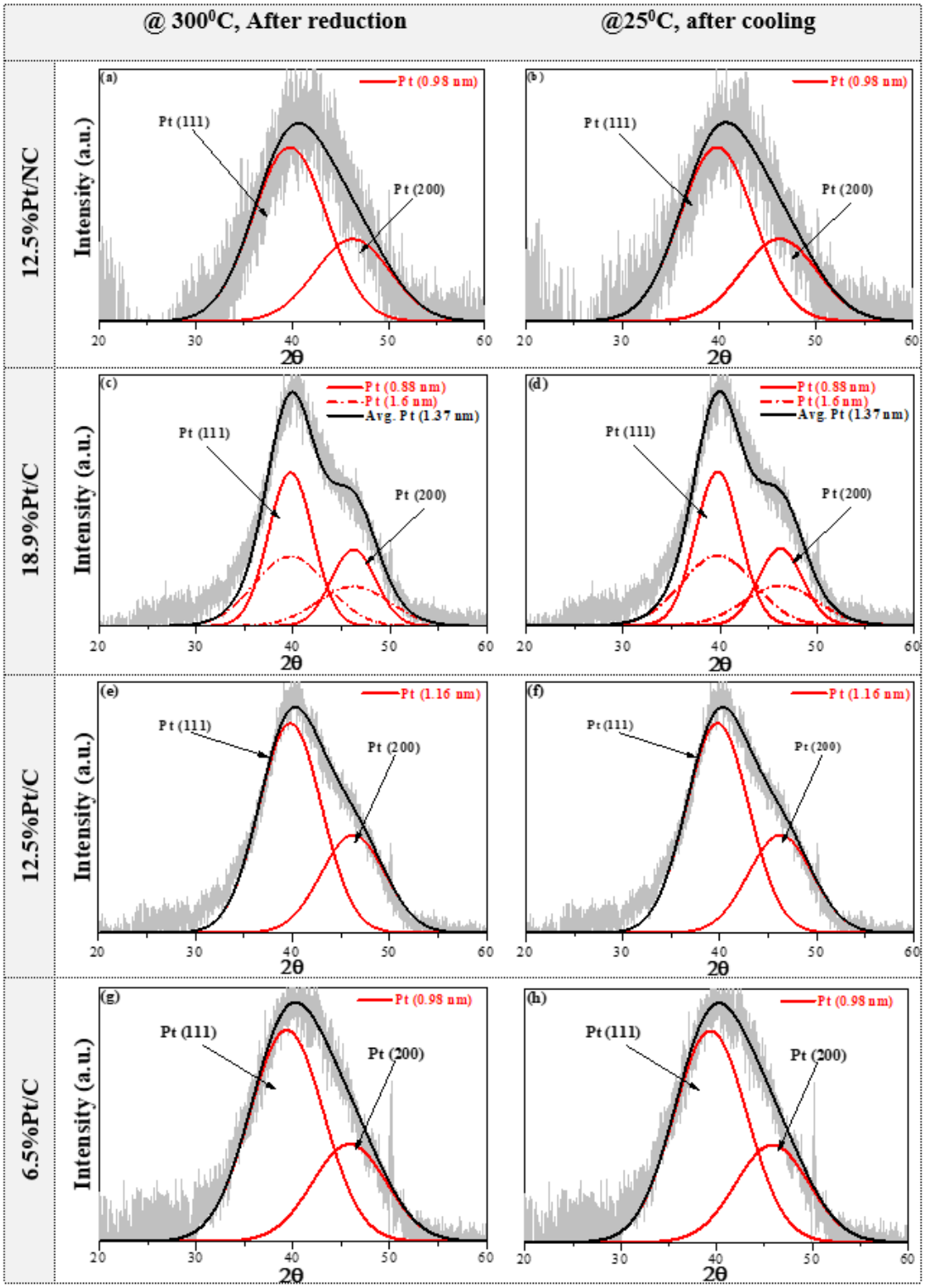

Figure B.3 Deconvoluted patterns for reduced samples: (a-b) 12.5%Pt/NC, (c-d) 18.9%Pt/C, (e-f) 12.1%Pt/C, and (g-h) 6.5%Pt/C. The measurements were done just after reduction at 300 °C and after cooling at 25°C under flowing of 20%H_2 balance He with a flow rate of 100 sccm.

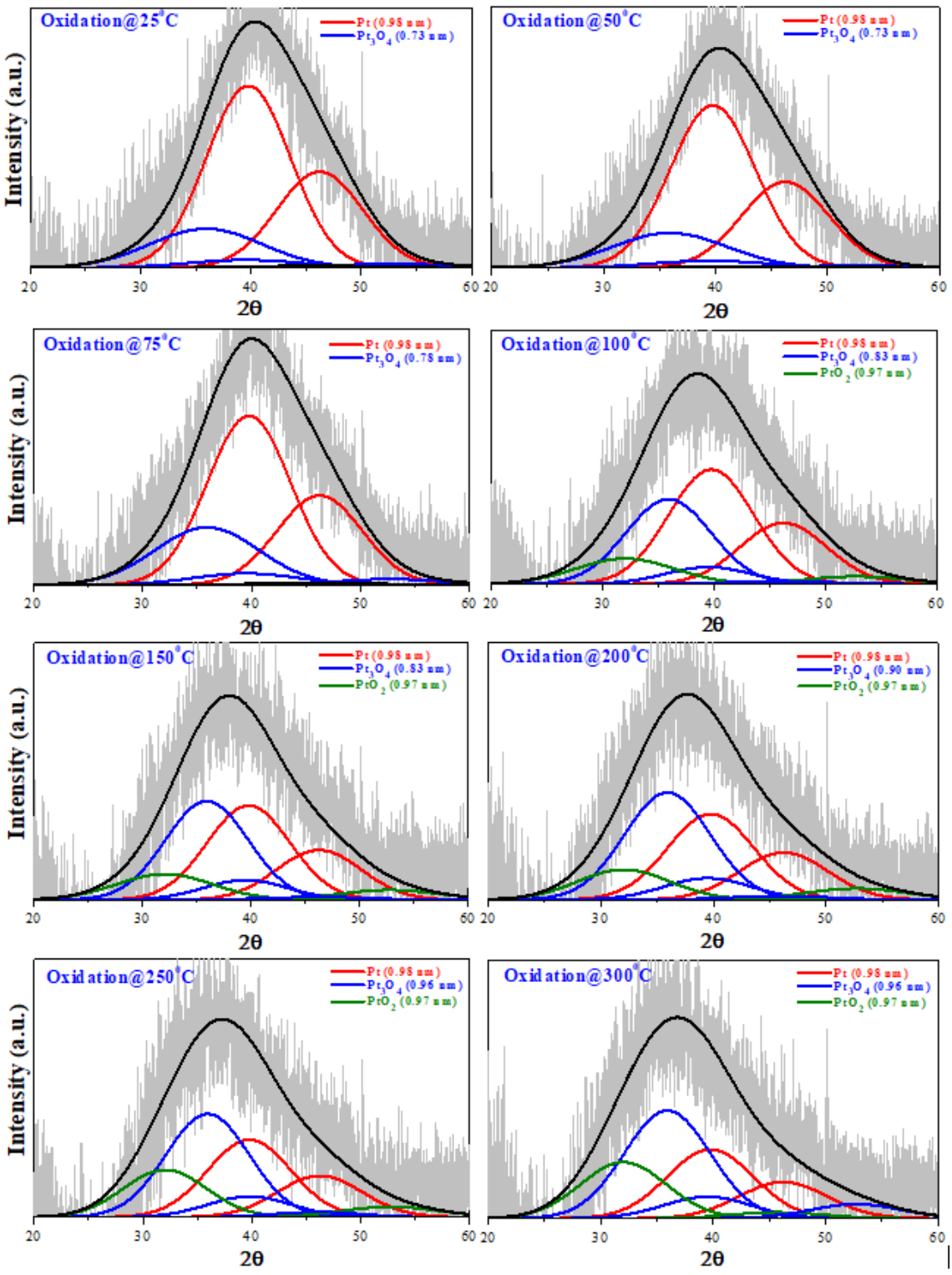

Figure B.4 Deconvoluted patterns of oxidized samples of 12.5%Pt/NC at different temperatures.

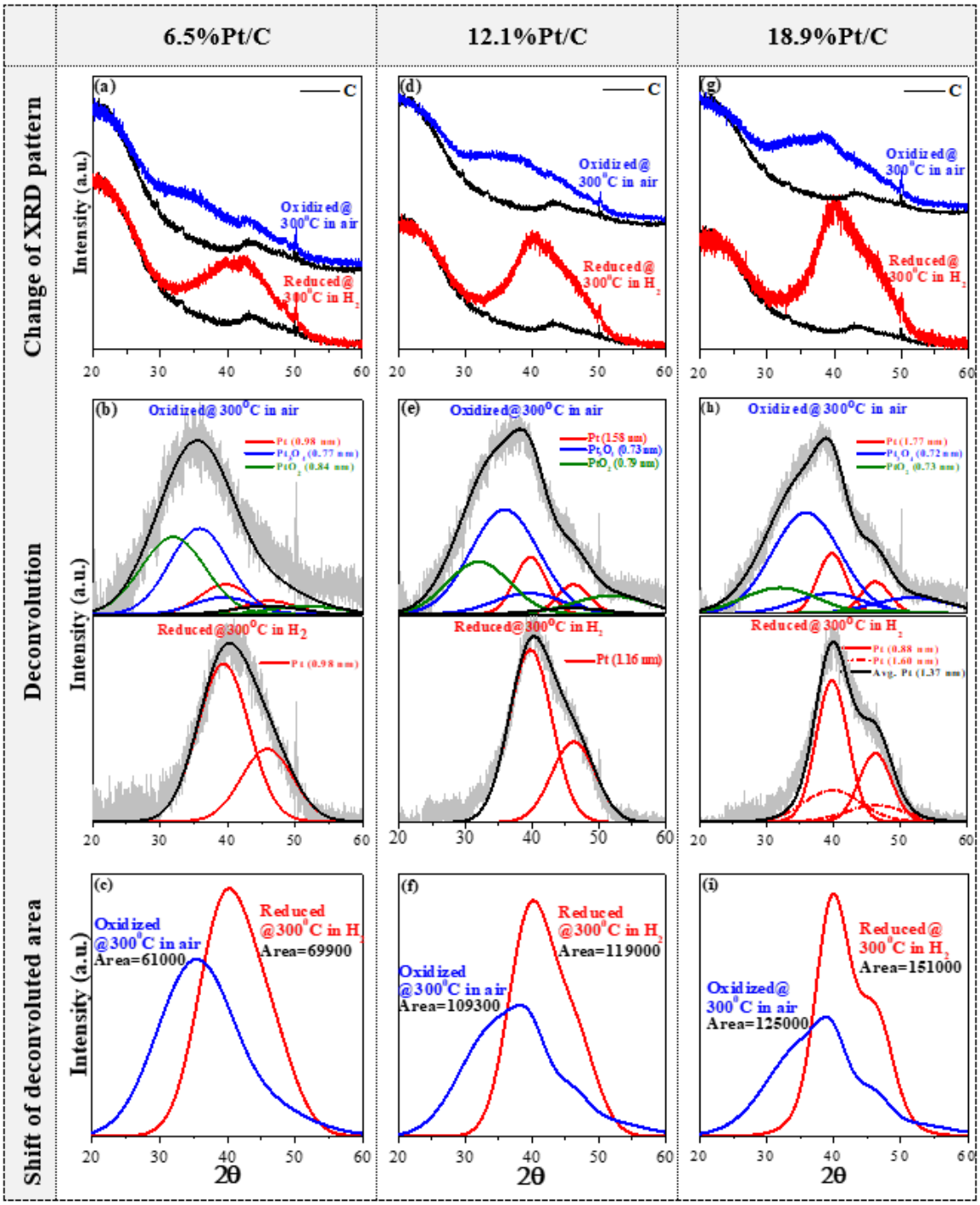

Figure B.5 Shifting of the deconvoluted area due to oxidation: (a-c) 6.5%Pt/C, (d-f) 12.1%Pt/C, and (g-i) 18.9%Pt/C.

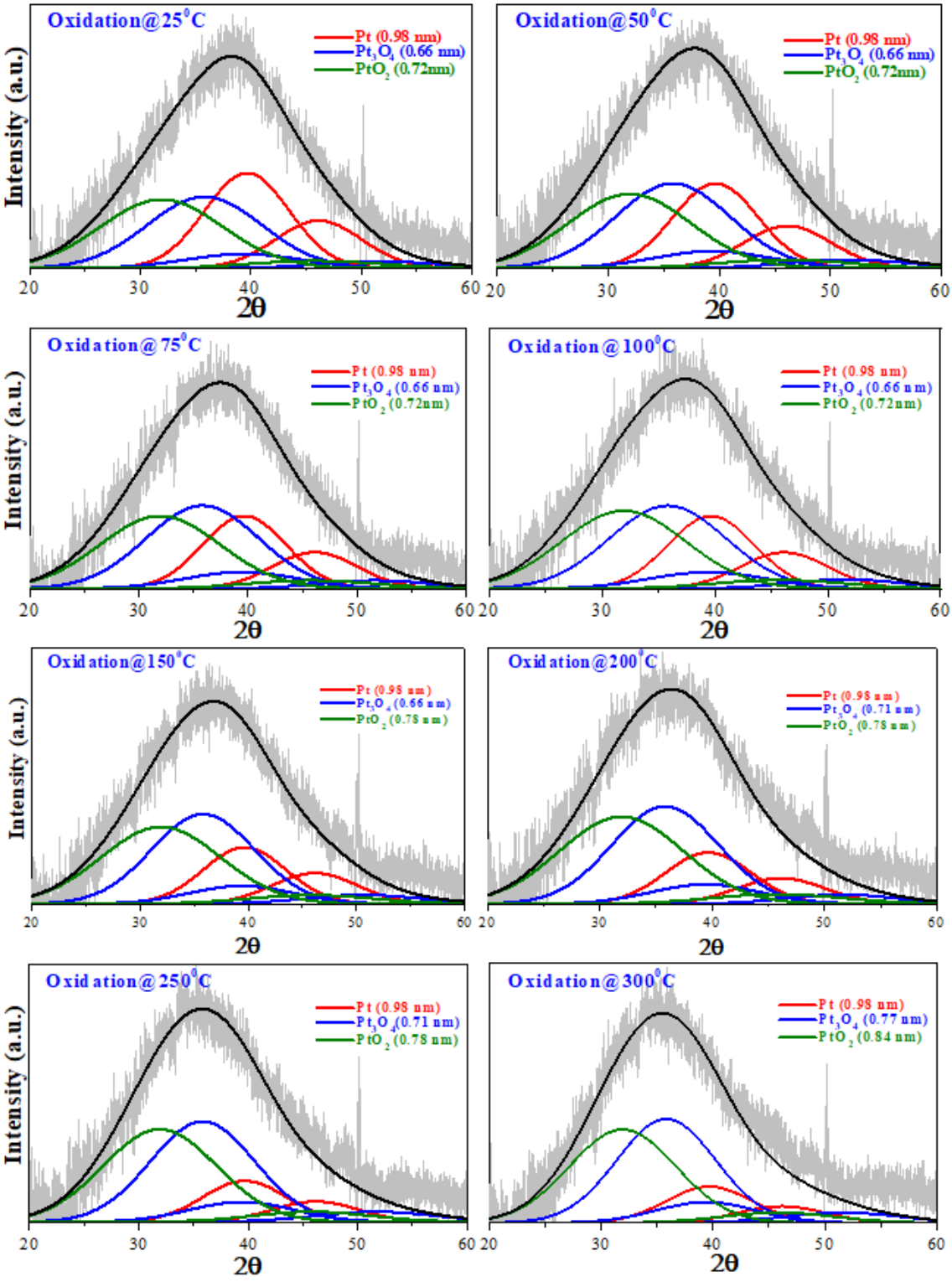

Figure B.6 Deconvoluted patterns of oxidized 6.5%Pt/C at different temperatures.

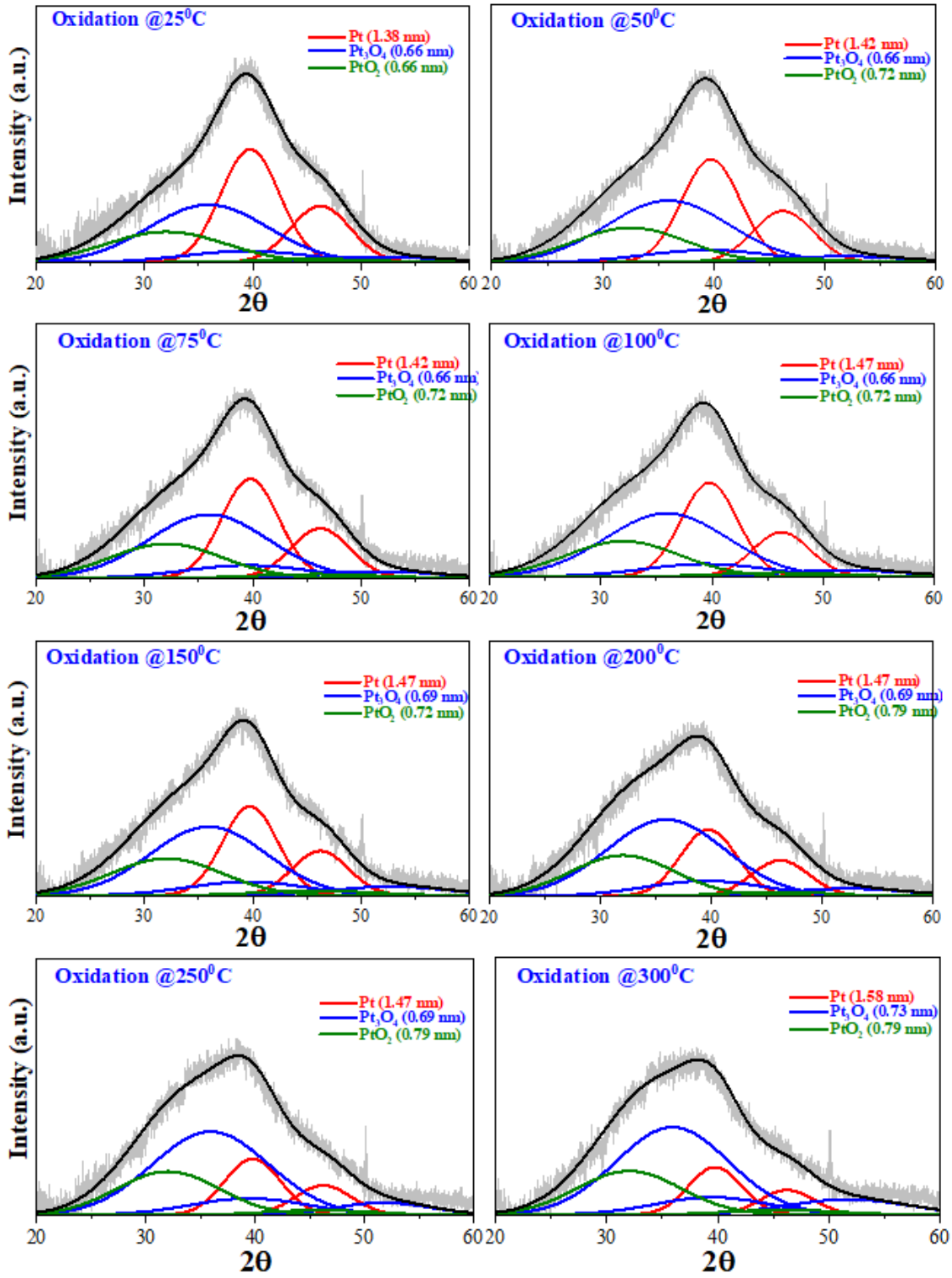

Figure B.7 Deconvoluted patterns of oxidized 12.1%Pt/C at different temperatures.

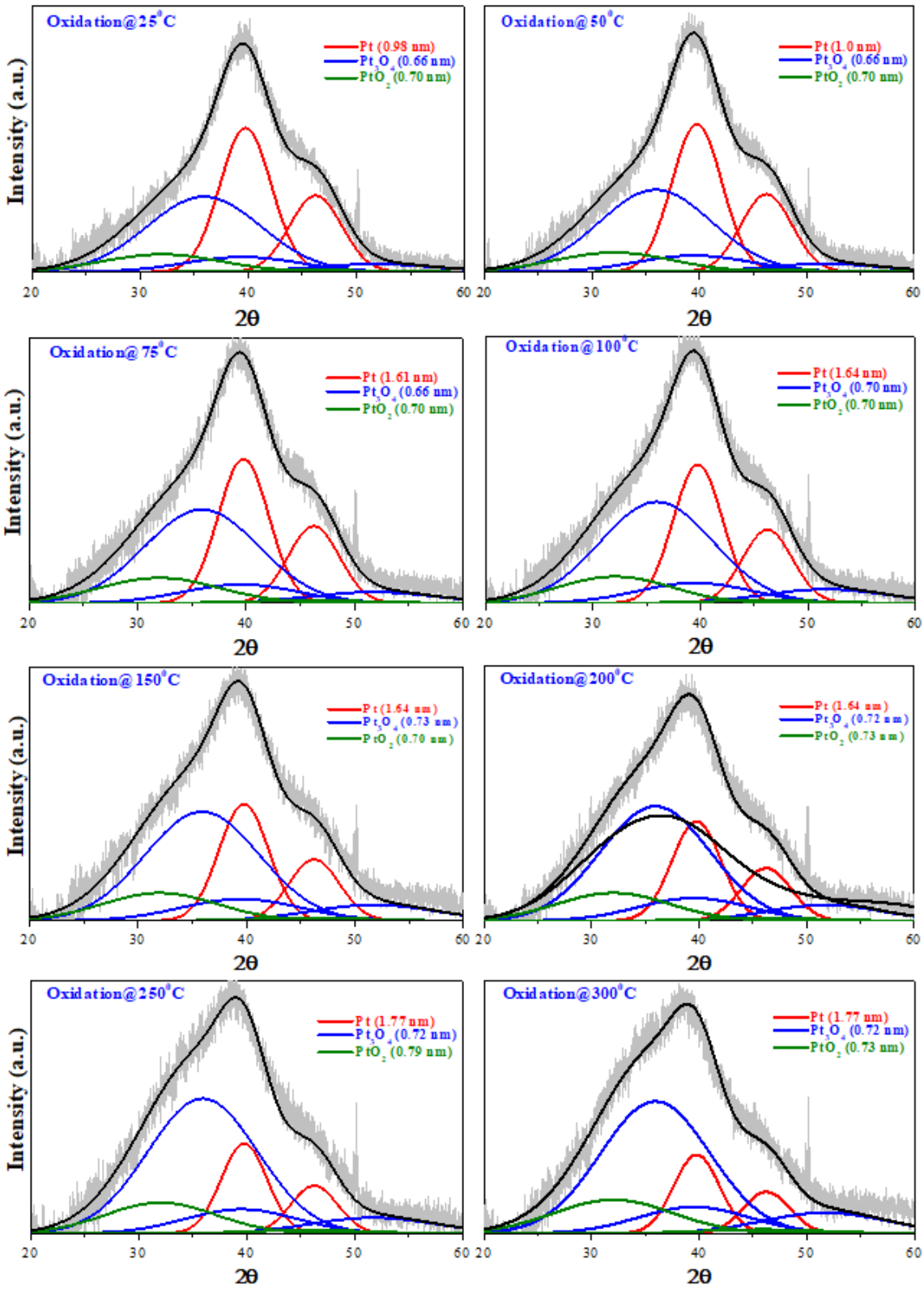

Figure B.8 Deconvoluted patterns of oxidized 18.9%Pt/C at different temperatures.

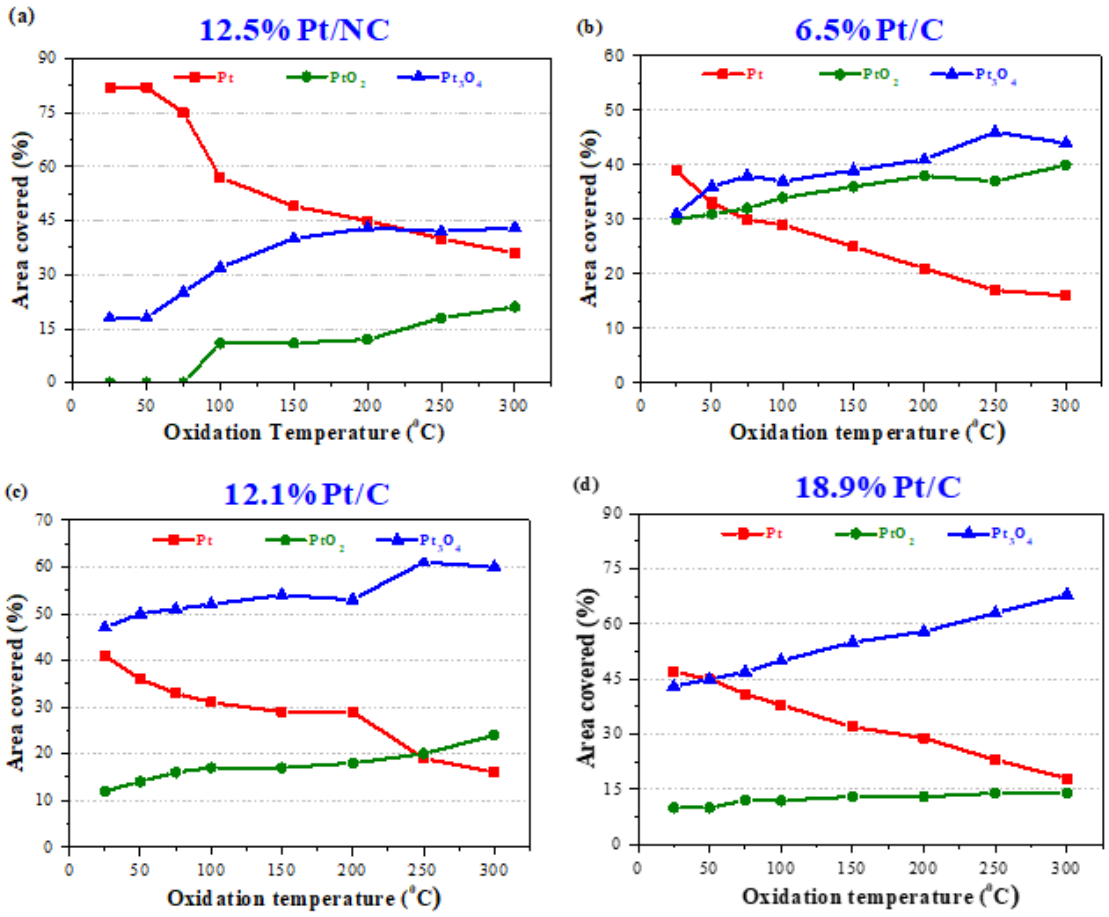

Figure B.9 Deconvoluted patterns of oxidized 18.9%Pt/C at different temperatures.

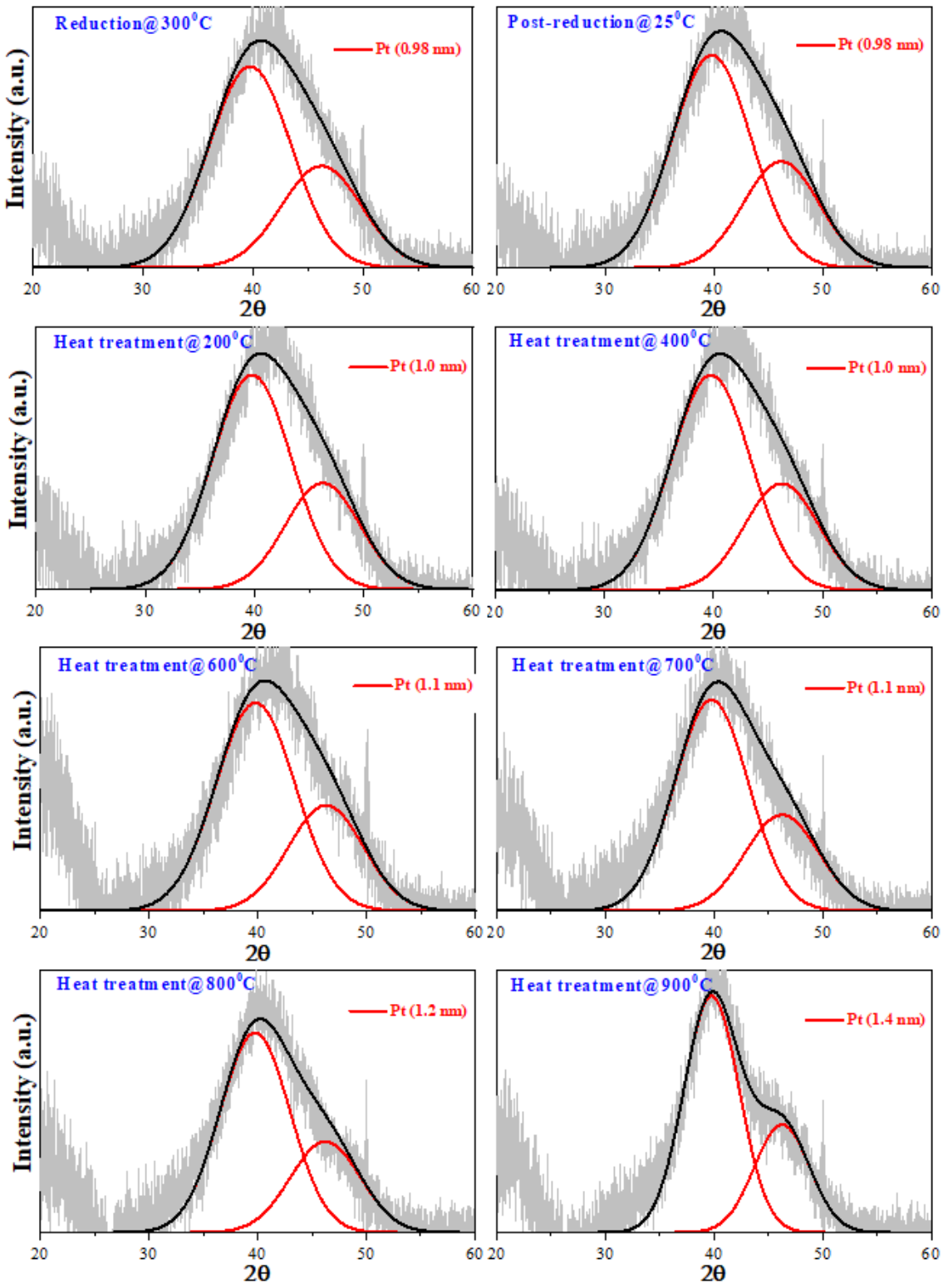

Figure B.10 Deconvoluted patterns of SEA prepared 12.5%Pt/NC catalyst after in-situ heat-treatment study.

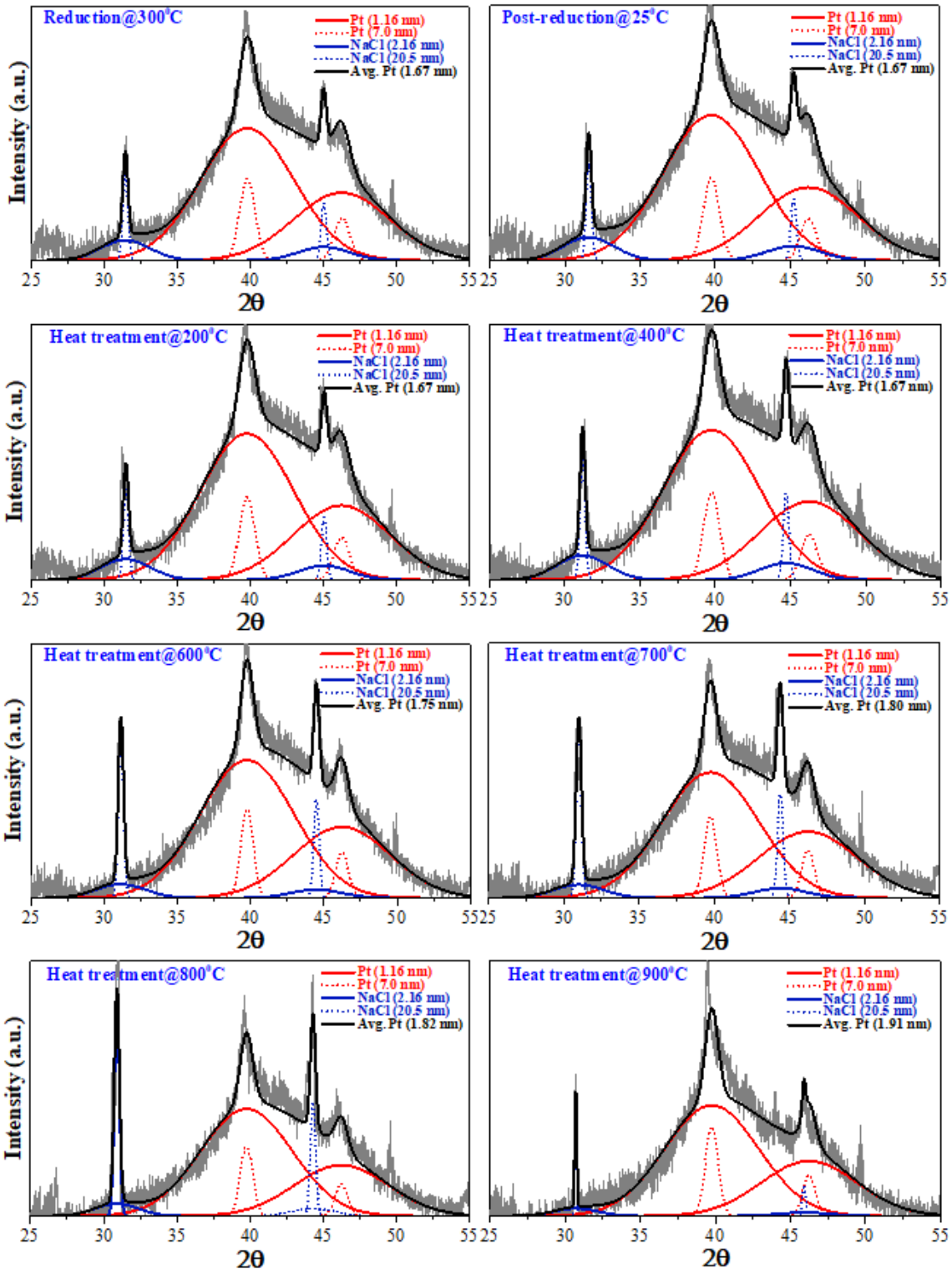

Figure B.11 Deconvoluted patterns of DI prepared 12.5%Pt/NC catalyst after in-situ heat-treatment study.

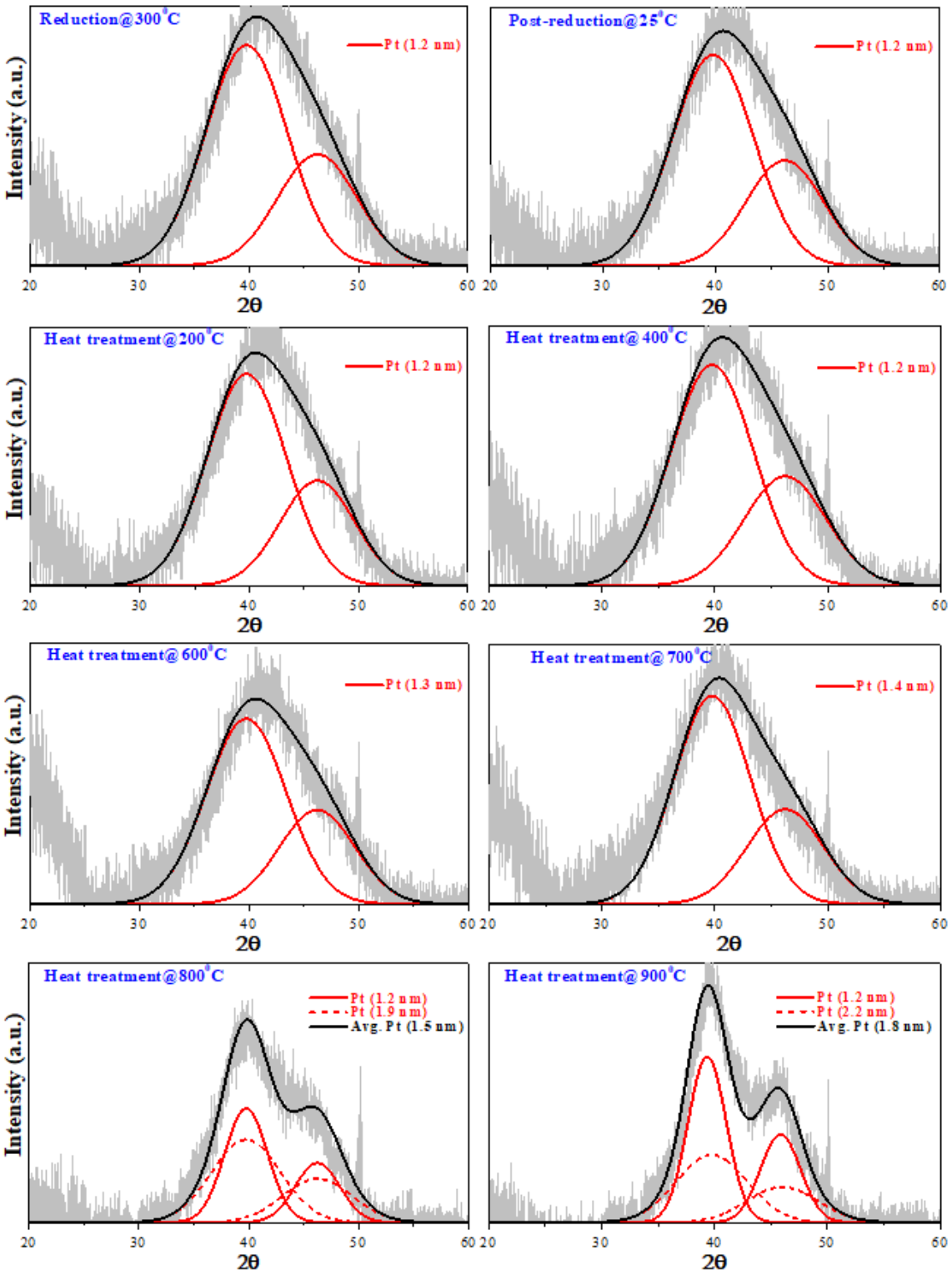

Figure B.12 Deconvoluted patterns of SEA prepared 12.1%Pt/C catalyst after in-situ heat-treatment study.

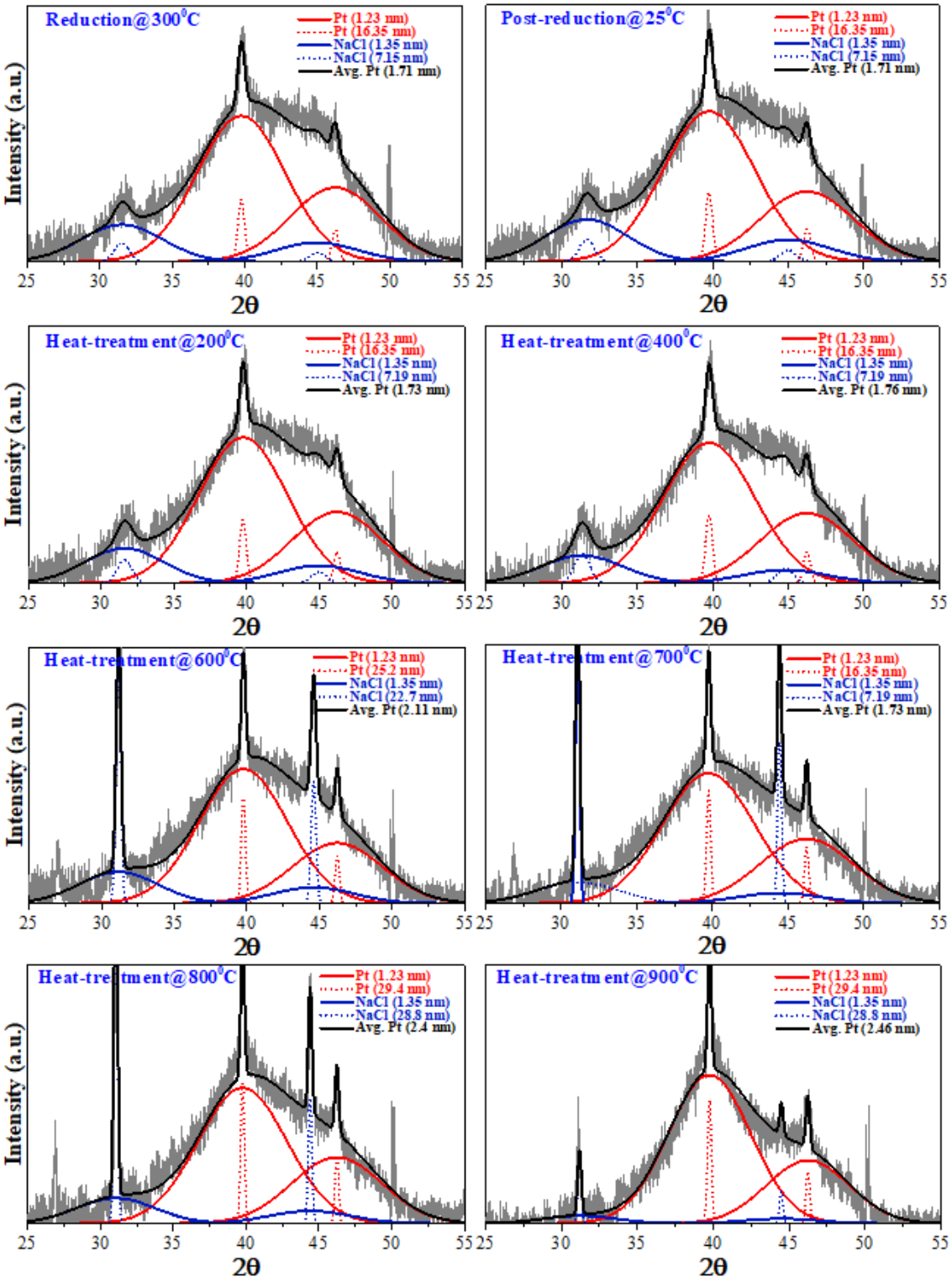

Figure B.13 Deconvoluted patterns of DI prepared 12.1%Pt/C catalyst after in-situ heat-treatment study.

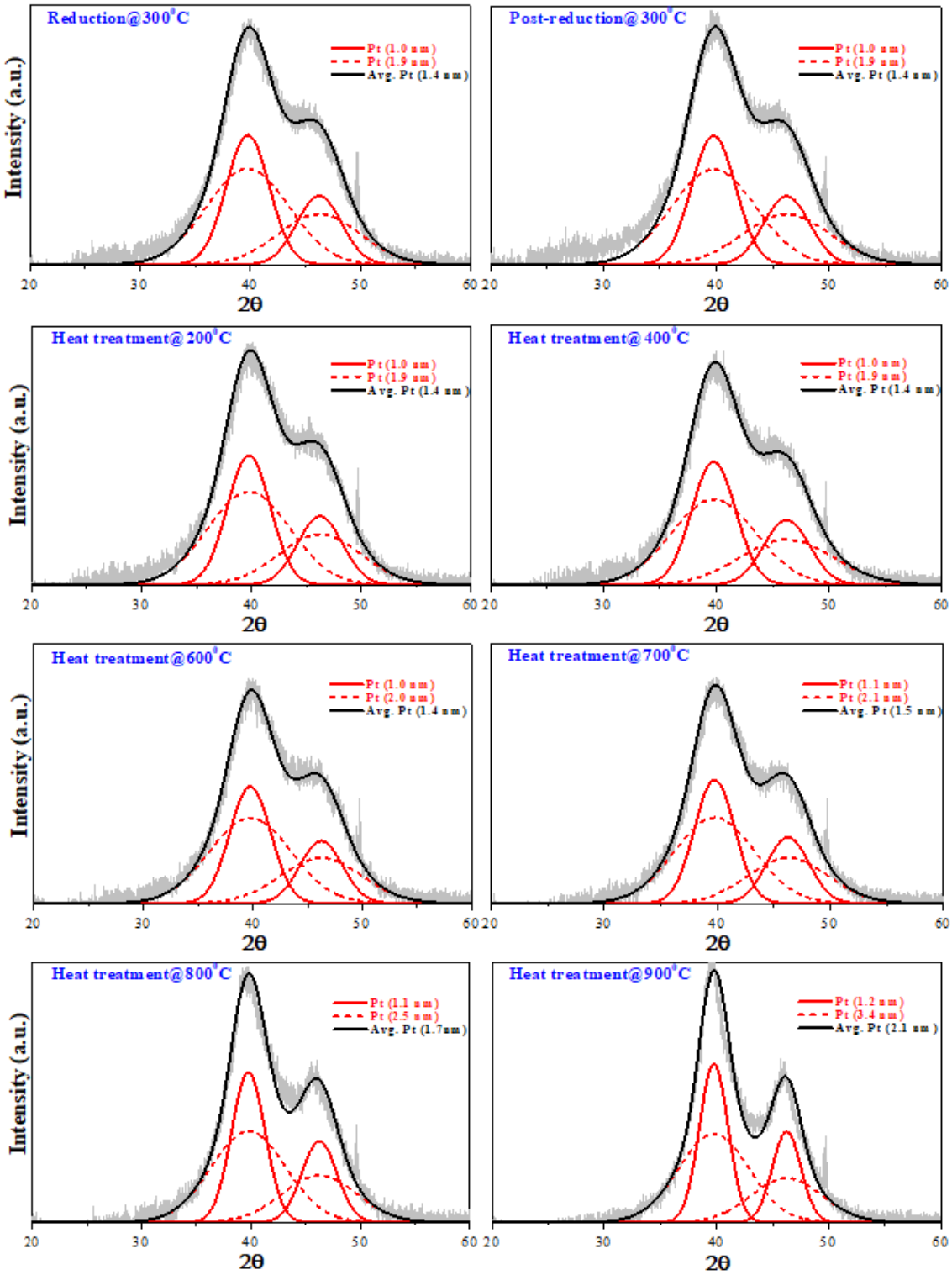

Figure B.14 Deconvoluted patterns of SEA prepared 18.9%Pt/C catalyst after in-situ heat-treatment study.

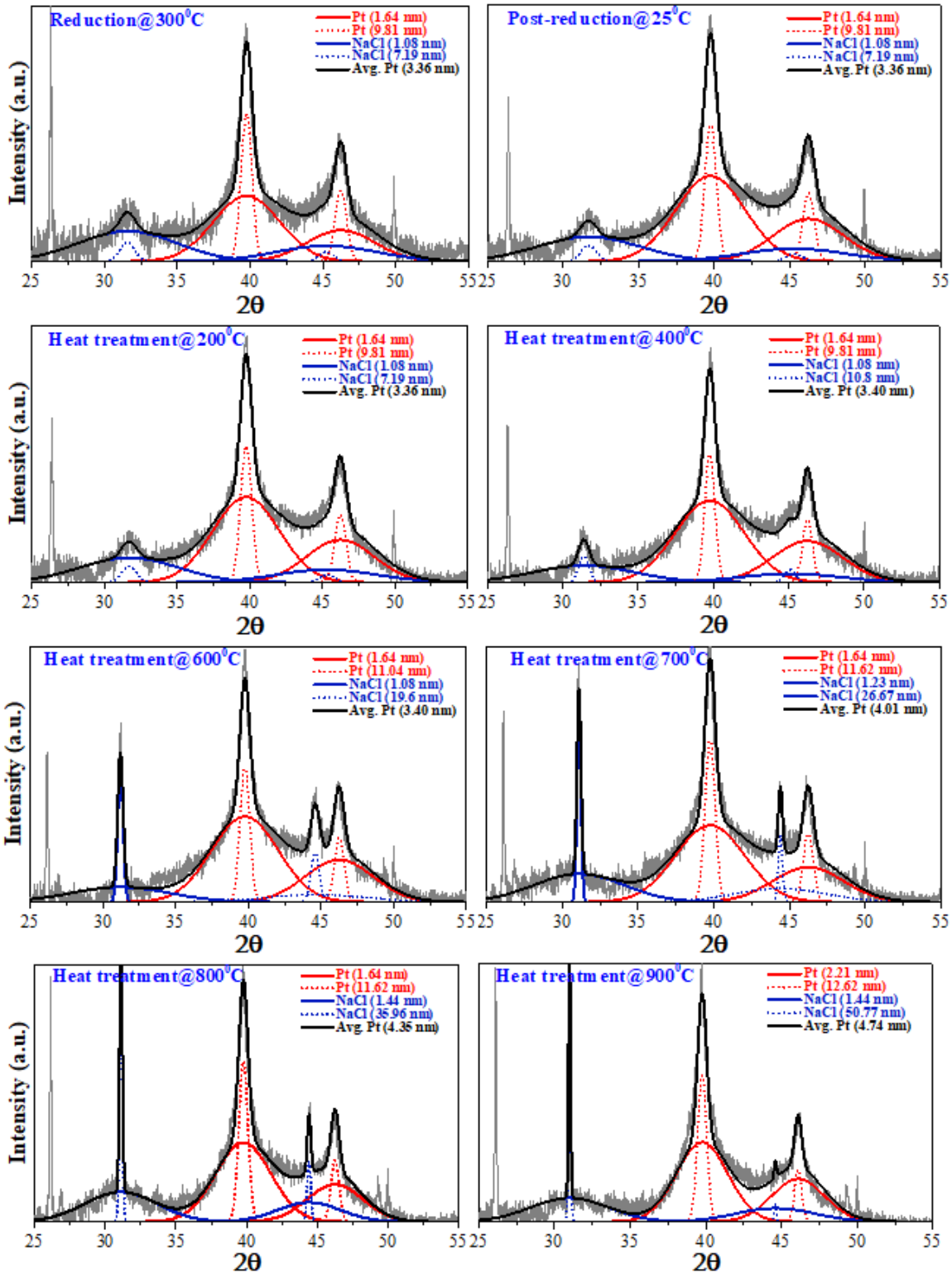

Figure B.15 Deconvoluted patterns of DI prepared 18.9%Pt/C catalyst after in-situ heat-treatment study.

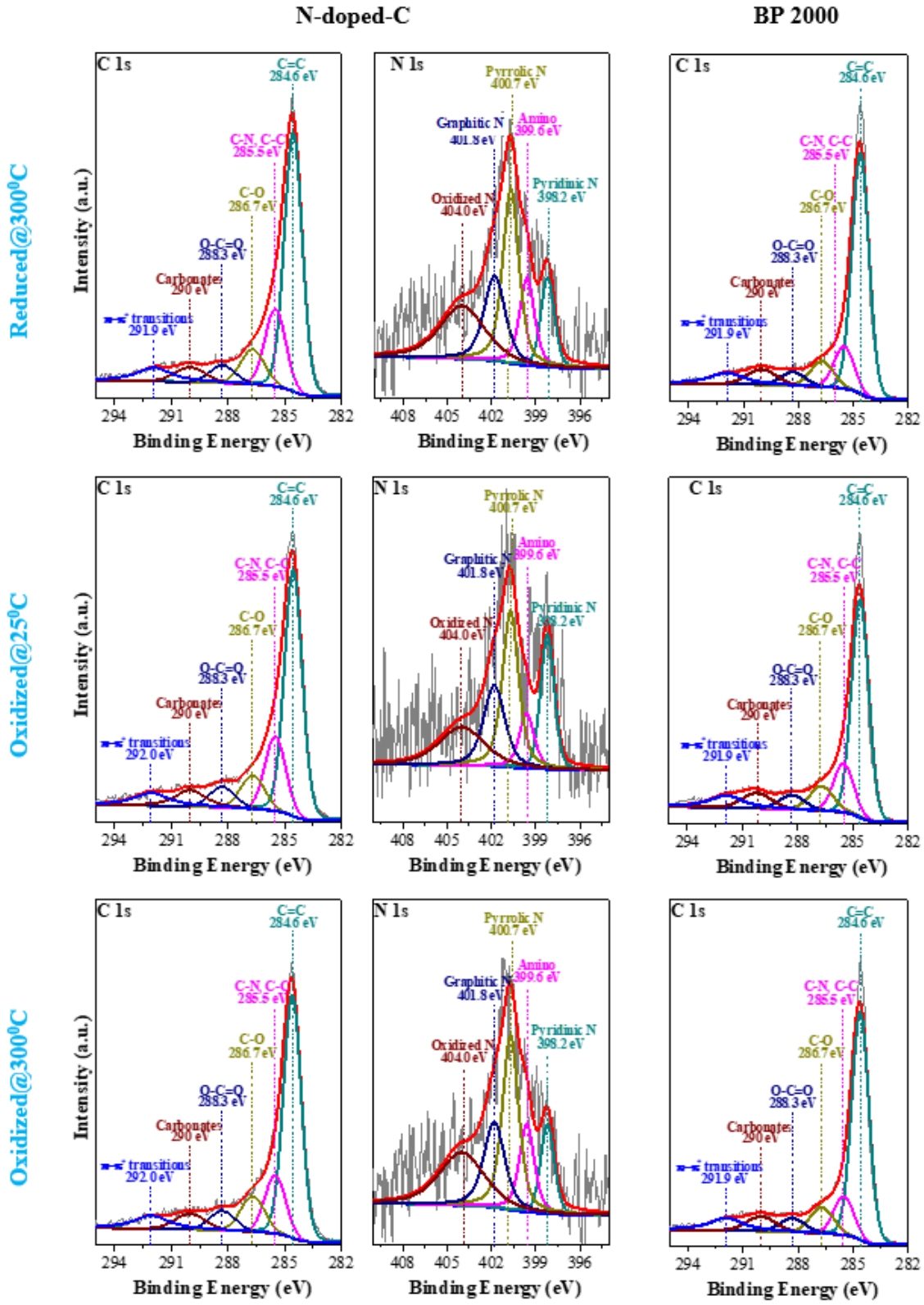

Figure B.16 C 1s and N 1s XPS spectra for N-doped-C and BP 2000

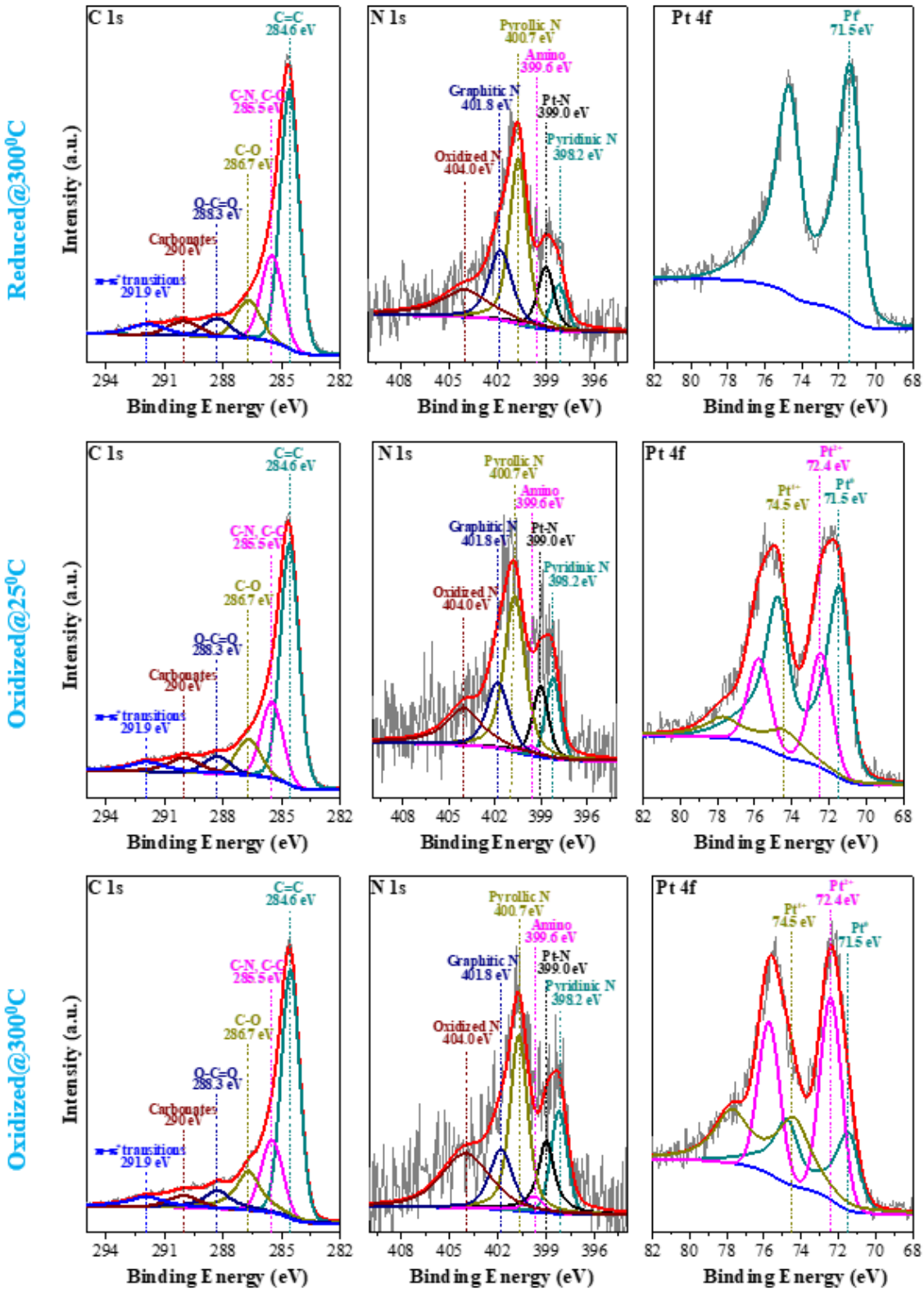

Figure B.17 C 1s, N 1s, and Pt 4f XPS spectra for the reduced and oxidized 12.5%Pt/NC.

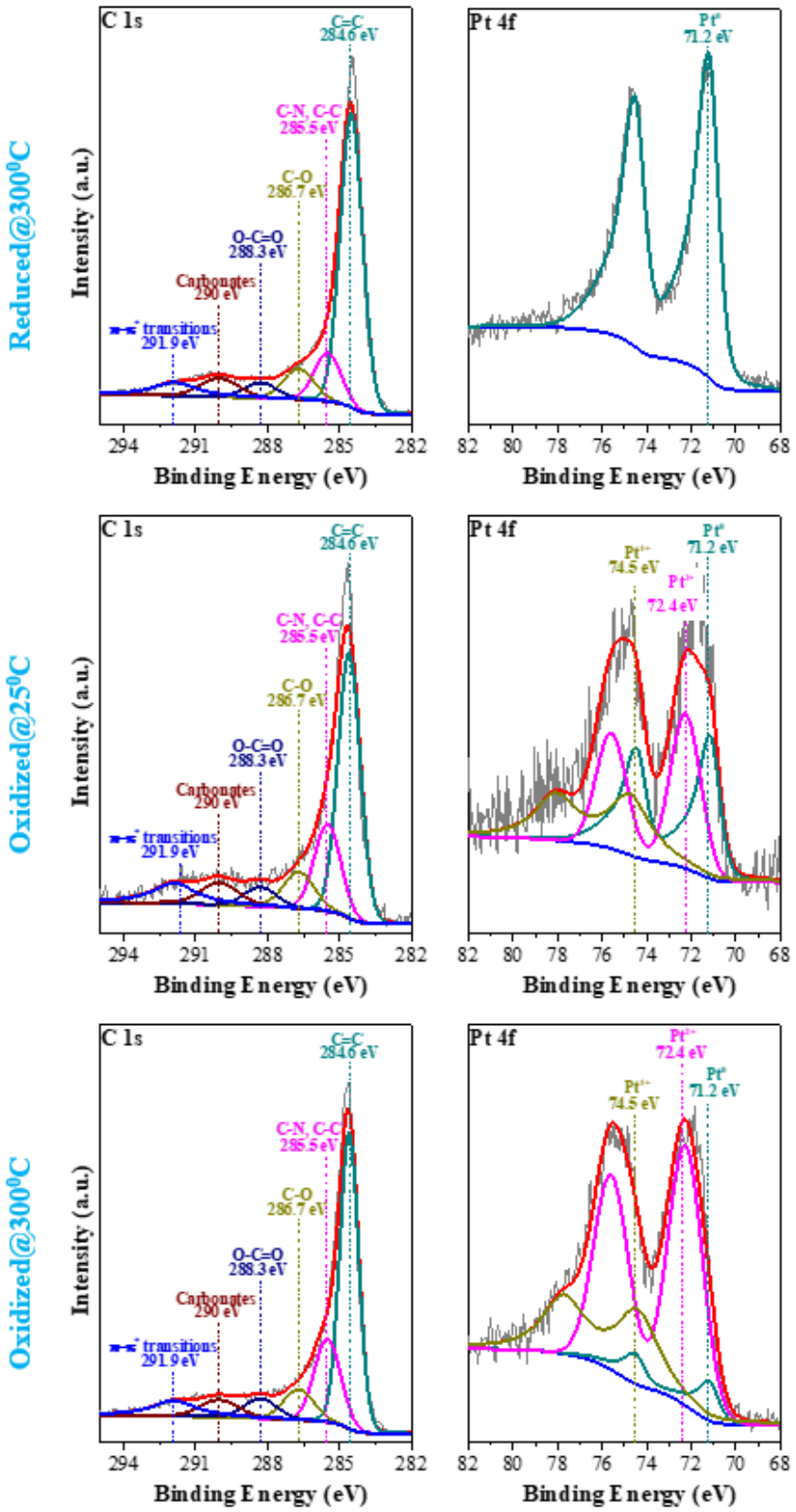

Figure B.18 C 1s and Pt 4f XPS spectra for the reduced and oxidized 18.9%Pt/C

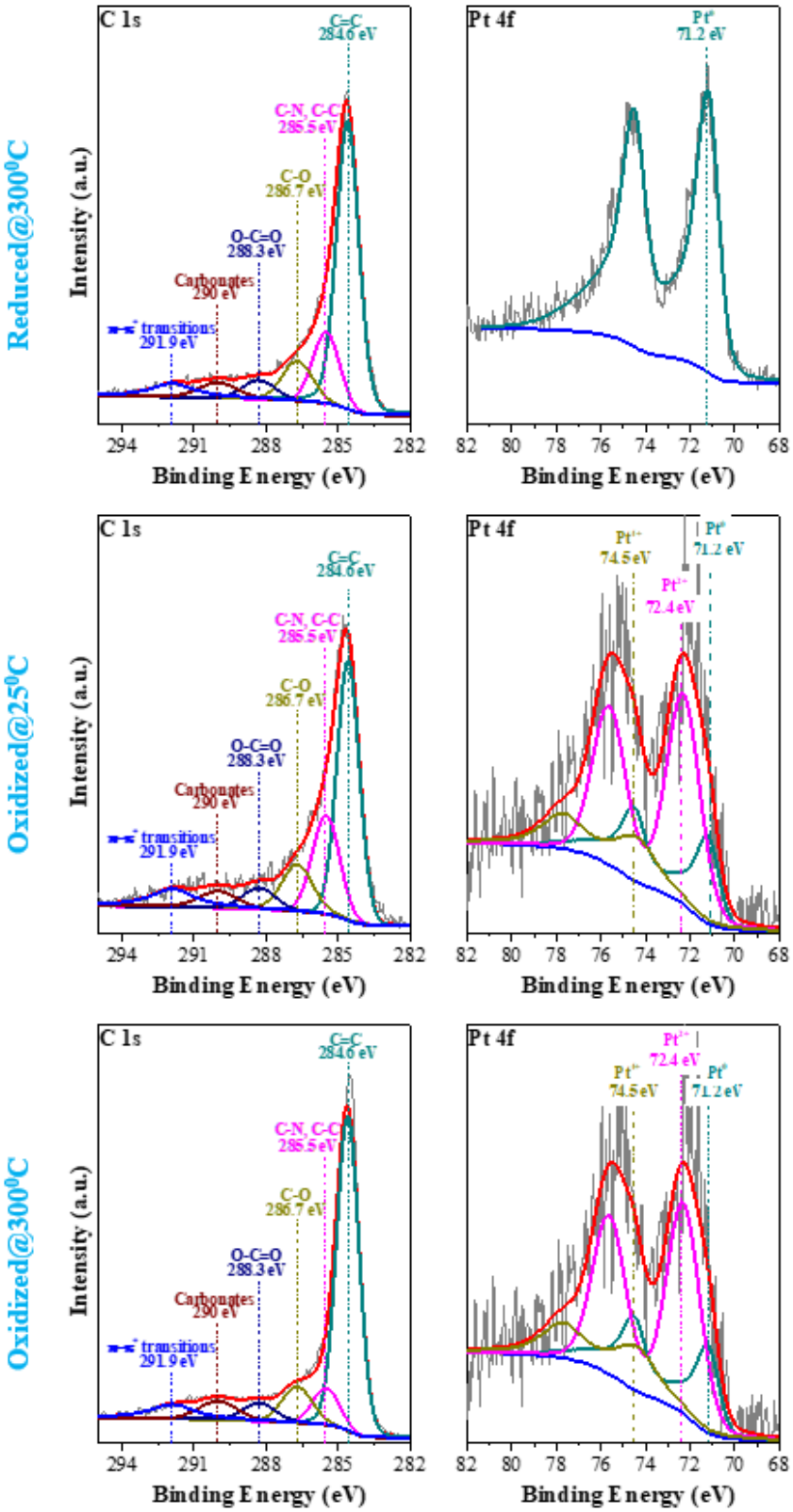

Figure B.19 C 1s and Pt 4f XPS spectra for the reduced and oxidized 6.5%Pt/C

Appendix C

Supplementary information for Chapter 4

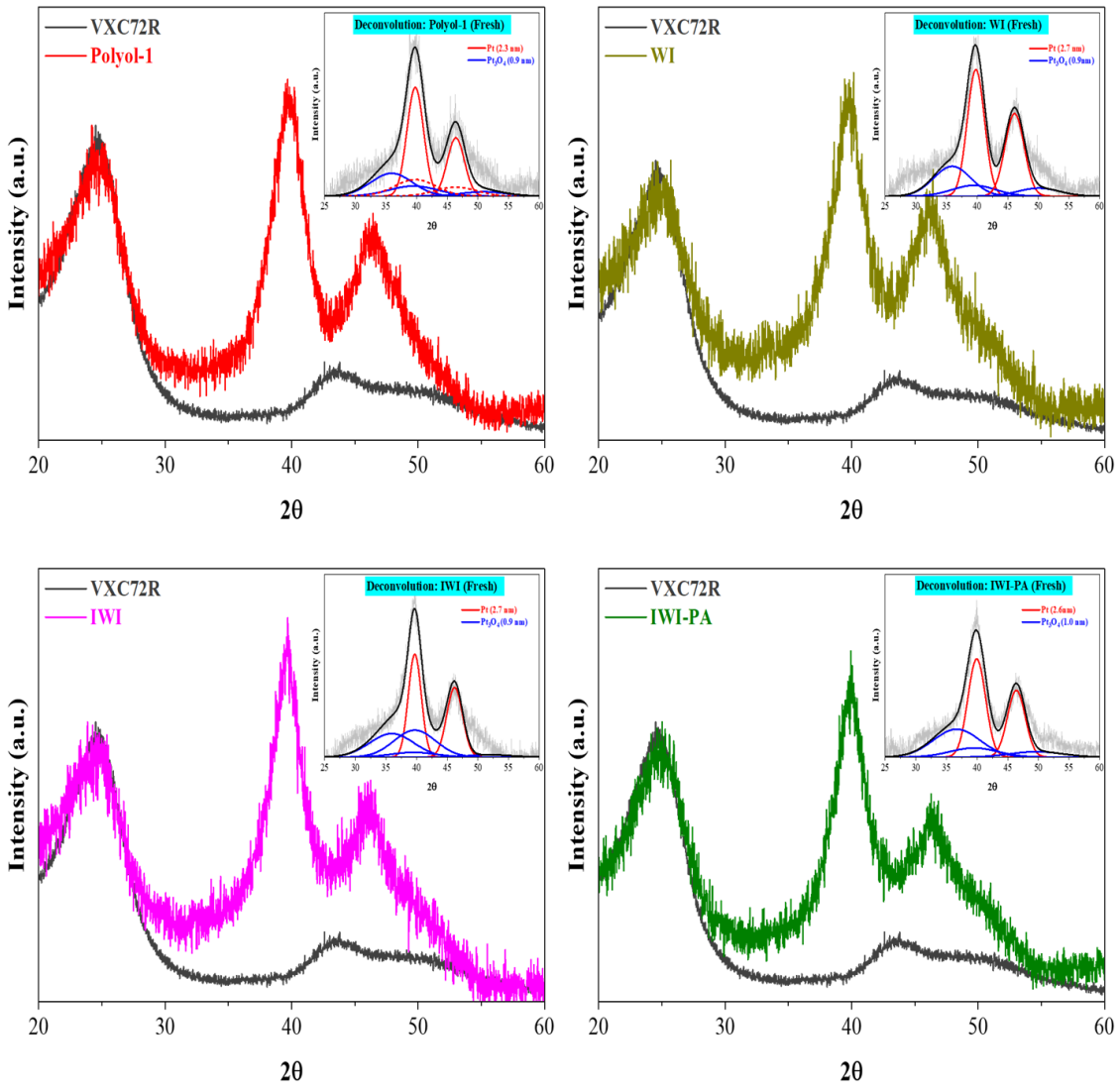

Figure C.1 XRD patterns of fresh Pt/C catalysts with respect to XC72R pattern with corresponds deconvoluted. Deconvolution was performed after support substraction and fitting Pt and Pt3O4 peaks.

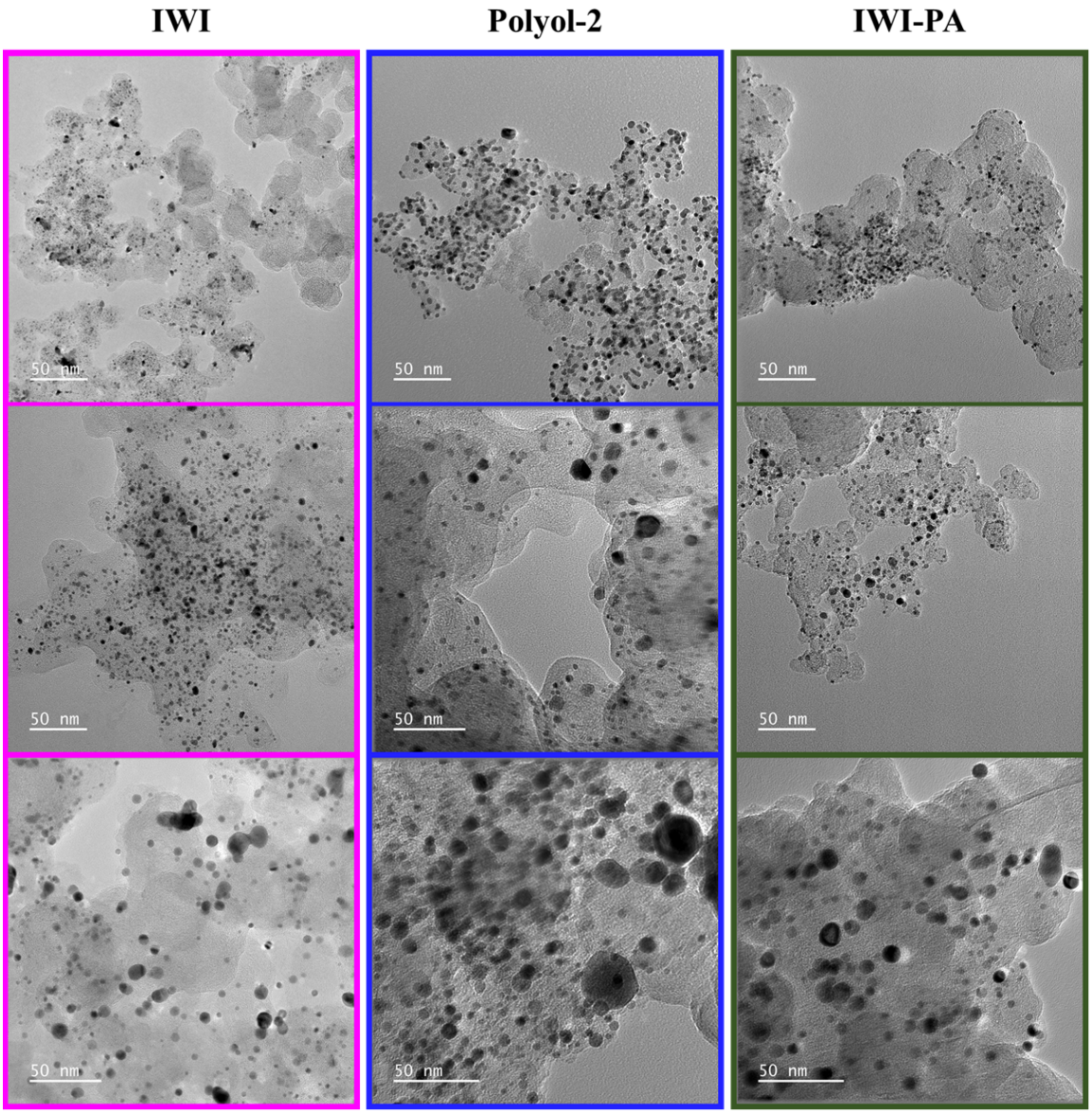

Figure C.2 (a) TEM images of fresh (as-prepared), annealed, and post-MEA catalysts and (b) particle size distribution of fresh catalysts prepared by SEA, WI and Polyol-1; (c) the growth of Pt particles due to high temperature annealing and 30K AST. Annealing was performend under 6%H_2/Ar at 750 °C for 12 h and AST was performed at potential between 0.6 and 0.95 V under H_2/N_2 (150 kPa_{abs}, 80 °C, 100%RH, 200/200 SCCM) for 30,000 cycles.

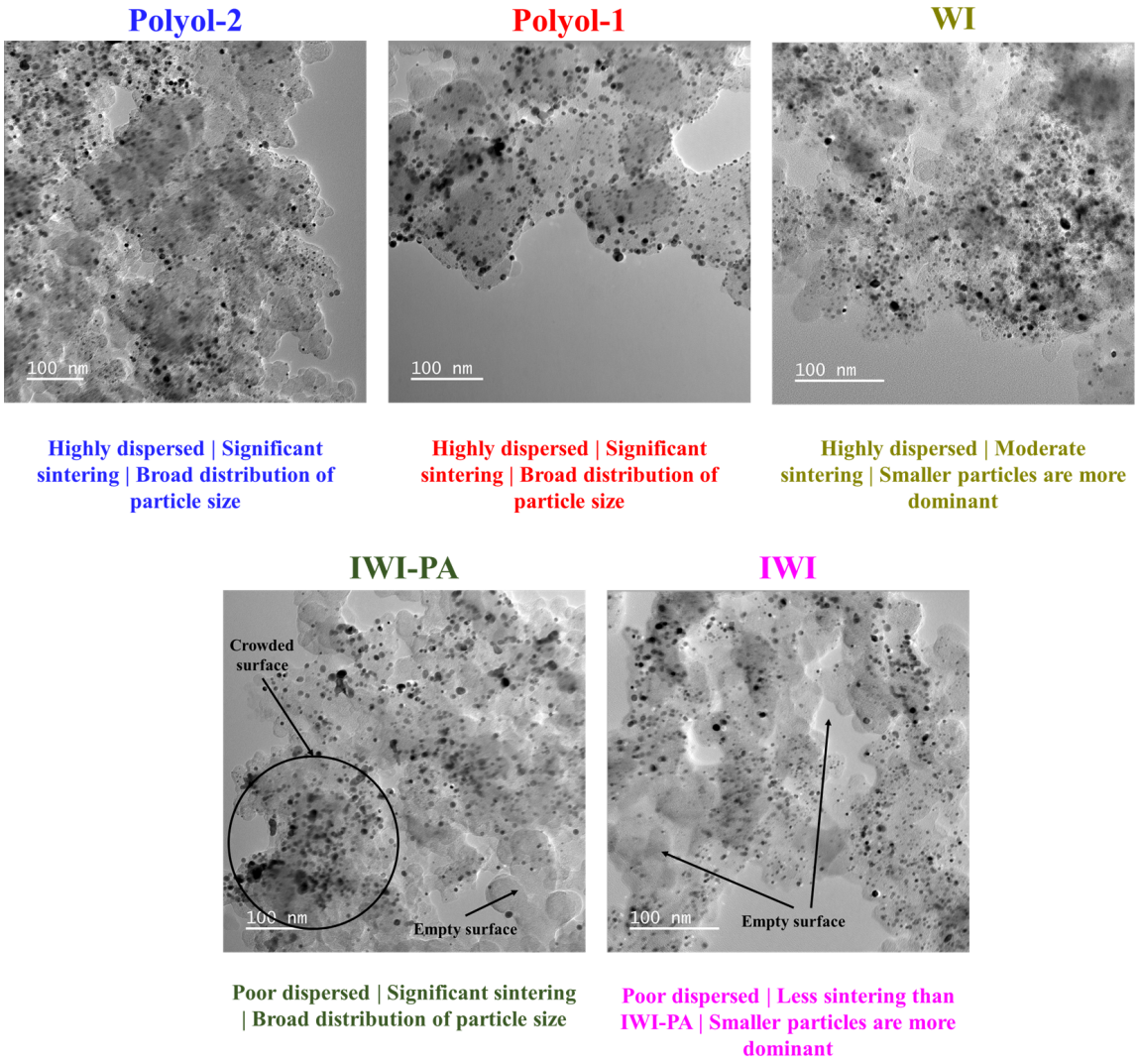

Figure C.3 Low-resolution TEM images of post-MEA catalysts.

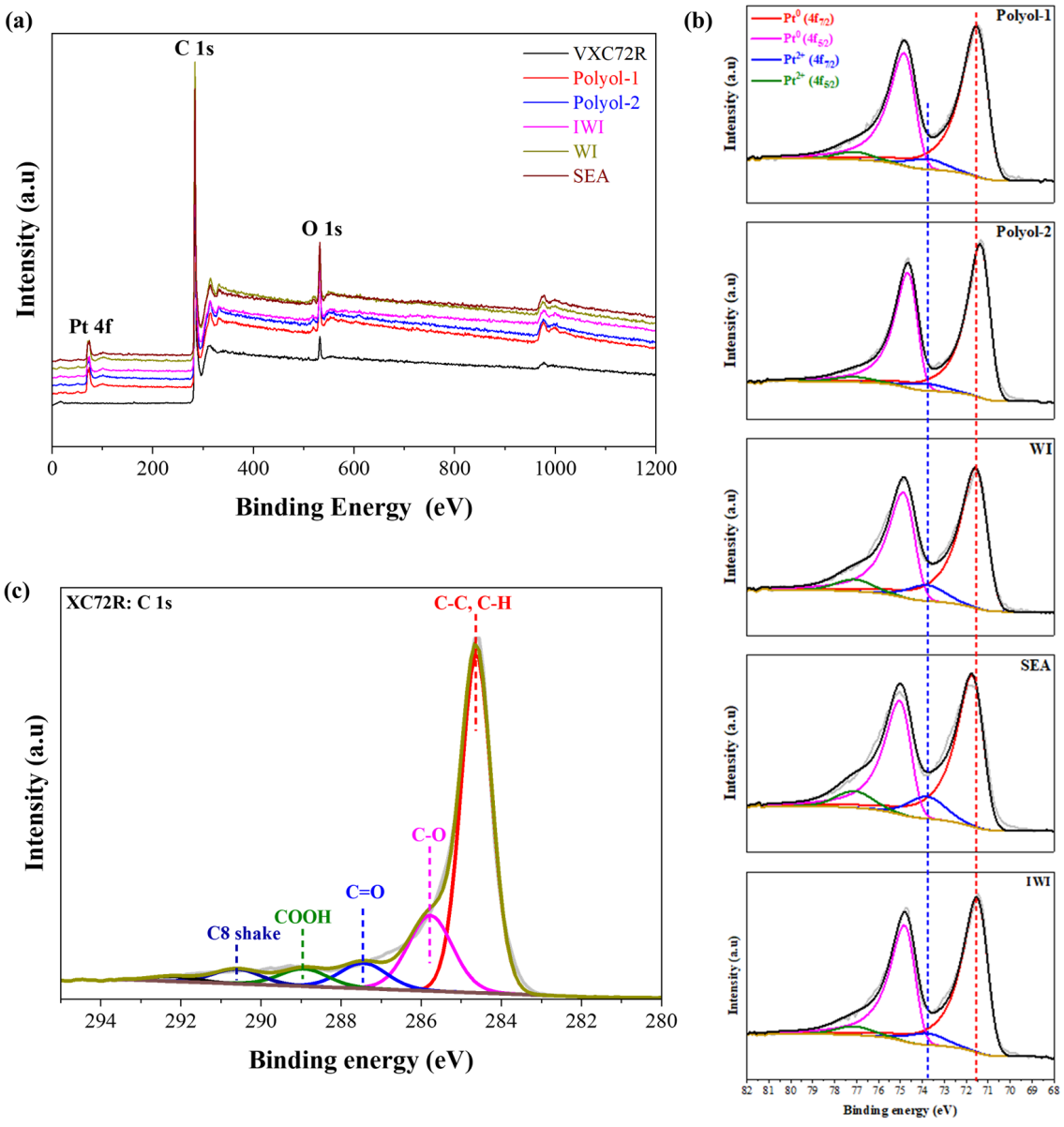

Figure C.4 (a) Full XPS spectrum of Pt/C catalysts and corrosponding XPS spectra of (b) Pt 4f; (c) XPS spectra of C 1s in XC72R.